Fiber-Optic Sensors for Fully-Distributed Physical, Chemical and Biological Measurement

Yunjing Wang

Dissertation submitted to the faculty of the Virginia Polytechnic Institute and State
University in partial fulfillment of the requirements for the degree of

Doctor of Philosophy
In
Electrical Engineering

Anbo Wang, Co-Chair
Gary R. Pickrell, Co-Chair
Ting-Chung Poon
James R. Heflin
Yong Xu

December 11, 2012
Blacksburg, Virginia

Keywords: Fiber Optics, Distributed Sensing, Long Period Grating, Acousto-Optics

Fiber-Optic Sensors for Fully-Distributed Physical, Chemical and Biological Measurement

Yunjing Wang

ABSTRACT

Distributed sensing is highly desirable in a wide range of civil, industrial and military applications. The current technologies for distributed sensing are mainly based on the detection of optical signals resulted from different elastic or non-elastic light-matter interactions including Rayleigh, Raman and Brillouin scattering. However, they can measure temperature or strain only to date. Therefore, there is a need for technologies that can further expand measurement parameters even to chemical and biological stimuli to fulfill different application needs.

This dissertation presents a fully-distributed fiber-optic sensing technique based on a traveling long-period grating (T-LPG) in a single-mode fiber. The T-LPG is generated by pulsed acoustic waves that propagate along the fiber. When there are changes in the fiber surrounding medium or in the fiber surface coating, induced by various physical, chemical or biological stimuli, the optical transmission spectrum of the T-LPG may shift. Therefore, by measuring the T-LPG resonance wavelength at different locations along the fiber, distributed measurement can be realized for a number of parameters beyond temperature and strain.

Based on this platform, fully-distributed temperature measurement in a 2.5m fiber was demonstrated. Then by coating the fiber with functional coatings, fully-distributed biological and chemical sensing was also demonstrated. In the biological sensing experiment, immunoglobulin G (IgG) was immobilized onto the fiber surface, and the experimental results show that only specific antigen-antibody binding can introduce a measurable shift in the transmission optical spectrum of the T-LPG when it passes through the pretreated fiber segment. In the hydrogen sensing experiment, the fiber was coated with a platinum (Pt) catalyst layer, which is heated by the thermal energy released from Pt-assisted combustion of H_2 and O_2, and the resulted temperature change gives rise to a measurable T-LPG wavelength shift when the T-LPG passes through. Hydrogen concentration from 1% to 3.8% was detected in the experiment. This technique may also permit measurement of other quantities by changing the functional coating on the fiber; therefore it is expected to be capable of other fully-distributed sensing applications.

Acknowledgement

I would like to thank my advisor, Professor Anbo wang, for his tremendous help and guidance throughout my graduate study. He provided me with the great opportunity to work on this project, and offered excellent advice whenever I had difficulties in my research. His encouragement has always been my support in both my professional and personal lives. His positive and optimistic view of life inspires my research and career developing. I truly thank him for being a wonderful advisor, mentor and role model.

My sincere appreciation also goes to my co-advisor, Dr. Gary R. Pickrell, for his consistent help and support during my study in Virginia Tech. I would also like to thank the other committee members, Dr Ting-Chung Poon, Dr. James R. Heflin and Dr. Yong Xu for being very nice and supportive in my study and research.

It has been such a valuable and pleasant experience to work in Center for Photonics Technology (CPT) that I will never forget. CPT provides students with enough freedom to pursue their own research interests and offers a great research and study environment including sufficient equipment and wonderful colleagues. I would like to thank my best friends and colleagues at CPT, Kathy Wang, Cheng Ma and Bo Dong for their cherished friendship and endless help in the past 6 years. Thanks to Dr. Ming Han who was my project manager in the first two years of my research, and taught me a lot in research knowledge and skills. I would like to thank every student and staff I have worked with in CPT for their help and discussions: Dr. Evan Lally, Dr. James Gong, Dr. Brian Scott, Dr. Chalongrat Daengngam, Dr. Yizheng Zhu, Dr. Kristie Cooper, Dr. Jiajun Wang, Dr. Baigang Zhang, Dr. Jihaeng Yi, Tyler Shillig, Georgi Ivanov, Keith Depew, Guo Yu, Zhipeng Tian, Bo Liu, Michael Fraser, Islam Ashry, Ishac Kandas, Peng Lv and Chennan Hu. A special thank goes to Ms. Debbie Collins for her warm and sweet care.

I would also like to thank my dearest friends, Wei Zhang, Yanna Zhang, Bin Zhang, Juan Wang, Liguo Kong, Hong Tang, Zhengying Li, Ning Jiang and Dian Fan, for making my life in Blacksburg happy and colorful.

Finally I would like to express my deepest love and gratitude to my parents, who have provided me endless love, support and encouragement. I miss them every second in my life.

Table of Contents

List of Figures

List of Tables

Chapter 1 Introduction

1.1 Motivation

Real-time sensing of physical, chemical and biological stimuli is critical to maintaining safety and operational efficiency in today's complex industrial facilities and civil infrastructure sites. Many of these applications, such as environmental pollution measurement, health care, homeland security, flammable gas detection and industrial processes control, require various measurements at multiple locations, large spatial area coverage, capability of operation in harsh environments, low cost and in real-time. Therefore, there exists a critical need for technologies that can provide distributed measurement at multiple points.

Many kinds of sensors have been investigated for distributed sensing in the past two decades. Among these sensors, optical fiber sensors are well known for their intrinsic immunity to electromagnetic interference, high sensitivity, high resolution, resistance to chemical corrosion, small size, light weight, ease of installation and capability of operation in harsh environment[1, 2] thus attracting a great deal of research interest for distributed sensing.

According to the spatial continuity of the measurand, distributed optical fiber sensors can be divided into two categories: fully distributed fiber-optic sensors and quasi-distributed fiber-optic sensors. Compared with a quasi-distributed fiber-optic sensing system, where a series of point sensors are linked together to provide a number of specific and predetermined measurement points, a fully distributed fiber-optic sensing system can detect parameters at any points along the fiber with a certain spatial resolution. Although at present, fully-distributed fiber-optic sensing technology is hampered by some problems, such as limited sensing parameters and poor spatial resolution, it is believed to be a method which has attractive potential and future promise for further research[3].

Current fully-distributed fiber-optic sensors are mainly based on scattering in optical fibers, including Rayleigh, Raman and Brillouin scattering. However, although single-point optical fiber sensors have been demonstrated for the detection of a large variety of parameters, such as strain, temperature, pressure and other physical, chemical and biological parameters, all of the above three fully-distributed fiber-optic scattering sensing schemes are only capable for strain and/or temperature measurement[4-7]. Therefore, it is highly desirable to develop a new technology that can permit fully-distributed measurement of multiple physical, chemical and biological quantities using a single optical fiber.

1.2 Distributed Fiber-Optic Sensing

Distributed fiber-optic sensing (DFOS) is a technique utilizing the very special properties of the optical fiber to make simultaneous measurements of both the spatial and temporal behavior of a measurand field[8, 9]. It offers a new dimension in the monitoring, diagnosis and control of large, extended structures of all kinds because of its capability of determining the spatial and temporal features of a measurand field with a medium which is non-intrusive, dielectric, passive, flexible and easy to install into existing structures.

The basic theory of DFOS can be illustrated by an Optical Time-Domain Reflectometry (OTDR) system, which was the first effectively demonstrated DFOS system in 1976[2, 10]. Figure 1.1 (a) shows the schematic of an OTDR system, which consists of a pulsed laser, a detector, a coupler, data acquisition and a signal processor. In this system, an optical pulse from the pulsed laser is launched into the fiber and the light is continuously backscattered as it propagates in the fiber because of Rayleigh scattering from the small inhomogeneities and impurities in the amorphous silica which is the fiber material. The backscattered light power was detected at the launching end. Since the power of the received light decays as time increases, at the signal processor, the power of the back scattered light can be measured as a function of distance, by analyzing the time delay of the received light pulse compared with the reference point in the fiber. Figure 1.1(b) shows a typical OTDR return trace. Assume the time at which the backscattered light is received is τ, and then the fiber section from which the backscattering occurred can be identified by the distance from the launching end as:

$$s = \frac{v\tau}{2} \tag{1-1}$$

where v is the light velocity in the fiber. Therefore, if there is perturbation at any point along the fiber, the location can be determined by measuring the variation of the backscattering coefficient, and the spatial resolution depends on the temporal bandwidth of the light pulse.

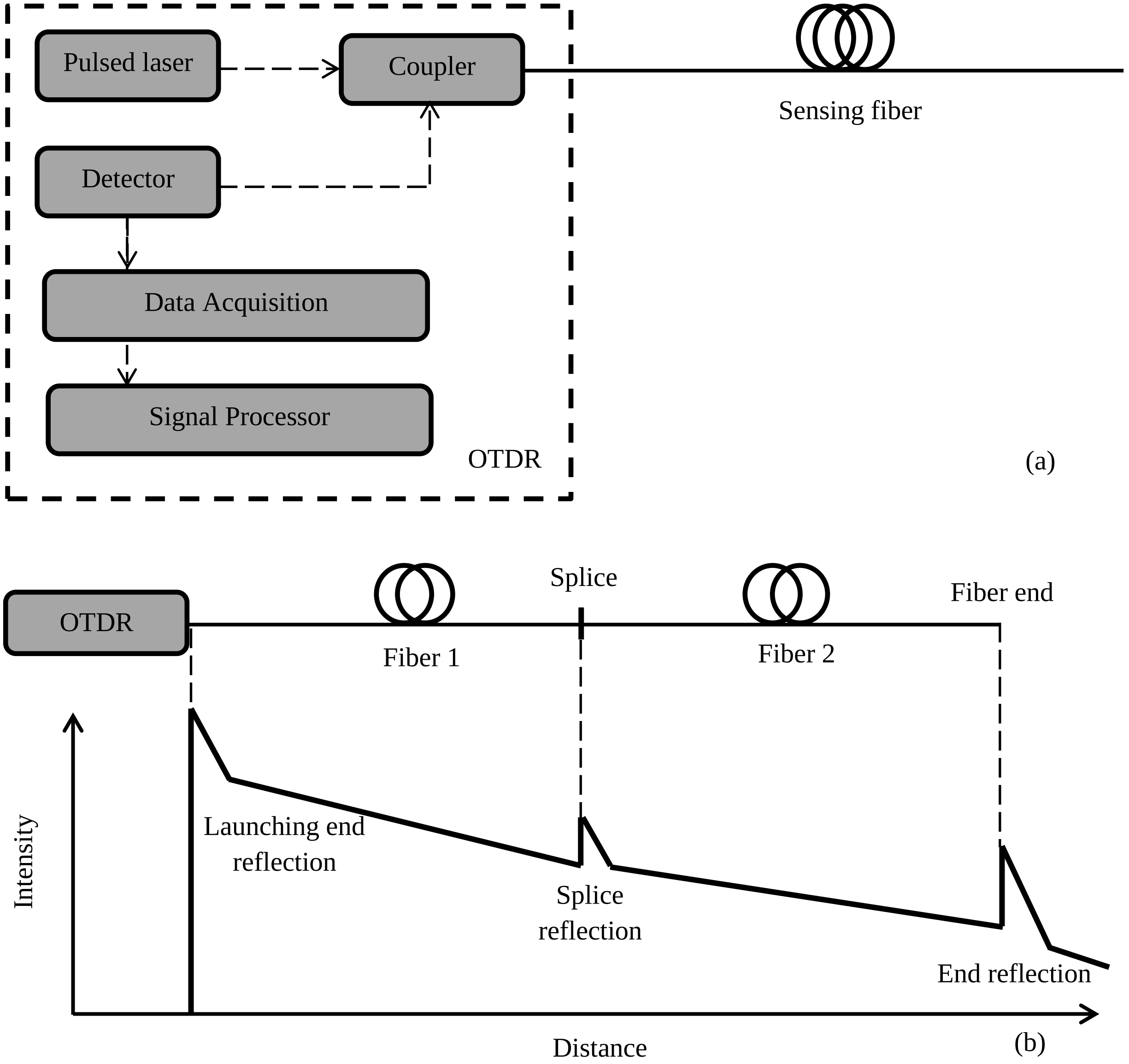

Figure 1.1. (a) Schematic of an OTDR system. (b) A typical OTDR trace.

Certainly there are many other methods for positional coding in DFOS, and there are compromises and trade-offs among them in terms of sensitivity, spatial resolution, dynamic range, etc. The specific DFOS system should be determined by the requirement of the application.

The performance parameters which characterize a given DFOS systems are listed as follows[2], as illustrated in Figure 1.2:

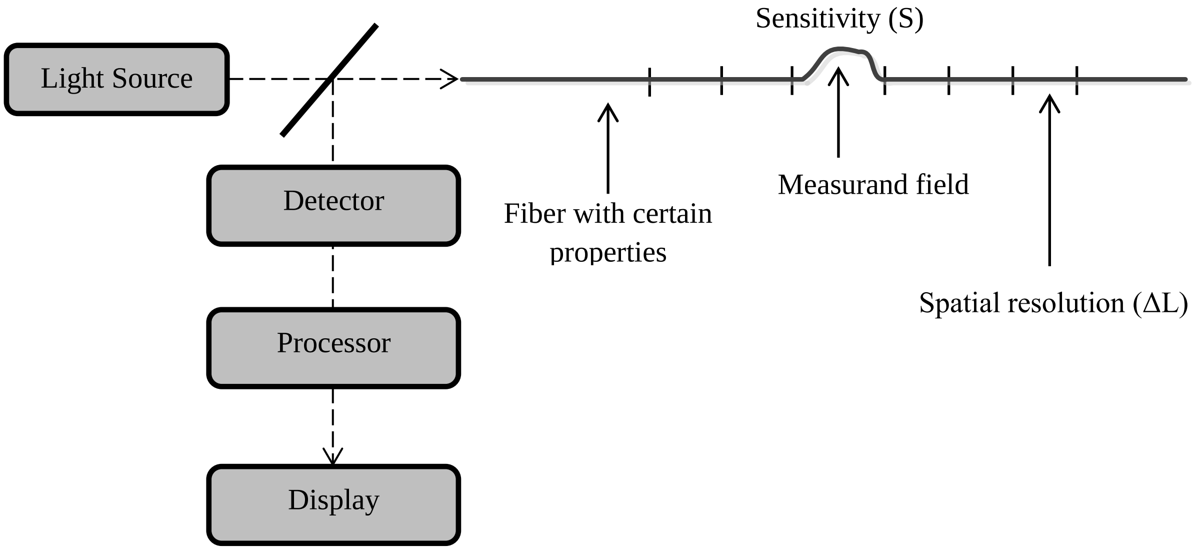

Figure 1.2. DFOS system performance parameters [1].

(1) Spatial resolution (ΔL): is the smallest length over which any sensible change of the measurand can be detected (unit: meter). It is usually considered with the total fiber length (L).

(2) Sensitivity (S): is defined as the change in the detected optical power produced by a unite change of measurand field per unite length of fiber (unite: W/field/m).

(3) Measurement bandwidth (B): is the bandwidth over which the changes in measurand field can be measured for the full fiber length (unite: Hz).

(4) System bandwidth (W): is the bandwidth of the optical detector in the system (unite: Hz).

(5) Dynamic range (D): is the ratio of maximum to minimum values of the measurand field given the required accuracy (unite: dB).

(6) Measurement accuracy: is the accuracy with which the output power of the optical detector can be measured in the face of system noise levels (%).

(7) Fiber properties: the system specifications must include a specification of the fiber used in the system, such as the attenuation, geometrical properties, coating properties, and etc.

For any given specific application, there is always a strong trade-off among the above parameters in order to optimize the system performance. For example, the sensitivity will be greater when the measurement length is longer which means a worse spatial resolution. Therefore, there is a sensitivity/spatial resolution trade-off nearly in all measurement systems.

As stated earlier, distributed fiber sensors can be divided into two types by the spatial continuity of the measurand: fully-distributed sensors and quasi-distributed sensors.

A quasi-distributed fiber sensing (QDFS) system is one that only the prescribed sections of the fiber are sensitive to the measurand field. Figure 1.3 schematically shows examples of QDFS systems. Figure 1.3(a) illustrates time domain demodulation of the individual sensors [11]; and (b) shows the frequency domain demodulation system [12].

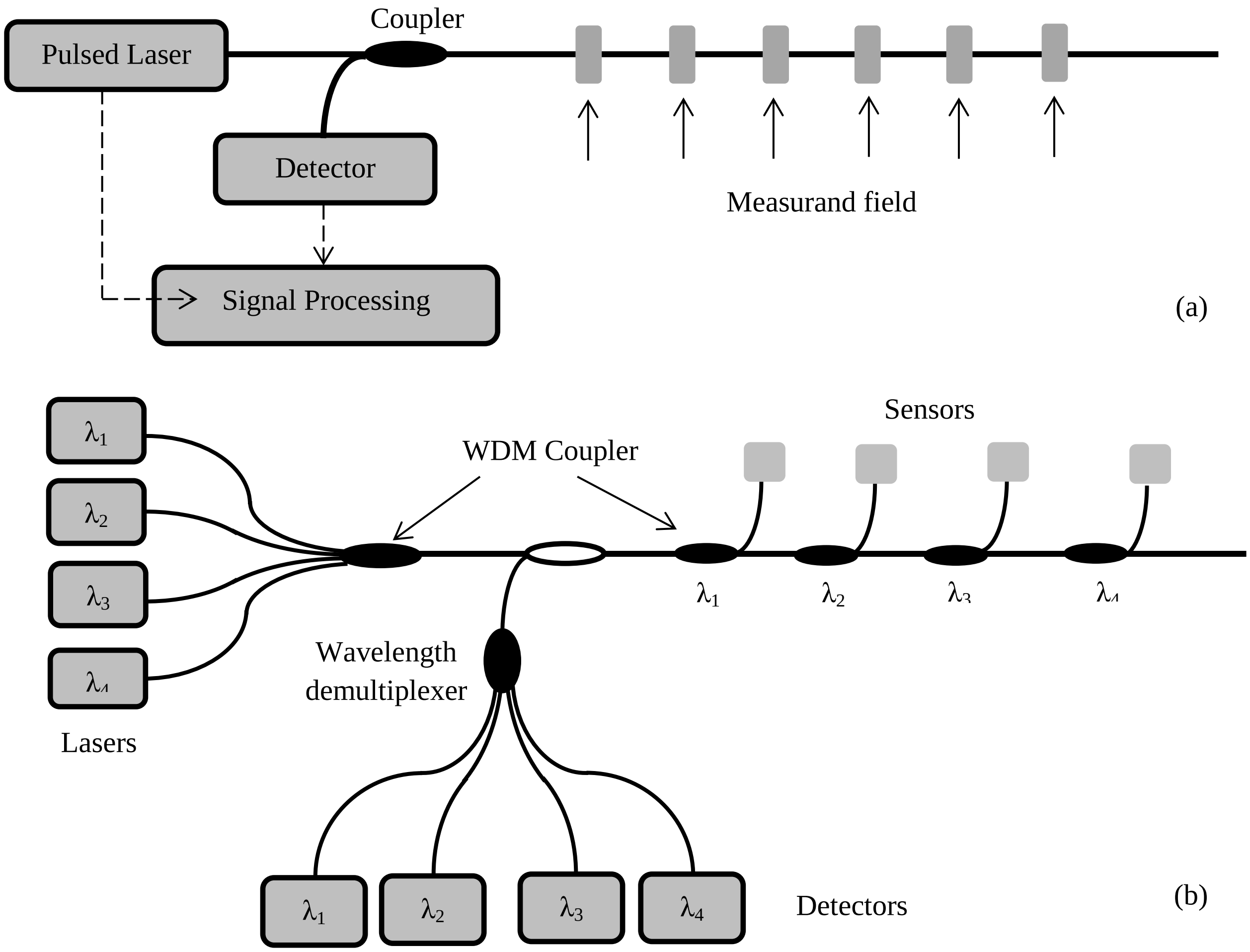

Figure 1.3. QDFS examples: (a) time domain system; (b) frequency domain system.

There are several advantages of QDFS systems. The sensitivity can be relatively high because the sensors can be characterized specifically to the wanted measurand. The sensitive fiber section can be made arbitrarily small, leading to a good spatial resolution. Because the sensitive fiber regions are prescribed, their positions are known, leading to an easy identification of the spatial location of individual sensors.

However, there are also some drawbacks in QDFS. The most important as well as the most obvious one is that all the sensing points in a QDFS system are fixed, which means the measurement can only happen in predetermined crucial locations. However, in practice, the need for detection is usually spatially random, especially in applications such as oil leakage detection, gas detection, and fire alarm. Also, there is always a limit on the maximum number of the sensors that can be multiplexed in a system, which is usually due to the attenuation of the interrogating light introduced by the sensing points or by the limitation of the demodulation techniques. And this makes QDFS not capable for long-span measurement, and even within the maximum multiplexing sensing points, to make a large number of sensors could be very time consuming and costly.

Compared with a quasi-distributed fiber-optic sensing system, where a series of point sensors are linked together to provide a number of specific and predetermined measurement points, a fully-distributed fiber sensing (FDFS) system can detect parameters at any points along the fiber with a certain spatial resolution. Since the fiber is used for both sensing and light guiding, it is also called intrinsic distributed fiber-optic sensing [3, 8]. FDFS has been under research for over two decades, with common measurands as temperature and strain. Usually, communication grade fiber can be used to measure the field over kilometers with a resolution down to the order of centimeter.

Current fully-distributed fiber-optic sensors are only capable for strain and/or temperature measurement [4-7]. Therefore, it would be highly desirable to develop a new technology that can permit long-span fully-distributed measurement of multiple physical, chemical and biological quantities using a single optical fiber.

1.3 Scope of the Research

In this research, the major objective is to develop a novel fully-distributed fiber-optic sensing platform based on traveling long-period gratings (LPGs) in single-mode optical fiber. The fixed LPG is a proven optical sensing element that can detect a variety of physical, chemical and biological parameters [13-20]. Through the novel concept of traveling LPGs, the flexible and sensitive fixed LPG is transformed into a powerful distributed sensing platform, for not only physical parameters measurement but also some chemical and biological species, such as gases, viruses, so it can extend the functionalities of current fully-distributed sensing schemes and beyond temperature and strain.

The contents of this dissertation are organized into five chapters.

Chapter 1: This chapter describes the motivation of the research with an introduction to the importance and needs of a novel fully-distributed fiber-optic sensing scheme, followed by the objective and scope of my research.

Chapter 2: This chapter reviews several mainstream fully-distributed fiber-optic sensing technologies, the current situation of biological and chemical fiber-optic sensing, and the principle of traditional LPG sensors.

Chapter 3: A detailed description of the proposed fully-distributed fiber-optic sensing system based on traveling acoustic LPG is given in this chapter, including the principle of acoustically generated LPG and the sensing scheme.

Chapter 4: Experiments using this novel sensing system on physical, biological and chemical sensing parameters are described in this chapter, and the experiment results are provided.

Chapter 5: This chapter summarizes the entire thesis and also suggests areas of future research.

Chapter 2 Research Background

2.1 Fully-Distributed Fiber Sensing

Most FDFS systems are based on scattering, in which the fiber's scattered light is sensitive to external parameters to be measured at any point along the fiber with a certain spatial resolution. Figure 2.1 shows the typical spectrum of light scattering. In optical fibers, Brillouin and Raman scattering are 20dB and 30dB weaker than Rayleigh scattering respectively. Based on the types of the scattering mechanisms, which are Rayleigh scattering, Raman scattering, and Brillouin scattering, FDFS systems can be divided into three classes accordingly:

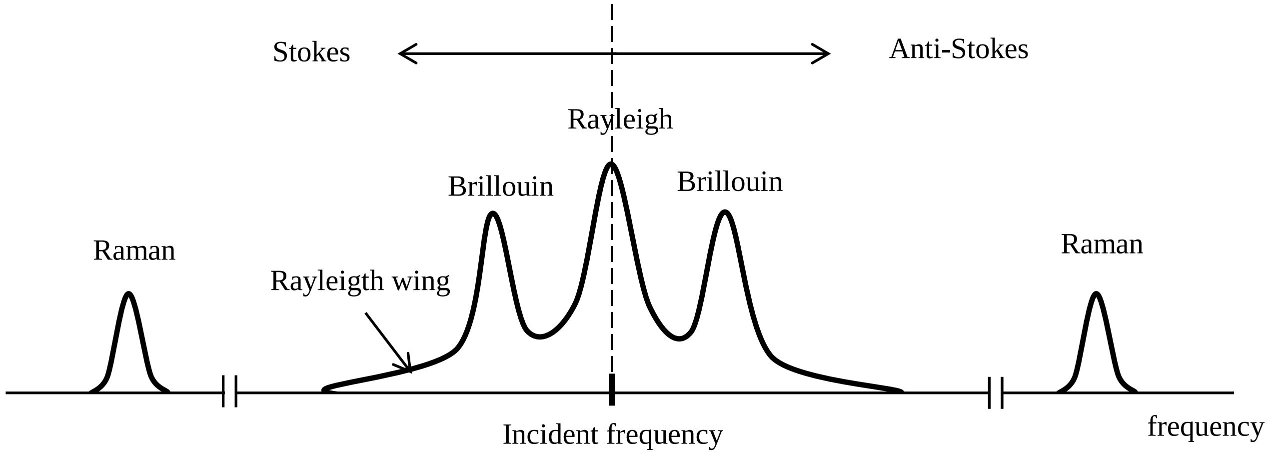

Figure 2.1. Typical scattering spectrum.

2.1.1 Raleigh scattering based systems

Rayleigh scattering is an elastic scattering process in optical fiber due to the fluctuation in the index profile along the fiber. Therefore, the scattered light has the same wavelength as the incident light, and FDFS systems using Rayleigh scattering are also called linear backscattering systems. In most this type of systems, the detected signal is the time-varying power intensity or the state of polarization of the back-scattered light. The demodulation techniques include optical time domain reflectometry (OTDR), optical frequency domain reflectometry (OFDR) and polarization optical time reflectometry (POTDR). The sensing parameters include temperature, strain and pressure.

OTDR technique has been reviewed in Chapter 1, so the following section mainly reviews the POTDR and OFDR techniques. Figure 2.2 shows a typical arrangement of a POTDR system [21]. In fact, POTDR was the first FDFS system in the laboratory by Rogers in 1980 [21], which was based on detecting the variation of polarization state along the fiber, and he also pointed out its potential for distributed sensing of temperature (via the temperature dependence of the elasto-optic effect), lateral pressure (via the elasto-optic effect), magnetic field (via Faraday rotation) and electric field (via the Kerr quadratic electro-optic effect). Different from the OTDR, which detects the power of the backscattered Rayleigh scattering of a propagating light pulse; POTDR measures the polarization state of the backscattered light, which gives the spatial distribution of the polarization state of the backscattered light. In a POTDR system, a broadband frequency laser whose linewidth is about 0.1nm is used as the light source to create a polarized light pulse. The fiber loss is modulated by the local polarization state change and detected by backward Rayleigh scattering. If disturbance occurs in any location, the local state of polarization (SOP) will be modulated. Therefore, any external field that modifies the polarization properties of the fiber can be measured in POTDR, such as strain, temperature, electric field and magnetic field.

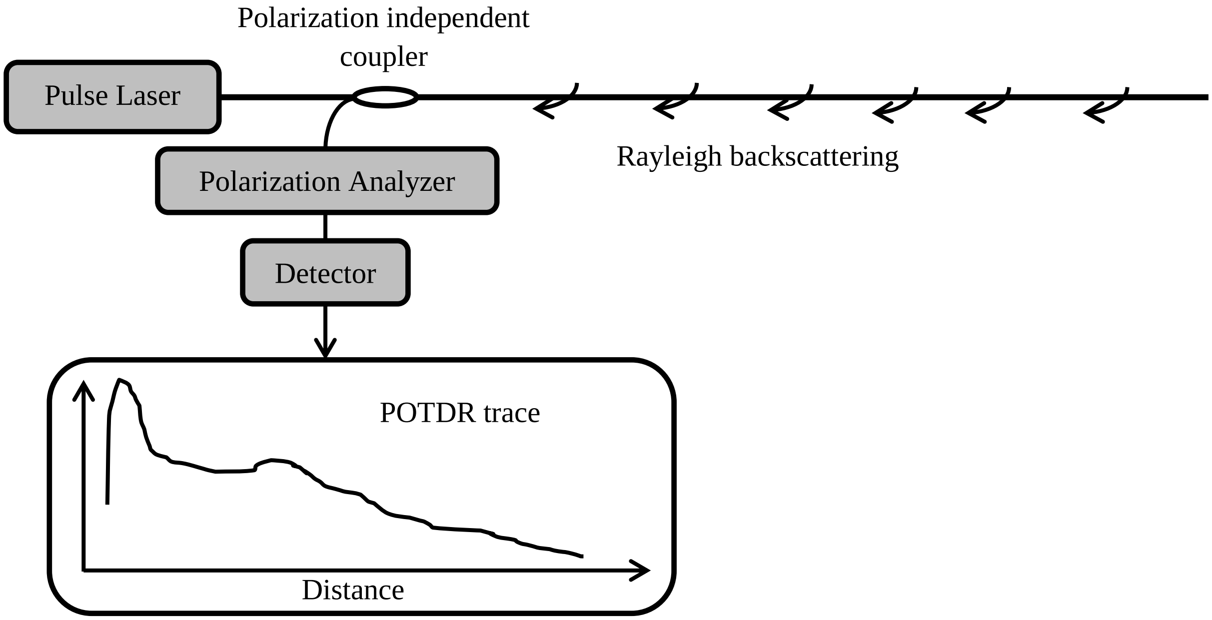

Figure 2.2. Schematic of a typical POTDR system.

Rayleigh scattering based OTDR and POTDR systems usually detect the intensity or the state of polarization of the back-scattered light. However, the power intensity of the light is also influenced by many other factors, such as the fluctuation of the light source, bending of the fiber and the optical connections along the optical path. The POTDR technique which received extensive study for distributed sensing in 1980s, the research efforts on it seem to diminish after 1990s due to its two critical drawbacks when used as a sensing method [3, 8]. One is the extremely low signal to noise ratio (SNR). Because Rayleigh scattering is essentially a weak signal, for example, about 70dB below the input laser power for 1m standard SMF working at 1550nm[22]. Rayleigh scattering is also a random process coming from the microscopic inhomogeneity in the fiber, which means it is noisy intrinsically. Therefore, in order to reach a reasonable SNR, a large spatial length should be covered, which, however, will reduce the spatial resolution significantly. In addition, POTDR requires using single mode fibers, which when used with narrow bandwidth lasers, have troublesome problems on application length due to coherent addition from multiple Rayleigh back scattering centers[23]. Besides, the fiber SOP appears to drift by itself with time, so POTDR is not a good choice for static process sensing. It may be used for dynamic measurement such as a distribution vibration sensor with 2km sensing length and 10m spatial resolution to detect 5kHz vibration frequency and double events[24]. But because the SOP change in one position will affect the following positions, this induces a significant location uncertainty, even in the dynamic measurement. So POTDR is mostly used in the communication field for locating fiber sections with high polarization mode dispersion (PMD) which is a limiting factor for high speed fiber communication systems.

OFDR in single-mode fiber was reported by W. Eickhoff in 1981 for the first time[25], as a method to measure the spatial distribution of the Rayleigh scattering and the fiber loss. After that, it has been investigated and commercialized for numerous monitoring applications. There are two main classes of OFDR systems: coherent OFDR and incoherent OFDR. Most OFDR systems based on Rayleigh scattering are of the first category, and coherent OFDR is mainly used in systems using Raman or Brillouin scattering, which will be introduced later.

The need for short spatial resolution of millimeter scale pushed the interest in OFDR systems. Because such a small spatial resolution in OTDR systems would require very narrow pulse (<1ns) light source and the corresponding high speed detection system, plus a data acquisition card with 10GHz bandwidth and tens of GS/s sampling rate, will make the whole set very expensive. While OFDR offers an alternative solution for a high spatial resolution sensing system by detecting the frequency response of the sensing fiber and converting it into the time/spatial domain response by Fourier transform.

A typical coherent OFDR system is schematically shown in Figure 2.3. In the system, a continuous wave (CW) tunable laser whose optical frequency is linearly swept in time without mode hopping is used as the light source. This frequency-modulated light is split by an optical coupler into two paths: the reference path and the sensing arm. In the sensing path, the light is further split to interrogate the fiber under test and return the backscattered light. The backscattered light and the light from the sensing arm coherently interfere with each other when recombined at another coupler. And the interference signal contains the beat frequencies which appear as peaks at the Fourier transform spectrum of the time-sampled received signal from the photodetector. OFDR is a promising technique for applications demanding for high spatial resolution (millimeter-level).

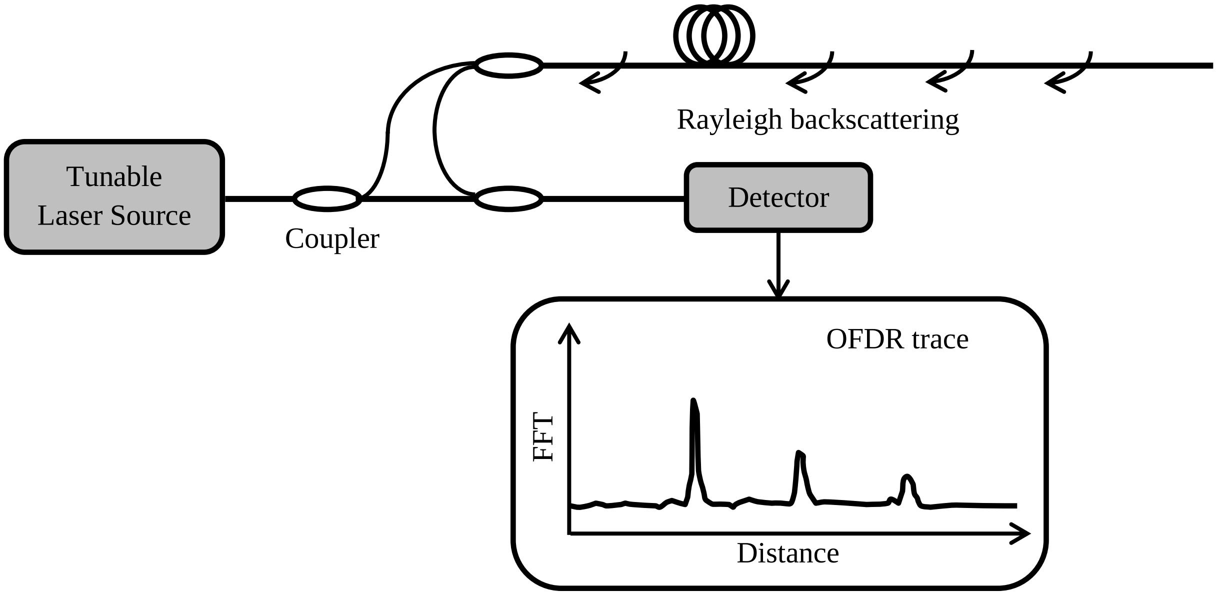

Figure 2.3 Schematic of a typical OFDR system.

OFDR can be used to detect temperature, strain, beat length and high order mode coupling in tapered fibers. It is an excellent choice for short sensing lengths (<100m), and longer measurement distance (5km) is possible at the cost of spatial resolution and temperature/strain resolution[26]. Its spatial resolution is determined by the frequency tuning range and chromatic dispersion. The maximum sensing length is limited by the phase noise of the laser[27]. A major drawback for Rayleigh scattering based OFDR is that its maximum measurement range is limited to half the coherence length of the optical source. Another problem is the polarization dependence. Because of the coherent detection scheme, the intensity of the measured signal is strongly affected by the state of polarization (SOP) of the backscattered light with respect to the reference light. If the SOP of the light from the sensing arm and the reference arm are orthogonal at the detector, their interference will completely vanish. So in order to solve this problem, the sum of the reference and sensing light is split into two orthogonal polarization states and detected by two photodetectors respectively [28].

2.1.2 Raman scattering based systems

Raman scattering is an inelastic scattering process in fiber by vibrating molecules in the fiber material, for example thermally driven molecular vibration in silica glass. The process involves a material transition from an initial state to a final state, which absorbs an incident photon and emits two new photons and thus the incident light is scattered into light at a longer wavelength termed Stokes light and light at a shorter wavelength termed anti-Stokes light [4, 29], as shown in Figure 2.4.

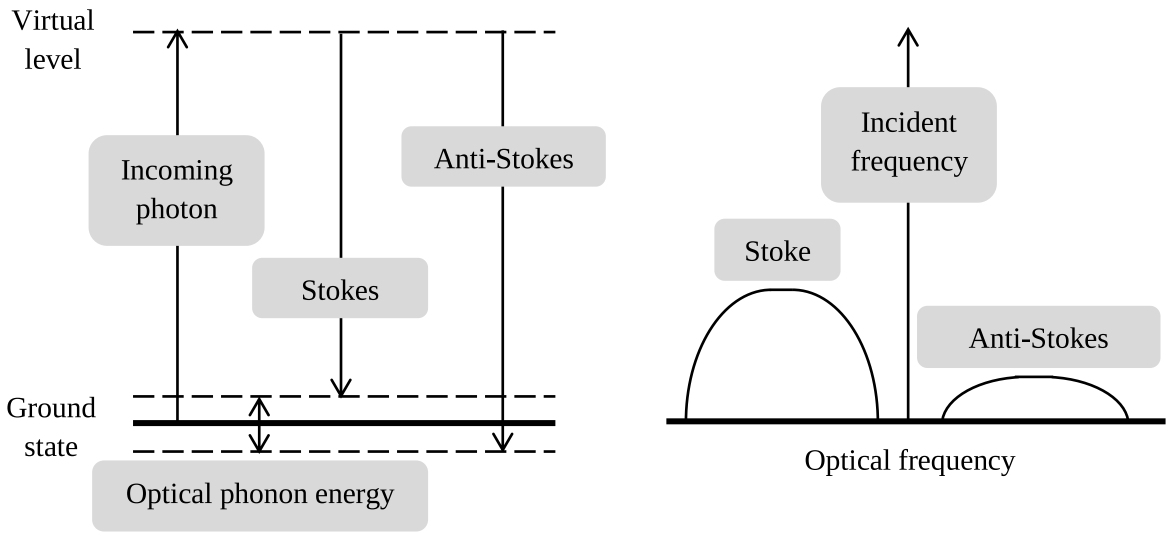

Figure 2.4. Schematic of spontaneous Raman scattering process.

The intensity ratio of Stokes and anti-Stokes light can provide an absolute measurement of temperature around the fiber with the following relationship[4]:

$$R(T) = \left(\frac{v_a}{v_s}\right)^4 e^{\left(\frac{hv}{kT}\right)} \tag{2-1}$$

where R is the ratio of Stokes power and the anti-Stokes power, v_a and v_s are the anti-Stokes and Stokes optical frequencies respectively, h is the Planck constant, v is the optical frequency of the incident light, k is Boltzmann constant, and T is the absolute temperature in the core of the fiber where the detected light is scattered.

From Equation (2-1) we can see that R is not related to the incident light intensity, the power attenuation and the fiber material composition, which is an advantage of this type of systems. By using filters to select Raman scattered light and eliminate other scatterings, the temperature sensitivity of the measured signal can be greatly enhanced. The first distributed Raman scattering based temperature sensor was demonstrated in 1985[4, 29]. Distributed temperature sensors based on Raman scattering are now well established as successful sensors technically, and are commercially available. They are widely used for temperature monitoring in oil wells and energy pipelines[30]. The highest spatial resolution for Raman OTDR is 0.24m for 135m sensing length and temperature resolution of 2.5°C[31]. A main drawback of Raman scattering is the low intensity which is usually 20 to 30dB weaker than the Rayleigh scattering signal, and thus causes a low signal to noise ratio (SNR) and limited sensing length in a Raman scattering based distributed sensing system [32].

The early demonstration of Raman scattering based systems used the OTDR demodulation technique, and a typical system scheme is illustrated in Figure 2.5. A high power probe laser launches a pulsed light into the sensing fiber. In the backscattered Raman signal, the Stokes component is only weakly dependent on temperature while the anti-Stokes component shows a strong relation to temperature. They are then separated by a wavelength-selective optical filter, after which they are detected by two detectors respectively, and their ratio is computed [33]. The location information is derived from the time of the pulse propagation time in the sensing fiber.

Typically, the wavelength difference between Stokes and anti-Stokes components is about 200nm at 1550nm depending on the fiber type. And the temperature difference of the Stokes and anti-Stokes ratio is comparable to the fiber loss difference at their wavelengths (0.2dB/km at

1550nm, 0.4dB/km at 1310nm), which is about 0.8%/°C at room temperature in SMF-28[4, 29]. So the reflected Stokes and anti-Stokes light pass through the same fiber length with different attenuation, and it would introduce an error if the temperature information is simply decoded from their reflected ratio without taking this attenuation difference into consideration. A few methods have been proposed to solve this problem such as the dual end method [33], the double light source method [34, 35], and the single light source for either Stokes or anti-Stokes method [36].

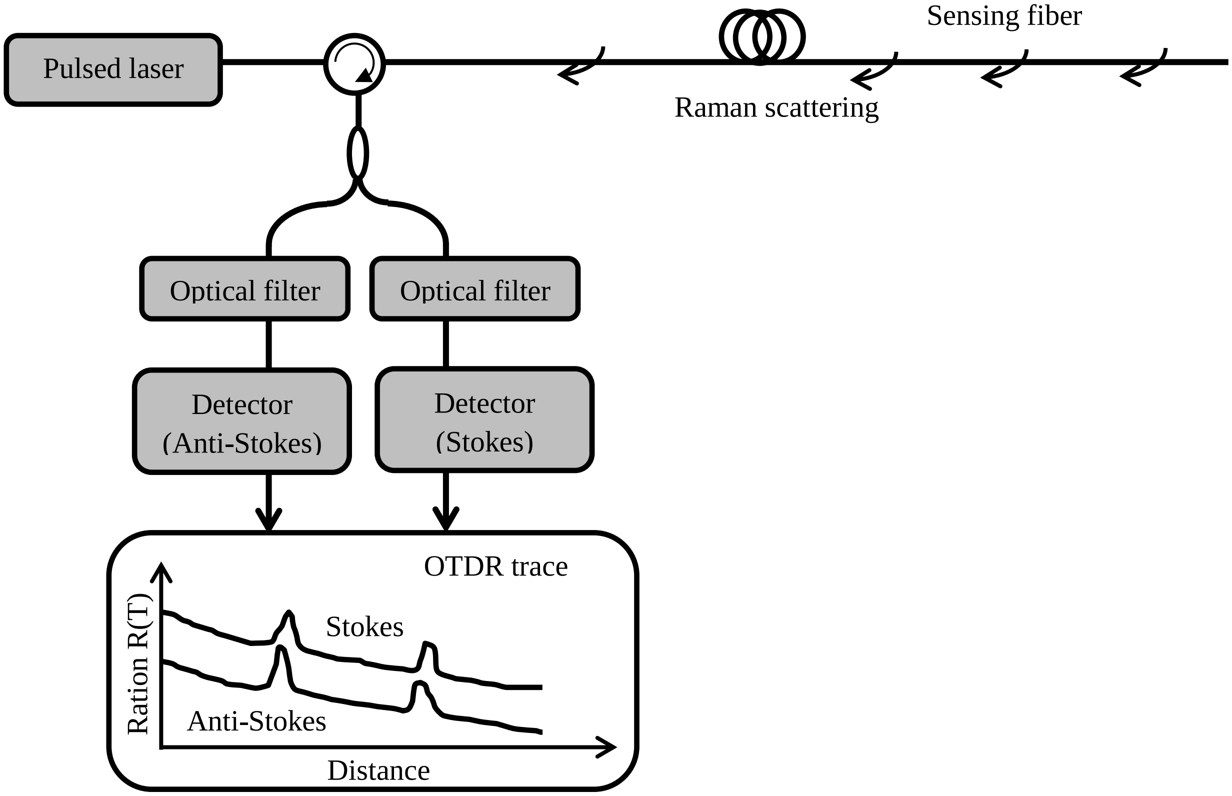

Figure 2.5. Schematic of a typical Raman OTDR system.

In the early demonstrations of Raman OTDR, multi-mode fiber was used to increase the collection of backscattered photons and pump lasers at 800-900nm wavelength were used so that high performance silicon avalanche photodiodes (APDs) could be used for detection[4]. The typical measurement range is limited to ~10km, which is due to the fiber loss, and intermodal dispersion for multi-mode fiber. Later, telecom-grade low-loss single-mode dispersion shifted fiber and optical amplification in combination with coded pulses was implemented to increase the measurement distance to 40km [37]. Raman OTDR's spatial resolution is mainly determined by the convolution of the laser pulse width with the response function of the detector. Current commercially available Raman OTDR systems have typical spatial resolution of 5m over distance up to 30km and measurement time is in the order of minutes [38]. Most recently, the spatial resolution has been significantly improved to the order of centimeters over several meter's measurement distance by using multi-photon [39] and single-photon counting techniques [40].

Different from Rayleigh scattering based OFDR, which is classified as 'coherent OFDR' as mentioned previously, OFDR systems based on Raman or Brillouin scattering are identified as 'incoherent OFDR'. In coherent OFDR, a continuous wave (CW) laser is used as the probe light source whose intensity is modulated by a RF signal. The frequency of the RF signal is changed periodically over a certain frequency range either continuously [41] or stepwise [42]. The sinusoidally modulated probe signal is launched into the sensing fiber, and the backscattered Stokes and Anti-Stokes signals are detected separately as a function of the RF modulation frequency. The detectors are usually avalanche photodiodes (APDs) because Raman signals are fairly weak. The frequency response of the backscattered signal is processed at the network analyzer, and the inverse Fourier transform of the frequency response then gives the time-domain impulse response. Figure 2.6 is a typical system schematic of Ramen scattering based OFDR.

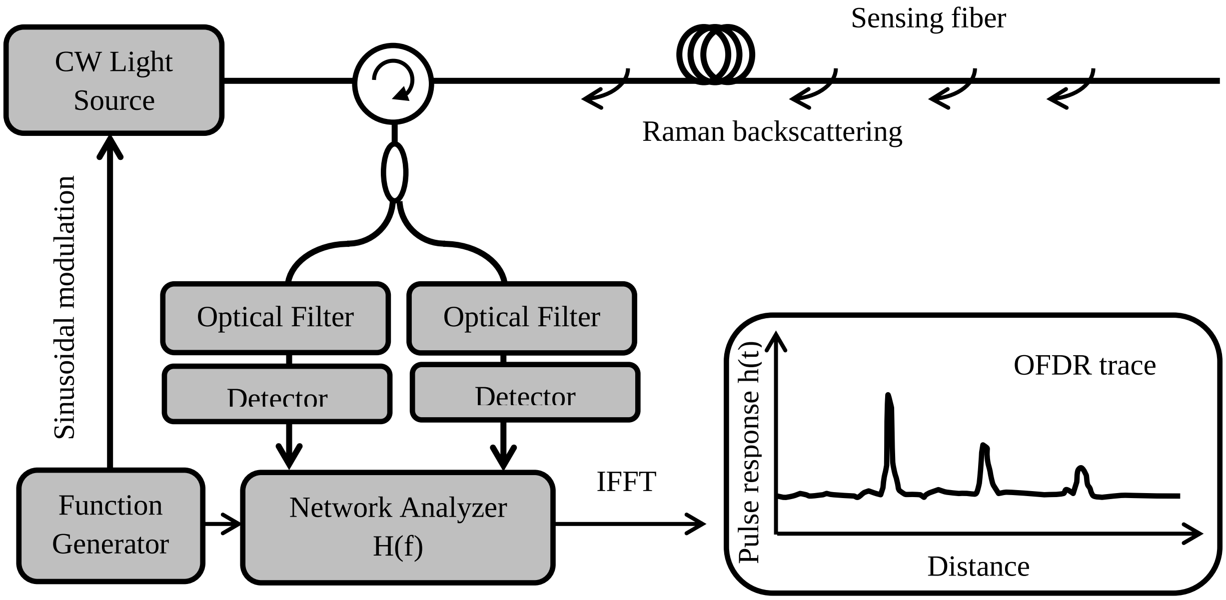

Figure 2.6. Schematic of a typical Raman OFDR system.

As mentioned before, the major advantage of Rayleigh scattering based OFDR (coherent OFDR) over OTDR is its small spatial resolution. While the key advantage of Raman OFDR (ROFDR) over Raman OTDR (ROTDR) is the possibility of using narrow-bandwidth operation which can reduce the noise and thus a more efficient data averaging. For ROTDR, broad-band measurement is necessary to resolve pulse rising time of several nanoseconds. But in ROFDR, the resolution bandwidth is the bandwidth of the down-converted intermediated frequency (IF) signal which can be analyzed in a very narrow frequency band (e.g., 1kHz). Here is an example [43]: In ROTDR, for 10km sensing fiber, 5ns pulse width is used to have a 1m spatial resolution. It takes about 0.1ms for the pulse to propagate to the end of the fiber and back. And the pulse response of 1m long fiber length takes 10ns propagation time. Therefore, the total measurement time for 20,000 single pulses is 2s, but the effective averaging time is only 0.2ms. While in the case of ROFDR, the measurement bandwidth can be adjusted to 10kHz for the IF signal, corresponding to a measurement of 0.1ms which is the same as the transient time of the sensor system. So the total measurement time is 0.2ms for each pulse. In order to have 1m spatial resolution, 10,000 single frequencies are needed for the measurement. So the total measurement time is also 2s, but the effective averaging time is 1s, which is far more than 0.2ms in the ROTDR case. Therefore, in the same total measurement time, the noise level in ROFDR case is far lower than that in ROTDR. Another advantage of ROFDR is that no high speed optical components or fast data acquisition or digital sampling techniques are required. In ROFDR, components of frequency of several hundred MHz are used, and they are inexpensive, less trouble-prone and easy to get.

2.1.3 Brillouin scattering based systems

Brillouin scattering is also an inelastic scattering process caused by the refractive index variation which is induced by the acoustic wave traveling along the fiber. Therefore FDFS systems based on Brillouin scattering and Raman scattering are also called nonlinear scattering FDFS systems. Brillouin scattering process is illustrated in Figure 2.7, which is similar to but fundamentally different in nature from that of Raman scattering process.

In Brillouin scattering process, the microbendings of the acoustic wave traveling in the optical fiber can form a periodic structure which is similar as a fiber Bragg grating, and according to Doppler's effect, this moving grating structure will result in a frequency shift of the scattered light from the incident laser. When the acoustic wave travels and the light travel in the same direction in the fiber, the scattered light frequency is down-shifted, and is up-shifted when one traveling in the opposite direction [32].

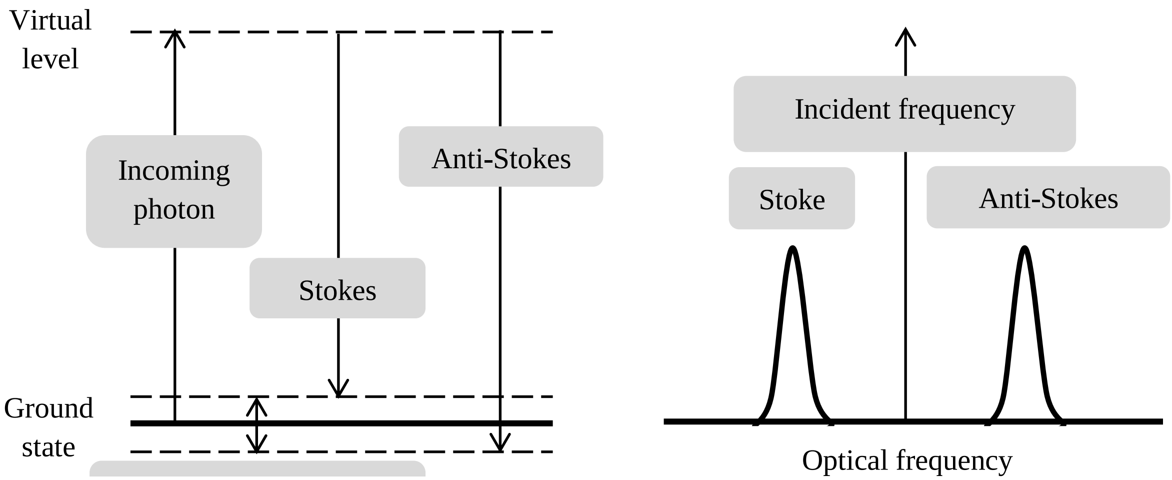

Figure 2.7. Schematic of Brillouin scattering proces.

The frequency difference between the incident light and the scattered light is called Brillouin frequency, which is given by [32]:

$$v_B = \frac{2nV_A}{\lambda} \tag{2-2}$$

where n is the refractive index of the fiber core, V_A is the acoustic velocity in the fiber, and λ is the wavelength of the incident laser. For standard single-mode optical fibers, at room temperature, Brillouin frequency is 12800MHz at 1319nm and 10850MHz at 1550nm. It is also a function of both temperature and strain experienced by the fiber [44-46], which is described as:

$$\begin{aligned} v_B(T) &= v_B(T_r)[1 + C_T(T - T_r)] \\ v_B(\varepsilon) &= v_B(\varepsilon_r)[1 + C_\varepsilon(\varepsilon - \varepsilon_r)] \end{aligned} \tag{2-3}$$

where T is temperature, ε is tensile strain, T_r and ε_r are the reference temperature and strain respectively, and C_T and C_ε are the temperature and strain coefficients respectively. Although the effective refractive index n also changes with temperature and strain, the dominating effect is induced by the material density change which influences the acoustic velocity V_A [47]. Therefore, by measuring the Brillouin frequency, Brillouin scattering based FDFS systems can be used for temperature or strain sensing. Moreover, temperature and strain can be monitored simultaneously, which is an important advantage of Brillouin scattering based FDFS systems[45].

There are two kinds of scattering in Brillouin scattering. One is Spontaneous Brillouin scattering, which is induced by the acoustic noise coming from the Brownian motion of molecules in the silica fiber, and it is usually about 20dB weaker than the Rayleigh scattering. The other is stimulated Brillouin scattering, which is the process following the spontaneous scattering due to the electrostriction effect of silica fiber material[32]. Both these two Brillouin scatterings have been used in distributed temperature and strain sensing systems along a communication-grade fiber [48].

The first distributed Brillouin scattering sensing system was based on stimulated Brillouin scattering, which was demonstrated in 1990 by researchers in NTT Communication Lab in Japan called Brillouin optical time domain analysis (BOTDA). Distributed temperature measurement with 3^{o}C temperature resolution and 100m spatial resolution over 1.2km sensing length was demonstrated [6]. In 1992, the same group proposed another system called Brillouin optical time domain reflectometry (BOTDR), and the sensing length was increased to 11km with a similar spatial resolution. Figure 2.8 shows typical the schematics of BOTDR and BOTDA systems.

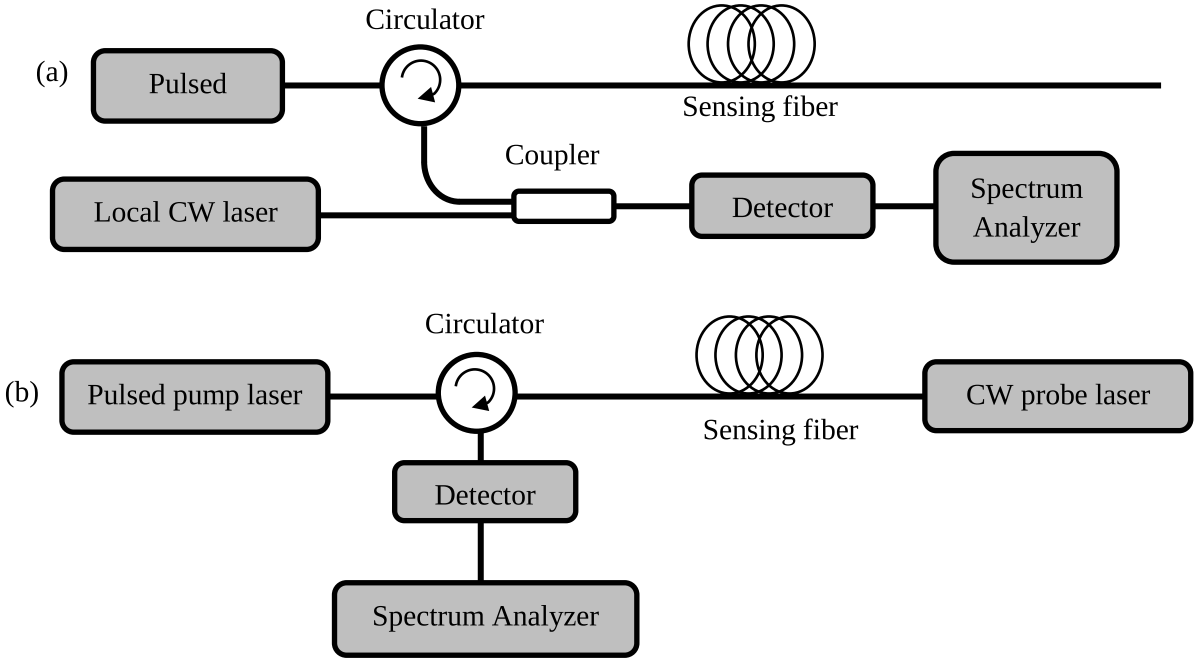

Figure 2.8. Schematic diagram of (a) BOTDR system and (b) BOTDA system.

In a BOTDR system, there is only one light beam injected into the sensing fiber, and it is pulse modulated. When the pulse is propagating along the fiber, its Brillouin Stokes wave at different locations is backscattered, and beat with a local CW laser, whose optical frequency is adjusted to around the frequency of the Stokes wave. Their beat signal is detected by a photodetector, and mapped in a spectrum analyzer, and the measurement of location information is the same as that in OTDR systems. Typically, the detected backscattered wave is spontaneous Brillouin scattering in BOTDR systems.

In a BOTDA system, a pulsed light at frequency v_p is injected from one end of the sensing fiber as pump light, and a CW light at v_{CW} is launched into the other end as probe light. The frequency of the CW light is slowly tuned, and when it is tuned to satisfy the condition $v_{CW} - v_p = v_{B,}$ where v_B is the Brillouin frequency, the pulsed light is amplified through the Brillouin gain mechanism, and the intensity of the CW pump beam will be reduced. Therefore, by monitoring the CW light intensity, the position information can be obtained from the time delay between the launching of the pulsed light and the regions where the CW light power is reduced, which corresponds to the round-trip time for the light travel to and from that specific region. After reconstruction of the Brillouin loss spectra of the CW light at specific locations, distributed measurement is enabled.

Similar to ROFDR, there is also Brillouin Optical Frequency Domain Analysis (BOFDA), which is also a 'coherent' OFDR technique. The system diagram is similar to that of ROFDR, as illustrated in Figure 2.9. The difference is that BOFDA is used to detect stimulated Brillouin scattering, so there are two lasers whose output light is counter-propagating in the sensing fiber. And the intensities of the two beams are detected and fed into a network analyzer which calculates the baseband transfer function by the ratio of the Fourier transforms of the pump and Stokes intensities. The inverse Fourier transform is then taken to provide the temporal pulse response corresponding to a spatial response [49]. Another frequency domain system is Brillouin Optical Correlation Domain Analysis (BOCDA), in which two CW light waves with a Brillouin frequency difference are identically frequency-modulated, and stimulated Brillouin scattering occurs at the correlation peak position where the two lightwaves are highly correlated [50].

Generally speaking, compared with Raman scattering based systems, Brillouin scattering-based systems have a major advantage, which is the much stronger signal and a resultant better spatial resolution and temperature/strain sensitivity besides the strain sensing capability. For time domain systems, the first demonstration of spatial resolution substantially better than one meter (50cm) was in 1998 [51], and this was further improved to 2cm over 2km sensing fiber by using a differential pulse width pair (DPP) technique in 2012 [52]. In BOFDA systems, a 3cm spatial resolution over 9m sensing length was reported by post-signal processing method [53]. In BOCDA systems, the spatial resolution can be further improved to 1cm for short sensing length [54]. In BOTDA sensor systems, the ultimate temperature or strain resolution is limited by the maximum contribution of system SNR and fiber inhomogeneity [47]. The reported best performance is 1°C temperature resolution [55] and 20 με per meter strain measurement accuracy [56]. And simultaneous measurement of temperature and strain using polarization maintaining fiber was demonstrated with 128 με per meter strain resolution and 3.9 °C temperature resolution at a spatial resolution of 3.5m [45].

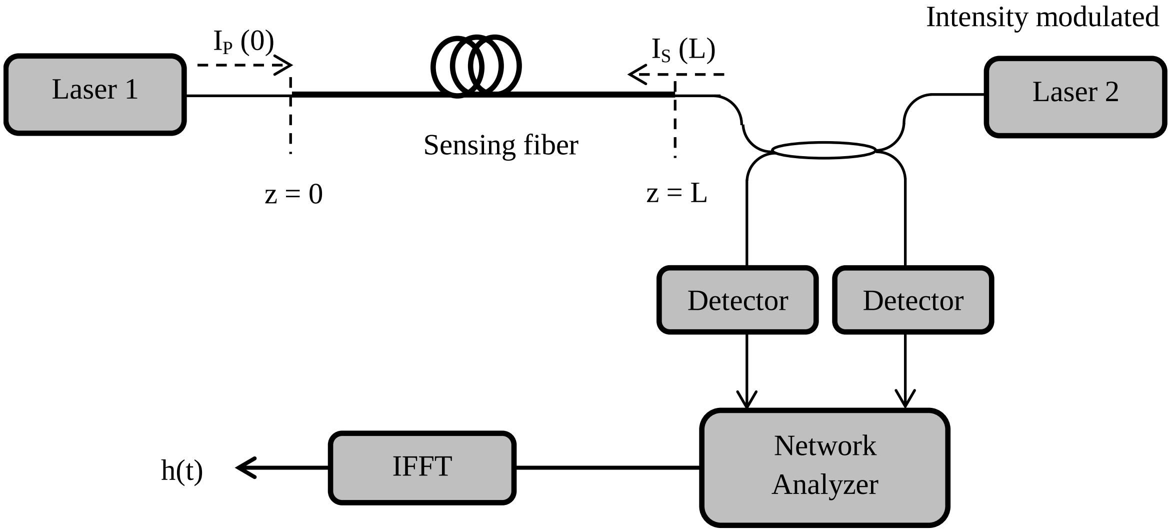

Figure 2.9. Schematic of a typical BOFDA system.

2.1.4 Problems with scattering-based FDFS

After over twenty years of research, some scattering based fully distributed sensing systems are now established as well-developed techniques, both technically and commercially. However, some major problems still remain. Some of them may be solved by further research, but some others are inherited.

One of the common problems for scattering based systems is their high cost, which greatly hampers their practical applications. This is due to the need of expensive components in the systems, such as the high speed optical detectors, the broadband electronics and digitizer requirements in OTDR systems and the narrow linewidth tunable laser in OFDR systems. Typically, the price of commercial BOTDA and Rayleigh based OFDR systems is more than $50,000. Raman based systems are less expensive, but their capability is temperature measurement only and both their measurement accuracy (~1°C) and spatial resolution (~1m) are worse than that of BOTDA and OFDR systems.

Although fiber optic sensors have been demonstrated for the detection of a large variety of parameters, such as strain, temperature, pressure and other physical, chemical even biological parameters, distributed fiber-optic sensing especially in fully-distributed manner is still only capable for strain and/or temperature measurement to date. This is mainly due to the scattering in regular single mode fibers are intrinsically not sensitive to parameters other than temperature and strain. Therefore, the solution is to use special fibers or modified regular fibers in order to do extend the FDFS to more measurands.

2.2 Fiber-Optic Biological and Chemical Sensing

Monitor of chemical and biological species is becoming more and more important in many markets including industrial process control, energy production, health care, environment monitoring and anti-terrorism, so fast, reliable, and accurate chemical and biological sensors have attracted extraordinary interest in recent years. Optical fiber-based sensors have been demonstrated for measurement of a variety of physical and chemical parameters, and possess some unique advantages due to the intrinsic characteristics of optical fibers. By researches reported in recent years, it is obvious that fiber-optic sensors have great potential in chemical and biological sensing compared with other sensors which are usually time consuming and require not only high cost equipment but also strictly trained personnel [57-61]. For convenience of discussion, all the sensors denote to fiber-optic sensors in the discussion below.

2.2.1 Fiber-Optic Biological Sensing

According to the definition from International Union of Pure and Applied Chemistry (IUPAC), a biosensor is a self-contained integrated device providing quantitative or semi-quantitative analytical information which includes a biological sensing element in direct contract with a transducer [62]. The definition, classification and nomenclature of biosensors have been described in detail [62]. Figure 2.10 is a schematic figure of a typical biosensor. At the heart of all biosensors there is a biologically active component called receptor, which plays the key role in the sensitivity and selectivity of biosensing. Receptor interacts with its target analyte, producing a chemical or physical measurable effect, which is transmitted to the transducer that can generate another signal that is proportional to the signal received. A good biosensor should return to its original state once the measurement has taken place, in other words, it can be reused. The analyte recognition mechanism and the close connection between the sensing element and the transducer are critical for biosensors.

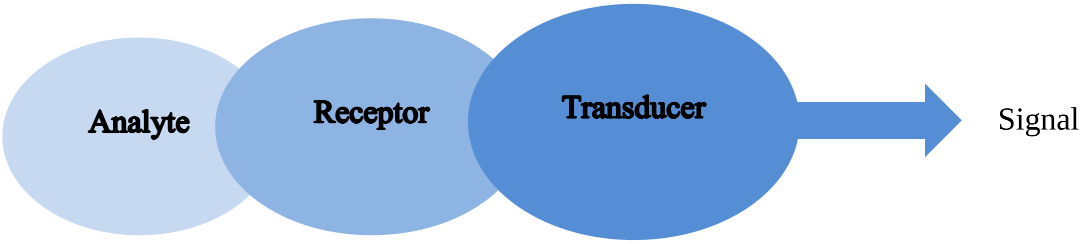

Figure 2.10. A typical biosensor structure.

Biosensors can be classified according to the different transducer types, including optical, electrochemical, piezoelectric and calorimetric. In fiber-optic biosensors, optical fibers act as the platform for biological recognition elements and medium for the light propagation, and they made great success for *in situ* and *in vivo* measurement where conventional sensors may not be appropriate. Biosensors can also be divided into many groups by the type of analytes, such as enzymatic sensors, immunosensors, DNA sensors, bacterial sensors and etc. In our experiment, we chose immunosensors, an important and intensively investigated group among biosensors.

Immunosensors are used to detect the recognition between specific antigen and antibody. An antigen is anything that makes the immune system respond to produce antibodies, and antibodies are proteins that bind to the specific antigen with high affinity. Immunosensors have superior sensitivity and selectivity because of their inherent specificity of antigen-antibody reactions with the high sensitivity of various physical transducers.

Immunosensors can be classified into four commonly used types: direct assay (a), competitive assay (b), binding inhibition assay (c), and sandwich assay (d) as shown in Figure 2.11.

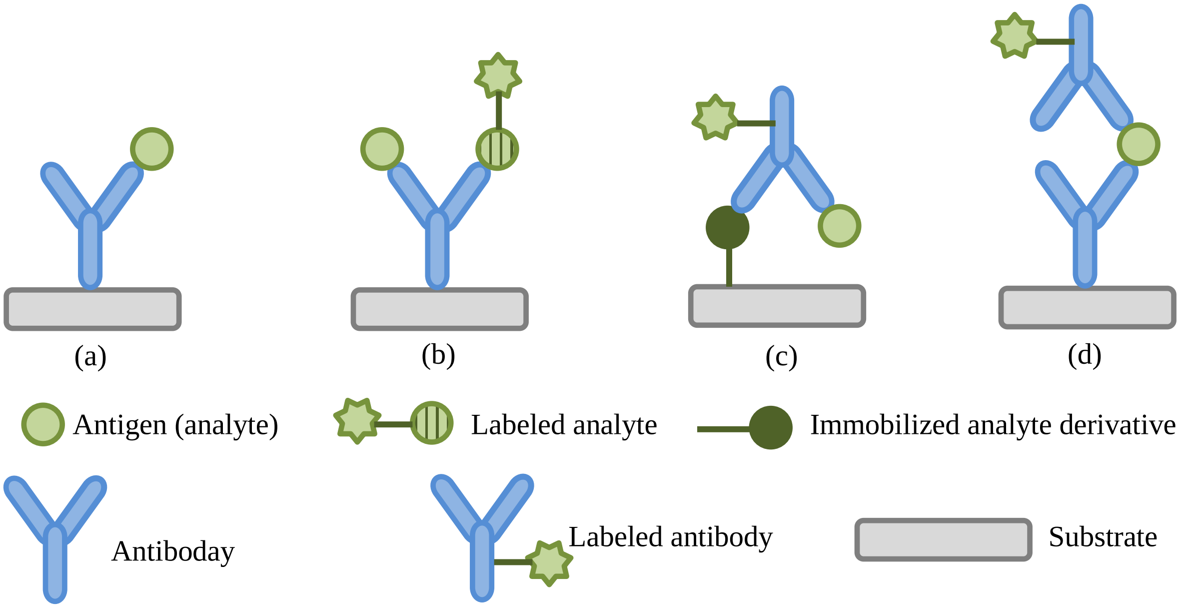

Figure 2.11. Assay formats in immunosensors: (a) direct, (b) competitive, (c) binding inhibition, (d) Sandwich

In direct immunoassay, the antigens are incubated with excess amounts of immobilized antibodies, and they can be a fluorescent compound in fluorescence-based measurement[63, 64]. Unlabeled direct assay is a relatively quick and convenient method because it does not require the time-consuming and expensive labeling process. Many techniques have been applied for unlabeled direct assay, such as ellipsometry [63], optical waveguide spectroscopy [63], resonant mirror [65], surface Plasmon resonance [66] and interferometry [67]. In competitive assay, analytes must be labeled with detectable chemicals, such as fluorescein and Cy5 [68-70], and they will compete with labeled derivative for limited binding sites of the antibodies during the incubating. Since the amount of labeled derivative bound is inversely proportional to that unlabeled analyte in the sample, the signal will decrease as the analyte concentration increases. Binding inhibition assay is an alternative test format of competitive assay, in which the antigens are immobilized and the antibodies are labeled [71, 72]. In the sandwich assay, antibodies are immobilized to the sensor, and then the sensor is incubated with the analytes, and complexes are formed between the analytes and the immobilized antibodies. At last, another labeled antibody recognizes and binds to another epitope of the analytes [73-75]. The sandwich assay requires two antibodies that bind to two different epitopes on the same antigen, which can be done by either two monoclonal antibodies that recognize discrete sites or by batch of affinity-purified polyclonal antibodies. The extent of reaction in this case is directly proportional to the amount of antigens, and the cross reactivity is significantly reduced due to the recognition of different epitopes.

The specific binding of antigens and antibodies is dependent on hydrogen bonds, hydrophobic interactions, electrostatic forces, and van der Waals forces, so it is reversible non-covalent interactions. The interactions between antibodies and antigens can be disrupted by high salt concentrations, extremes of pH and detergents. It has also been reported that chemical reagents can remove antigens bound to antibodies, which makes the sensors reusable [76, 77].

2.2.2 Fiber-Optic Chemical Sensing

According to the types of species, fiber-optic chemical sensors can be divided into three classes. The first one is sensors for gases, vapors and humidity, which currently is the major focus among the three; the second one is sensors for pH and Ions; and the third one is sensors for organic chemicals.

In the first type, the major research focuses on gas sensing which is usually referred to hydrogen, hydrocarbons and oxygen. Hydrogen is of great research interest because it is highly explosive when mixed with air and at the same time is viewed as a potential supply to the ‘hydrogen economy’ of the future. There are also some flammable alkanes remain to be the analytes for safety considerations such as methane. Oxygen and carbon dioxide are clinically highly significant blood gases, so quantitative detection for them is important for medical applications. Optical humidity sensors can always attract much attention due to their highly different applications such as control of air conditioning, quality control of food products in a wide range of industries, paper and textile industries. Vapors, often referred to as volatile organic compounds, and are sensed by optical means in order to risk of explosion.

The second type covers all kinds of inorganic ions including the proton (i.e. pH), cations and anions. Fiber-Optic pH sensors are now commercially available, but the measurement and control of pH is kind of evergreen, because there are still challenges on the limited range of pH as well as material improvement. Generally speaking, the applications of ion sensors can be very different depending on the specific intended ion, but current major interest in health care incorporating specific ions like K^+ and Ca^+.

The third type usually means sensors for organic species (mainly saccharine), pollutants, agrochemicals and drugs. For an example, a hot topic recently is glucose sensor for heal care. Because the applications focus mainly on biomedical applications, there is a tendency of viewing them as biosensors.

Chapter 3 Fully-Distributed Fiber-Optic Sensing Based on Traveling Long Period Grating

In this work, we proposed a fully-distributed sensing technique based on the propagation of an acoustically induced transient long period grating (LPG) in a regular single-mode fiber [78]. The optical transmission spectrum from the area where the LPG is propagating was shown to be sensitive to the local changes to the fiber. Besides multi-functionality, the sensing method can potentially have some other advantages, such as high sensitivity, temporariness and flexibility, low cost and capabilities of temperature and nonspecific compensation.

3.1 Long Period Fiber Grating

Fiber gratings are a special case of waveguide gratings, and have been among the most popular optical fiber devices widely used in both optical communications and fiber sensing. There are two general types of fiber gratings: fiber Bragg grating (FBG) whose grating period is on the scale of optical wavelength (generally several hundreds of nanometers), and long period grating (LPG) with a few hundreds of microns grating period typically. LPG was first observed by Hill et al. in 1990 [79], the same group who developed FBG in 1978 [80]. After that extensive research have been done on the optical characteristics, fabrication technologies, and applications of LPG. LPG has a periodically modulated refractive index profile in the core of the fiber, as illustrated in Figure 3.1(a). The periodic pattern promotes coupling between the fundamental core mode and forward propagating cladding modes. The high attenuation of cladding modes results in a series of attenuation bands at discrete wavelengths in the transmission spectrum of LPG, and each attenuation band corresponds to a specific cladding mode. A typical LPG transmission spectrum is shown in Figure 3.1 (b). The central wavelength of each attenuation band is called the resonance wavelength of the LPG, which is determined by the phase matching condition as

$$\lambda_{res} = (n_{core} - n_{cl}^{i}) \cdot \Lambda \tag{3-1}$$

where λ_{res} is the LPG resonance wavelength, and n_{core} and n^{i}_{cl} are the effective indices of the core and the *i*-th cladding modes. When the light is coupled from the fiber core into the cladding, its evanescent fields can stretch beyond the physical boundary of the fiber or into the fiber surface coating. Therefore, changes in the fiber surrounding medium or in the surface coating will shift the LPG resonance wavelength. This response to surrounding environment makes LPGs particularly attractive for sensor applications, especially in multi-parameter sensing including various physical, chemical and biological measurands.

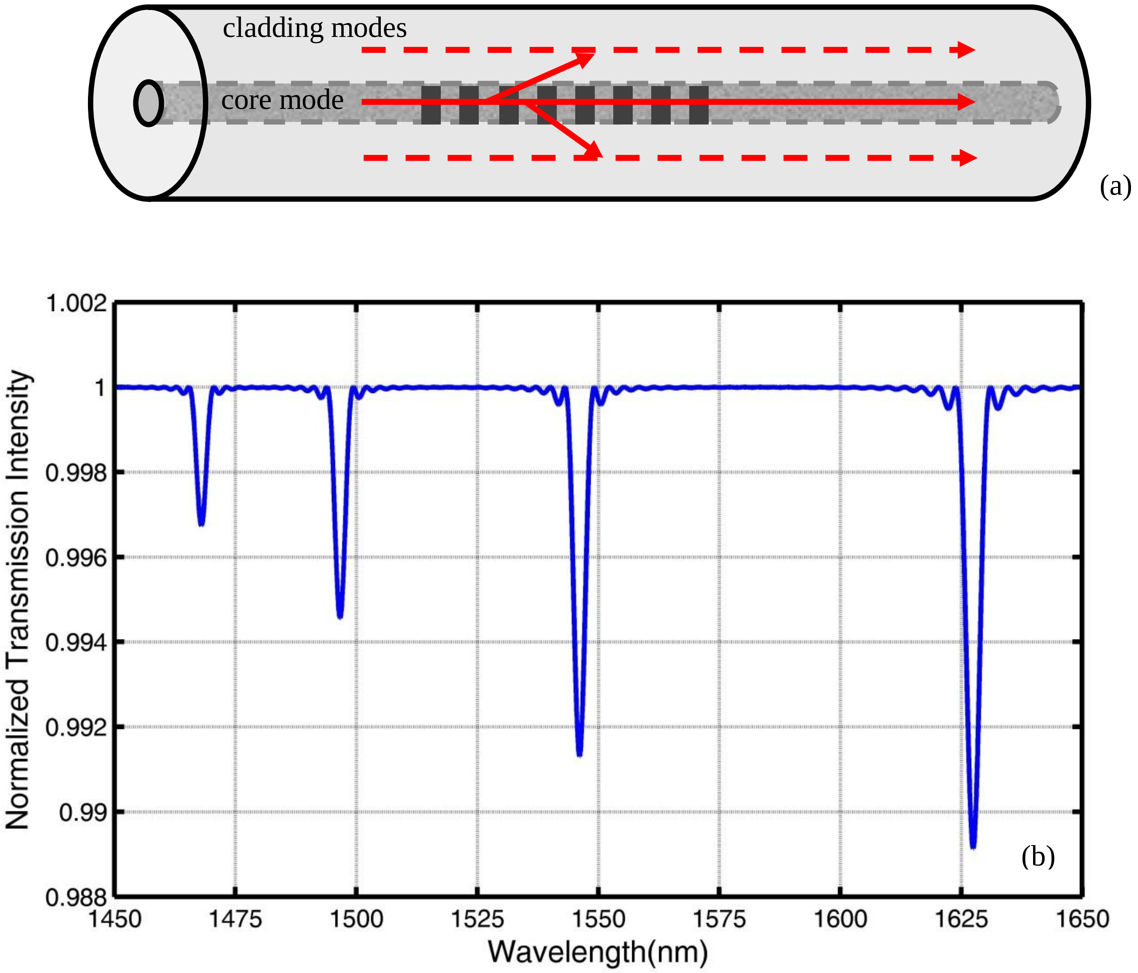

Figure 3.1. (a) Schematic of LPG operation mechanism. (b) Transmission spectrum of an LPG.

The sensitivity to a particular measurand is dependent on the core-cladding refractive index contrast, the core-cladding dimension, and the order of the cladding mode to which the fundamental core mode is coupled to. Therefore, different cladding modes exhibit different sensitivities.

Generally speaking, analytical modeling of an LPG is much more complicated than that of an FBG. Because in an FBG, the forward propagation core mode is coupled exclusively to the backward propagation core mode. While in an LPG case, the core mode is coupled to various cladding modes. And intuitively speaking, the coupling process is more like a competition among different cladding modes. Moreover, the coupling between different forward cladding modes makes the LPG modeling more complex. Eventually, at a certain wavelength, one cladding mode will have the dominant power from the core mode, determined by the grating properties and the fiber waveguide properties. Coupled mode theory has been a well-established technique to analyze LPGs, and will be discussed in detail in the following paragraphs.

To describe the cladding modes in an optical fiber, people use definition of LP modes. LP modes are considered to be transverse waves by letting E and H field on propagation direction equal to zero [81]. In a weakly guided single-mode fiber structure, an LP_{mn} mode is defined as mode of order n and within a cylindrical dielectric layer I whose radius satisfies $r_{i-1} < r < r_i$ and with refractive index n_i, as shown in Figure 3.2. And its transverse electric field components propagating along the fiber axis are given by [82, 83]:

$$\begin{aligned} U_{mn,i}(r,\phi,z) &= e^{-j\beta_{mn}z}\Psi_{mn,i}(r,\phi) = e^{-j\beta_{mn}z}\Phi_m(\phi)R_{mn,i}(r) \\ &= e^{-j\beta_{mn}z} \times \begin{cases} A_{mn,i}J_m(r\gamma_{mn,i}) + B_{mn,i}J_m(r\gamma_{mn,i}), \beta_{mn} < k_0 n_i \\ A_{mn,i}I_m(r\gamma_{mn,i}) + B_{mn,i}K_m(r\gamma_{mn,i}), \beta_{mn} > k_0 n_i \end{cases} \end{aligned} \tag{3-2}$$

where $k_0 = 2\pi/\lambda$ is the free space wavenumber, β_{mn} is the longitudinal propagation constant of the LP_{mn} mode, $\gamma_{mn,i} =(| k_0^2 n_i^2 - \beta_{mn}^2|)^{1/2}$ is the magnitude of the transverse wavenumber, ϕ is the azimuthal angle, and $A_{mn,i}$ and $B_{mn,I}$ are the field expansion coefficients determined by the boundary conditions within layer i. $J_m (r\gamma_{mn,i})$ and $Y_m (r\gamma_{mn,i})$ are the ordinary Bessel functions of the first and second kind of order m; $I_m (r\gamma_{mn,i})$ and $K_m (r\gamma_{mn,i})$ are the modified Bessel functions of the first and second kind of order m.

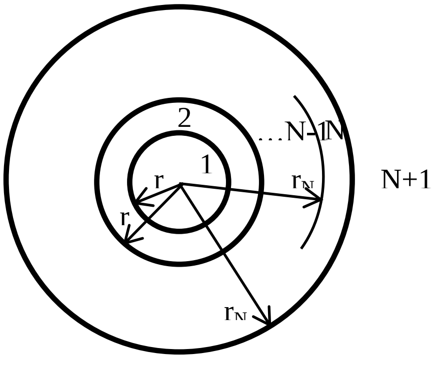

Figure 3.2. Cylindrical fiber waveguide with multilayer structure.

The interaction among the LP modes can be modeled by the coupled mode theory, in which the coupling between optical modes is proportional to their coupling coefficient K. In the coupled mode theory, each forward propagating mode (core and cladding) is assumed to have a complex form A(z), and the coupled mode equation governing the interaction of these modes is [84]:

$$\frac{dA_{\mu k}(z)}{dz} = -j\sum_{mn=1}^{M}[K^{t}_{mn,\mu k} + K^{z}_{mn,\mu k}]A_{mn}(z)e^{-j(\beta_{mn}-\beta_{\mu k})z}, \mu k = 01,\ldots,M \tag{3-3}$$

With the assumption that there is no mode coupling between forward cladding modes, which means that the coupling coefficient $K^{z}_{mn,\mu k}$ between the LP_{mn} and the $LP_{\mu k}$ modes in the propagation direction is zero. So the coupling coefficient $K^{t}_{mn,\mu k}$ can be replaced simply by $K_{mn,\mu k}$, which is derived by integrating the different mode fields over the whole fiber cross section as [85]:

$$K_{mn,\mu k} = [s_0 + s_1\cos(\frac{2\pi}{\Lambda}z)]\zeta_{mn,\mu k} \tag{3-4}$$

where s_0 and s_1 are the dc and ac components of the refractive index perturbation and $\zeta_{mn,\mu k}$ describes the field overlap between the LP_{mn} and $LP_{\mu k}$ modes within the entire fiber cross section, and is given by [84]:

$$\zeta_{mn,\mu k} = \frac{\omega\varepsilon_0}{2P_0}\sum_{i=1}^{N}n_0(r)\int_{r=r_{i-1}}^{r_i}R_{mn}(r)R_{\mu k}(r)rdr \tag{3-5}$$

where ω is the radial frequency of the light; ε_0 is the free space permittivity; P_0 is the normalized power in the LP_{mn} mode; n_0 is the refractive index of the fiber; N is the number of layers in the optical fiber structure; and $R_{mn}(r)$ and $R_{\mu k}$ (r) are the radial components of the electric field in the LP_{mn} and $LP_{\mu k}$ modes, respectively. For an LPG with air as the surrounding medium, we only need to consider two layers, which means N = 2. This is because the cladding diameter (125 μm) is much larger than the core diameter (8 μm), making the fiber outer diameter approximately infinite in regards to the position of the core-cladding boundary. n_0 is a step function along the fiber radius r, whose profile is illustrated in Figure 3.3.

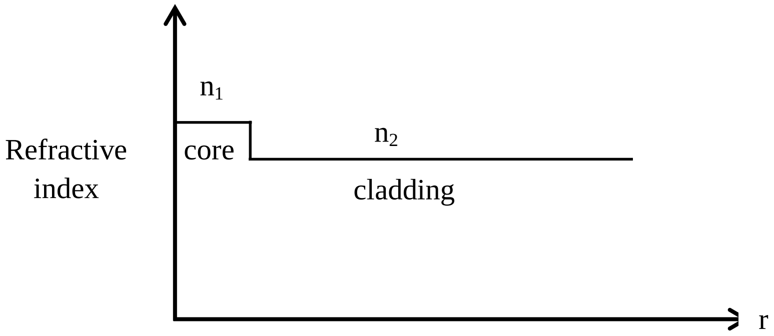

Figure 3.3. Refractive index profile of single-mode fiber.

By substituting Equations (3-4) and (3-5) into (3-3), and neglecting rapidly oscillating terms by applying common synchronous approximation, the coupled mode equation is modified as an equation system with M×M dimensions as [84]:

$$\frac{dA_{\mu k}(z)}{dz} = -j \sum_{mn=1}^{M} \begin{cases} s_0 \zeta_{mn,\mu k} A_{mn}(z), \text{if } \mu k = mn \\ \frac{s_1}{2} \zeta_{mn,\mu k} A_{mn}(z) e^{-j(\beta_{mn} - \beta_{\mu k} \pm \frac{2\pi}{\Lambda})z}, \text{otherwise} \end{cases} \quad \mu\text{k} = 01, \ldots, \text{M} \tag{3-6}$$

We can further define Q_{mn} and $V_{mn,\mu k}$ as the self-coupling and cross-coupling coefficients between different LP modes, respectively, as:

$$\begin{aligned} Q_{mn} &= -js_0 \zeta_{mn,mn} \\ V_{mn,\mu k} &= -j \frac{s_1}{2} \zeta_{mn,\mu k} \times e^{-j(\beta_{mn} - \beta_{\mu k} \pm \frac{2\pi}{\Lambda})z} \end{aligned} \tag{3-7}$$

Then the coupled mode equation system can be expressed as:

$$\begin{bmatrix} A_{01}(z) \\ A_{02}(z) \\ A_{03}(z) \\ \vdots \\ A_M(z) \end{bmatrix}_{z=0} = \begin{bmatrix} Q_{01} & V_{01,02} & V_{01,03} & \cdots & V_{01,M} \\ V_{02,01} & Q_{02} & V_{02,03} & \cdots & V_{02,M} \\ V_{03,01} & V_{01,02} & Q_{03} & \cdots & \vdots \\ \vdots & \vdots & \vdots & \ddots & V_{M-1,M} \\ V_{M,01} & V_{M,02} & \cdots & V_{M,M-1} & Q_M \end{bmatrix} \begin{bmatrix} A_{01}(z) \\ A_{02}(z) \\ A_{03}(z) \\ \vdots \\ A_{05}(z) \end{bmatrix} \tag{3-8}$$

The initial condition of the above equation is: A_{01} (z=0) = 1, and A_{mn} (z=0) = 0 for mn = 02…M. So by solving this equation set, we can calculate the electrical field of each cladding mode at a certain grating condition.

3.2 Acoustically Generated LPG

A number of techniques have been investigated to fabricate LPGs. The first demonstration of an LPG was done by a point-by-point inscribing method through the side of the fiber using a UV laser source with controlled grating period [79]. Electric arc discharge and focused infrared femtosecond laser pulses have since been used to write LPGs also on a point-by-point basis [86-89]. All of these methods can make a permanent density variation in the fiber core, resulting in a permanent modification of the refractive index profile of the core. Ion implantation has also been used to fabricate LPGs through a metal amplitude mask [90]. Hollow-core optical fiber filled with a liquid crystal solution can be periodically poled by applying a voltage to electrodes to create a LPG structure [91]. A simple method to create temporary LPG is to press a periodically grooved plate onto a fiber, and this is based on the physical deformation to the optical fiber which can also change the refractive index profile of the fiber core [92, 93]. CO_2 laser irradiation methods were developed to write LPGs using the localized rapid heating and subsequent cooling of the optical fiber, which results in the stress relief-induced refractive index changes in the fiber core.

A big problem with the UV inscription method is the LPGs fabricated by this method cannot survive at high temperature. When the temperature goes much beyond room temperature, the UV written LPG starts to fade and eventually loses the modal coupling. Among the techniques mentioned above, femtosecond laser, CO_2 laser irradiation and electric discharge are able to make survival LPG at a temperature up to 1000°C [94]. But femtosecond lasers are too expensive to be used in LPG fabrication; and CO_2 laser irradiation and electric discharge method may significantly affect the mechanical strength of the optical fibers.

Meanwhile, there are two common problems for nearly all the traditional LPG fabrication methods mentioned above. Firstly, nearly all of them produce permanent inscription to the fiber. Once the LPG is written in a fiber section, the section is designated for the LPG permanently and only. Although as mentioned before, pressing a periodically grooved plate onto a fiber can generate a temporary LPG, it also damages the mechanical properties of the fiber making the fiber more fragile and thus is not practical in LPG sensing applications. Secondly, in regards to the fiber sensing applications, they can only provide sensors for single-point measurement.

Theoretically speaking, multi-point measurement also works for LPGs. However, people prefer using FBGs with much shorter grating period because FBG sensors have better multiplexing capability and spatial resolution.

To overcome the problems of conventional LPGs, we proposed the idea of acoustically generated traveling LPG (T-LPG). In this concept, the LPG is generated by an acoustic wave, so it is temporary. When the acoustic source is off, there is no acoustic wave in the fiber and thus no LPG, making the fiber versatile for many applications. Also, T-LPG is generated by pulses of acoustic wave, and is traveling along the fiber as the acoustic pulses propagate in the fiber. So the T-LPG is detectable at different locations in the fiber, enabling the distributed measurement capability.

Using acoustic wave to generate grating originates from the acousto-optic Bragg diffraction technique, which is an interaction between two or more light waves and an acoustic wave in an optical material [95]. The acoustic wave can cause a periodic change in the refractive index by periodically straining the material. This periodic refractive index change acts like a diffraction grating, causing coupling between the light waves when the coupling condition is satisfied. The light waves can be in the same or opposite propagation directions, as long as their beatlength L_b equals to the acoustic wavelength λ_a. When two interfering light waves propagate in an optical fiber, their phase relation is restored after integer multiples of a certain propagation length, which is called beatlength defined as:

$$L_B = \frac{2\pi}{\Delta\beta} = \frac{\lambda_{res}}{\Delta n_{eff}} \tag{3-9}$$

where $\Delta\beta$ is the difference between the propagation constants of the two modes; Δn_{eff} is the difference between the effective refractive indices of the two modes at the resonance wavelength; λ_{res} is the optical resonance wavelength at which the coupling happens. The amount of light coupled in the coupling process depends on the interaction length, the acoustic amplitude, the elasto-optic properties of the fiber and the overlap between the optical and acoustic waves.

To enable coupling between two optical modes using periodic acoustic wave, the wavelength of the acoustic wave should equal the beatlength of the two modes. In the low frequency regime, the acoustic wavelength λ_a is in a relation with the acoustic frequency and the applied axial strain on the fiber as given by [96]:

$$\lambda_a = \sqrt{\frac{\pi R v_a}{f_a}\sqrt{1+\frac{\varepsilon \cdot \lambda_a{}^2}{\pi^2 R^2}}} \tag{3-10}$$

where v_a = 5760m/s is the acoustic velocity of extensional waves in silica; f_a is the acoustic frequency; R is the fiber radius; ε is the axial strain. When an axial strain is applied to the acoustic-optic interaction region, both the acoustic wavelength and the optical beatlength change. So the local acoustic wavelength may change depending on different local strain, resulting in a small shift of the local LPG resonance wavelength. A small strain ε changes the acoustic wavelength by $\Delta\lambda_a$ as[97]:

$$\frac{\Delta\lambda_a}{\lambda_a} = \frac{v_a}{4\pi R f_a}\varepsilon \tag{3-11}$$

In our case, we can minimize the strain effect in the experimental setup, so we can assume ε is so small that we can ignore it for simplicity. Therefore, the acoustic wavelength in our case can be expressed as:

$$\lambda_a = \sqrt{\frac{\pi R v_a}{f_a}} \tag{3-12}$$

Figure 3.4 plots the relations of the acoustic wavelength with the acoustic frequency ranging from 1MHz to 5MHz.

We can also have the effective acoustic velocity of acoustic extensional wave in optical fiber as:

$$v_{a\_eff} = \lambda_a \cdot f_a = \sqrt{\pi R v_a f_a} \tag{3-13}$$

To have the modal coupling, we need to have:

$$\lambda_a = L_B \tag{3-14}$$

Based on the phase matching condition as given by Equation (3-1) for traditional LPG, we can have the phase matching condition for gratings generated by acoustic waves in an optical fiber as:

$$\lambda_{res} = \lambda_a \cdot \Delta n_{eff} = \sqrt{\frac{\pi R v_a}{f_a}} \cdot (n_{core} - n_{cl}^i) \tag{3-15}$$

where n_{core} and n^i_{cl} are the effective indices of the core mode and the ith cladding mode.

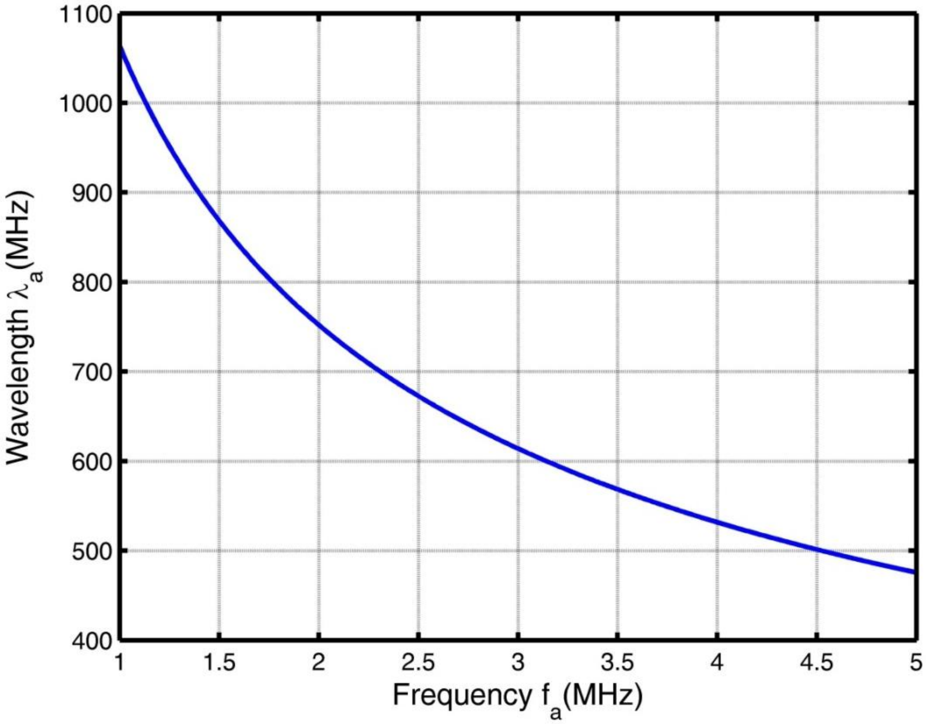

Figure 3.4. Acoustic wavelength as a function of the applied acoustic frequency.

An acousto-optic device can be used as an optical switch by simply turning the acoustic wave on and off, and as a frequency shifter because the refractive index modulation travels along with the acoustic wave and thus gives the coupled light a Doppler shift [95]. It can also be used as a tunable optical filter because the coupling is weakened and eventually falls to zero at deviating wavelengths far from the resonance.

3.3 Traveling LPG (T-LPG)

Generally speaking, fiber-compatible acousto-optic devices require appropriate means to excite and couple acoustic waves into the optical fiber, and there have been theoretical and experimental investigations in this field. However, the scope of research has been confined within applications for optical communications, such as tunable filters [98], and it has never been used for sensing until our report [78]. In the previous work for tunable filters, continuous acoustic waves were used to generate a standing LPG; while in our work, acoustic pulses are used to generate a transient and also traveling LPG. This acoustically generated traveling LPG (T-LPG) can propagate along the fiber as the acoustic pulse travels in the fiber, and its length is defined by the spatial span of the acoustic pulse. Moreover, because the T-LPG is traveling along the fiber with the propagation of the acoustic pulses, the meaurand field can be continuously monitored along the fiber. The LPG spatial location information can be known by the timing of the acoustic pulse relative to the optical measurement. By tuning this differential timing, any point along the fiber can be addressed to enable fully-distributed measurement.

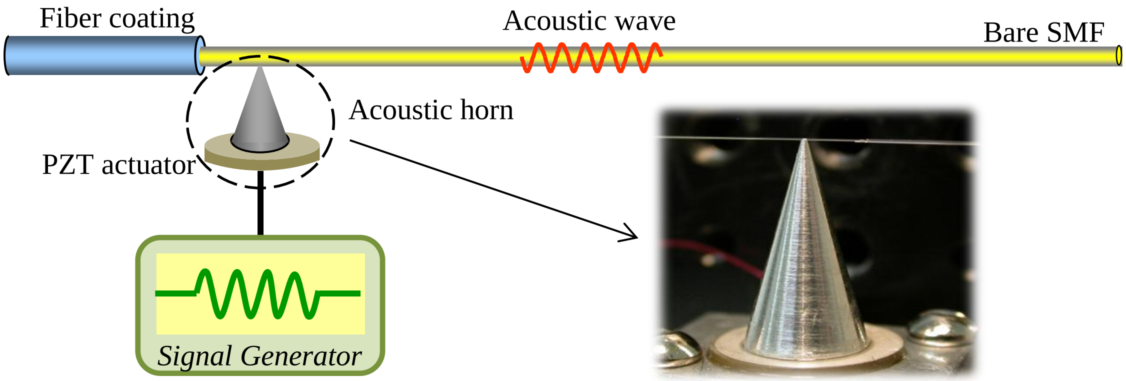

Figure 3.5. Operation principle of acoustically generated T-LPG.

Figure 3.5 illustrates the schematic of the T-LPG excitation and coupling setup. A pulsed acoustic wave is generated by a piezoelectric transducer (PZT), magnified by a cone-shaped aluminum horn and delivered to a segment of a single-mode fiber. This kind of acoustic horn has been investigated extensively in the literature[99]. The acoustic horn transforms low amplitude oscillations into high amplitudes by changing the cross section of the horn. The acoustic frequency is chosen to promote effective optical coupling from the core mode to a number of cladding modes for an interested optical spectral range. In the experiment, acoustic frequencies ranging from 1MHz to 4MHz were tested, and their corresponding LPG resonance wavelengths fall into the range from 1520nm to 1570nm. The key issue is how to appropriately bond the fiber with the horn to have a firm connection as well as an effective acoustic coupling. UV cured optical adhesive was used to glue the bare fiber to the aluminum horn. The adhesive is designed for optical bonding with excellent clarity, low shrinkage and light flexibility providing good light injection and transmission properties. It is cured when exposed to ultraviolet light for several minutes. However, the amount of the UV adhesive should be controlled to minimum to optimize the acoustic coupling from the horn to the fiber because the larger amount of adhesive would have a significant damping effect on the acoustic wave. The polymer coating of the single-mode fiber (SMF) on the sensing side is removed to reduce the acoustic loss, and the coating on the other side is kept as an acoustic damper. The strength and coupling wavelengths of the LPG can be easily tuned by adjusting the magnitude, frequency and number of periods of the acoustic wave, which makes the LPG characteristics more flexible to control.

In the experiment, firstly we need to choose proper acoustic frequencies to work with. According to the phase matching condition given by Equation (3-11), the acoustic frequency can be expressed as:

$$f_a = \pi R v_a \cdot \left(\frac{n_{core} - n_{cl}^{i}}{\lambda_{res}} \right)^2 \tag{3-16}$$

From the above equation we can see that to generate LPG at the same wavelength (the same λ_{res}), high order cladding modes (lower n^{i}_{cl}) correspond to higher acoustic frequencies. Generally speaking, to make the LPG more sensitive to the surrounding medium, higher order cladding modes are preferred because they have more evanescent fields extending to the outside of the fiber. However, the acoustic frequency is also limited by the resonance frequency of available PZTs as well as the wavelength range of the measurement equipment. Therefore, it is always necessary to test the acoustic frequency for LPG using continuous acoustic wave. This can give the appropriate acoustic frequency and the wavelength scanning range needed in the traveling LPG spectrum measurement.

Figure 3.6 is the schematic of the experimental setup of the standing LPG spectrum measurement. There is a scanning laser source and a photodetector in the optical component testing system (CTS, Micron Optics si720), which is used to measure the transmission spectrum from 1520nm to 1570nm. The signal generator (Agilent, 33120A) outputs sinusoidal waveform, whose amplitude is amplified to $30V_{p\text{-}p}$ by a power amplifier (Electronics & Innovation, 403LA). In the test, the frequency of the waveform was continuously tuned around the PZT's central frequency, and at each frequency, the corresponding transmission spectrum was monitored from the CTS. PZT discs (from Steminc, Inc) with thickness mode vibration were used to generate acoustic waves in the transverse mode. For PZT with 2.2MHz resonance frequency, when the PZT's frequency was tuned from ~1.5MHz to ~3MHz, its generated acoustic LPG was continuously observed within the 1520-1570nm range but with different grating strength (notch depth). In later experiment, PZT with different resonance frequencies were also tested. It was found that in our acoustic excitation setup, the requirement of the PZT's frequency is not very strict, and the frequency can be any value between 1MHz to 5MHz, corresponding to different cladding modes.

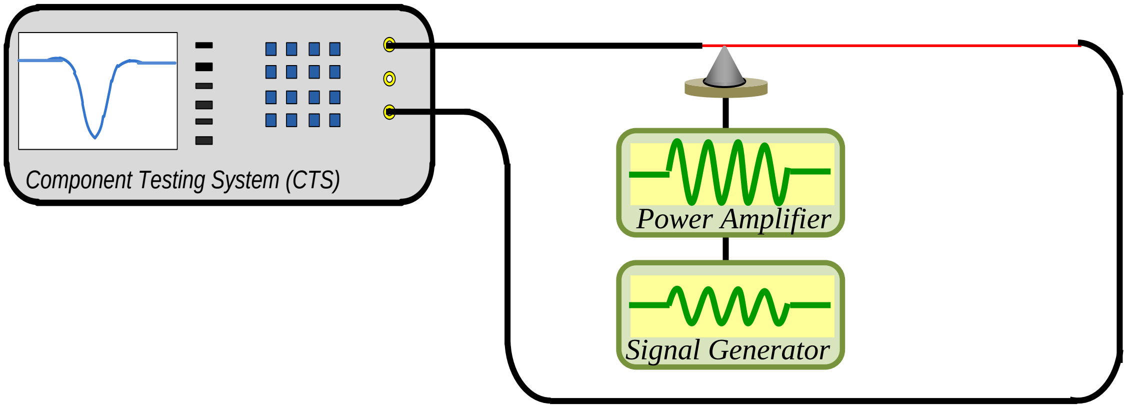

Figure 3.6. Schematic of acoustic LPG spectrum measurement setup.

Because continuous acoustic wave was used in this test, the generated grating length was determined by the length of the bare fiber used in the test. Regular single-mode fiber (Corning, SMF-28) has Acrylate coating outside the cladding to protect the fiber. But Acrylate has high acoustic attenuation, and based on our experience, acoustic wave cannot propagate longer than several centimeters in the fiber with the coating. So we need to strip off the Acrylate coating. An easy way to do so is to immerse the fiber into Acetone for a while, and the coating is detached from the fiber automatically. To de-coat fiber of several meters, usually around 1 hour immersion time is enough. Since Acetone evaporates easily, a covered container is needed with the fiber coiled into loops in it. This de-coating method can quickly strip off the coating for a long fiber section (up to tens of meters) without damage to the fiber surface.

Figure 3.7 shows typical transmission spectra of T-LPG generated by different acoustic frequencies, from which we can see that for a given fiber, the grating resonance wavelength can be tuned by changing the acoustic frequency. Different resonance wavelengths correspond to different cladding modes with different coupling coefficients resulting in different grating strength (notch depth in the spectrum). The side lobes are introduced by nearby cladding modes. The purpose of this test using continuous acoustic wave is to choose a proper acoustic frequency based on its corresponding LPG spectrum, which will be used in later experiment to generate transient LPG. There are two main factors that are considered to choose the acoustic frequency. One is the strength of the generated grating, and stronger gratings are preferred to have better signal to noise ratio (SNR). The other is the wavelength of the generated grating. In later experiment, a tunable laser was used as the light source whose wavelength tuning range is 1510 nm – 1580nm, so the preferred LPG resonance wavelength is in the center region of this range in order to have the full spectrum of the grating, especially when the grating is broadened by shorter acoustic pulses or shifted by the measurands for a sensing application.

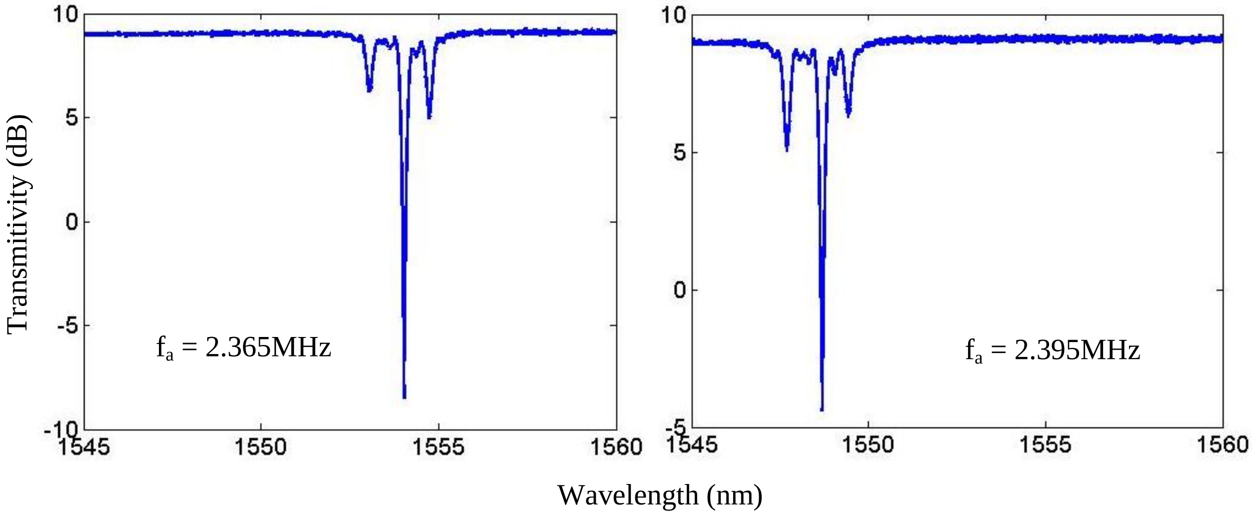

Figure 3.7. Transmission spectra of T-LPG at different acoustic frequencies.

Once the acoustic frequency is chosen using continuous acoustic wave as described in the above test, the signal generator is fixed at that frequency, and an acoustic pulse is used to generate a traveling LPG. To generate acoustic pulses, the signal generator is operated in burst mode, and each burst corresponds to one LPG. There are four parameters that need to be set in the burst mode. One is the waveform, which is set to sinusoidal in our experiment. The second is the frequency of the waveform, which should be the value selected by the previous test. The third one is the burst rate. It is the frequency of the burst, and is determined by the length of the sensing fiber. To avoid confusion, we need to make sure that there is one LPG at most propagating in the fiber at any data acquisition time. For example, according to Equation (3-12), the effective acoustic velocity for applied frequency f_a = 3.5MHz is about 2000m/s. So the propagation time for a 10cm LPG generated by this frequency in 1m sensing fiber is about 0.6ms, corresponding to 1.7kHz burst rate. Lower burst rate should be chosen for a longer sensing fiber length. The forth parameter is the number of cycles in each burst. It is the number of grating periods, and also determines the spatial resolution in the distributed sensing. A larger cycle number corresponds to a longer spatial resolution, but also a narrower grating linewidth and thus a higher sensitivity. Therefore, there is a trade-off between the spatial resolution and the sensitivity.

Figure 3.8 shows the transmission spectra for different grating lengths or different cycle numbers (CN) for a given acoustic frequency in each burst. From the spectra we can see that the grating's strength increases and its linewidth decreases with the increase of the cycle numbers. However, 400 cycles in each burst means the grating length is about 30cm for 2.365MHz acoustic frequency, making the spatial resolution not so good for sensing span of several meters.

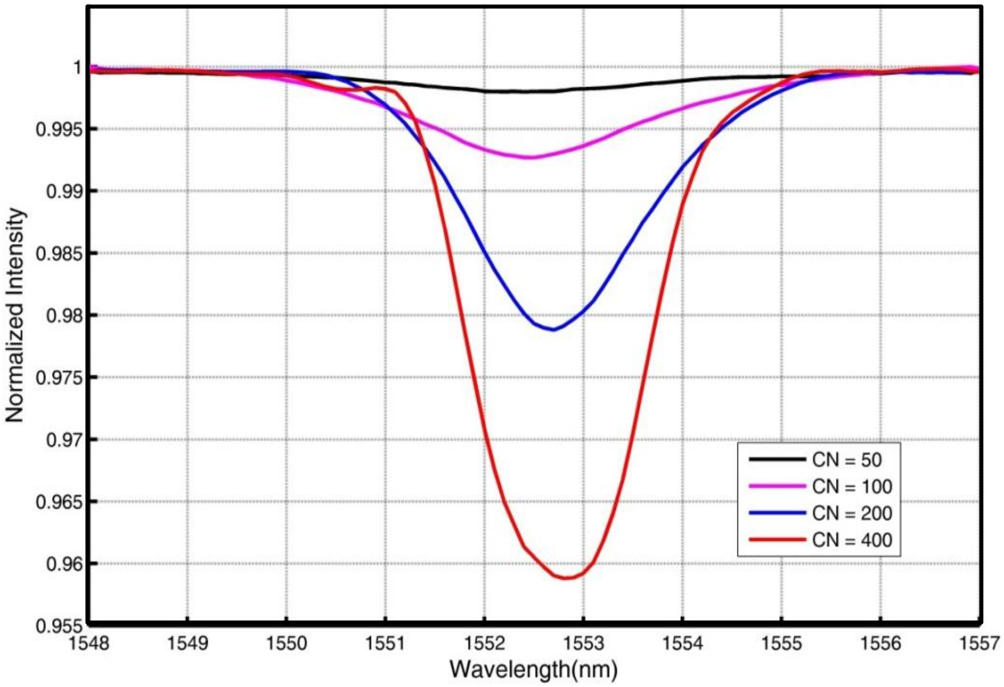

Figure 3.8. Transmission spectra of T-LPG of different lengths.

The experiment setup to measure the traveling LPG's spectrum is schematically shown in Figure 3.9. The acoustic frequency was set as 3.745MHz, and the generated LPG has 550 μm period and with resonance wavelength at ~1547nm. The signal generator was operated in burst mode with 200-cycle sinusoidal waves in each burst, corresponding to about 11cm LPG length. The total length of the sensing fiber is 2.5m, so the burst rate was set as 500Hz to make sure that at any time there is only one LPG at most propagating in the fiber. The voltage applied on the acoustic horn was about $40V_{p\text{-}p}$. A tunable laser (New Focus 6328) was used as the optical source, whose wavelength was scanned from 1540nm to 1552nm at a step size of 0.1nm. At each wavelength, the change of the light intensity output from the fiber end as a function of the acoustic wave traveling time was recorded by an oscilloscope (LeCroy LT322). The acoustic wave traveling time was mapped to the fiber location by perturbing the fiber at specific locations and observing the signal variations from the oscilloscope. After scanning the wavelengths, the LPG transmission spectrum at a specific location of the fiber was reconstructed from the intensities recorded by the oscilloscope.

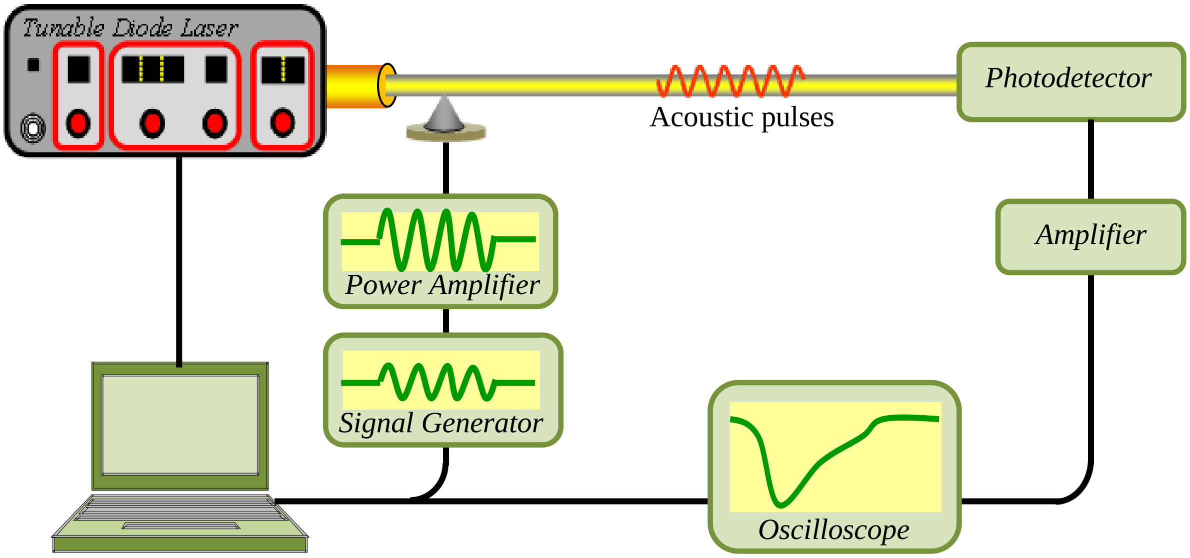

Figure 3.9. Schematic of T-LPG spectrum measurement setup.

Figure 3.10 shows the experimental results. Figure 3.10 (a) is the data collected by the oscilloscope when the tunable laser output was 1547nm. At each tunable laser output wavelength in the LPG spectrum range, the signal seen from the oscilloscope was similar as this, indicating the intensity of the LPG when it was traveling along the fiber. Because LPG couples light from the core mode to cladding modes, the transmitted light intensity is decreased when there is LPG in the fiber. So we can see from the figure that the light received at the photodetector started to decrease when the LPG started to enter the fiber at about t = 0.1ms. And after that, the LPG intensity was increasing as the LPG entered into the fiber gradually because the number of grating periods in the fiber was increasing. During this time, the received light was decreasing until the entire LPG had entered into the fiber, corresponding to the time of the dip in the figure. At this time, the T-LPG had fully entered into the fiber after traveling in the fiber for the distance that equals the LPG length. After the dip, the grating got weaker and weaker as it was traveling along the acoustically lossy fiber. So the received transmitted light intensity was increasing until the grating was totally damped by the fiber coating at the end of the fiber.

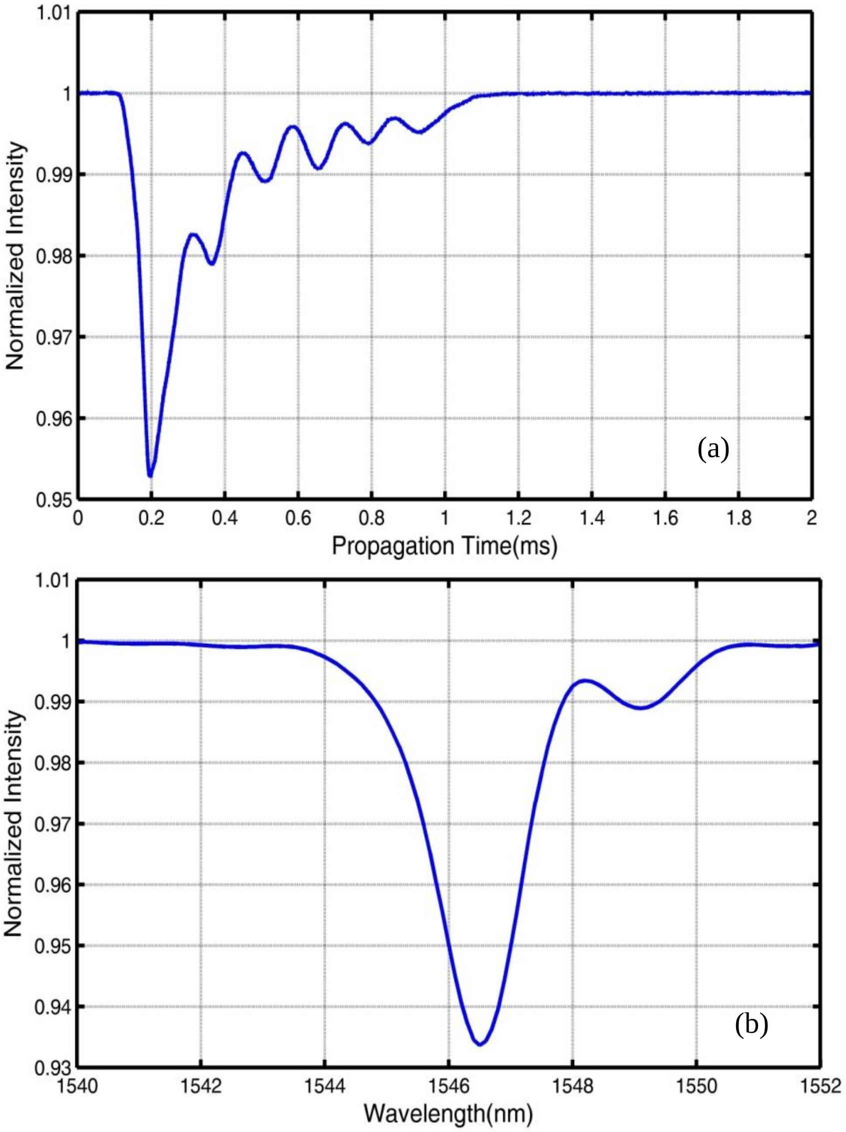

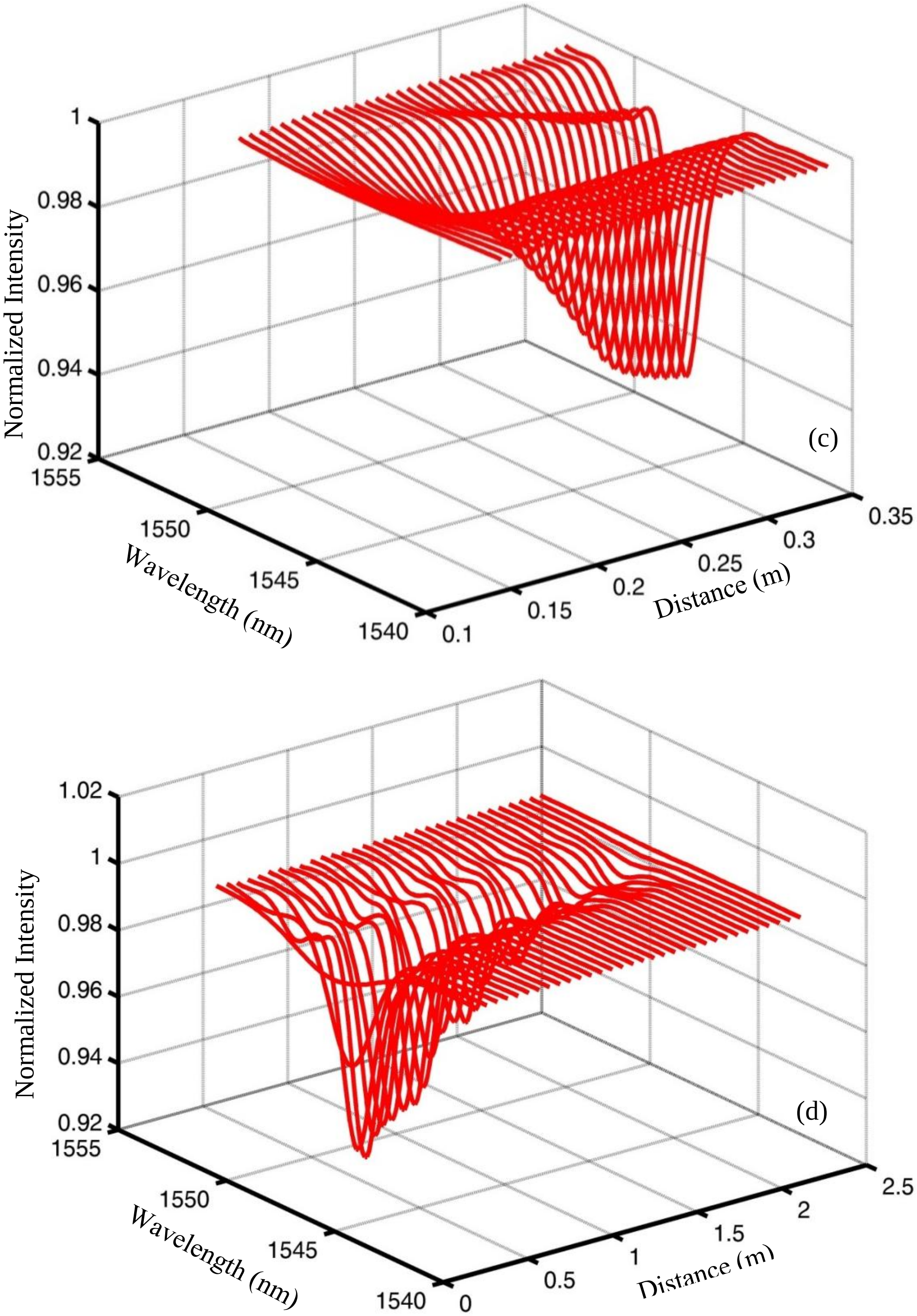

Figure 3.10. Experimental results: (a) Oscilloscope data at 1574nm wavelength of tunable laser output; (b) transmission spectrum of the T-LPG at t = 0.12ms propagation time; T-LPG spectral evolution as the LPG was (c) entering the fiber and (d) traveling along the fiber.

Figure 3.10 (b) is the transmission spectrum of the T-LPG measured at t = 0.22ms at which the entire grating has fully entered the fiber. Figure 3.10(c) plots the LPG transmission spectra at different locations from the sensing fiber starting point to the position corresponding to propagation time t = 0.22ms. It shows how the LPG transmission spectrum changes as the acoustic cycles sequentially enter into the fiber. Figure 3.10(d) plots the LPG transmission spectra at different locations in the whole sensing span, and it shows how the LPG transmission spectrum changed as the grating travels along the fiber.

The LPG spectra in the experimental results show that the acoustically generated LPG is weak, e.g. the spectral density at the LPG resonance wavelength was only 10% lower than the shoulders at distance of 0.6m. This is due to the weak acoustic wave coupled into the fiber, which can be enhanced by using a higher power signal generator or by using a more efficient acoustic coupling setup. It is also seen that acoustic wave attenuates rapidly when it propagates down the fiber, which would limit the measurement range. We believe this can be improved by exciting other acoustic modes, e.g. longitudinal modes or torsional modes which have smaller attenuation in the fiber, or by using specially designed fibers to better confine the acoustic wave. The fiber length used in the experiment was 2.5m, which could be substantially increased by generating stronger LPG through higher power of acoustic wave.

3.4 T-LPG transmission spectrum simulation

3.4.1 Transmission function

In our case, the acoustic wave is the fundamental flexural wave, and the optical mode coupling is between the core mode and any asymmetric cladding mode which is the second-order cladding modes in the frequency range used. The discussion below is based on coupled mode theory and previous theoretical investigation of acousto-optic coupling of fiber modes over the years [97-100]. According to the theory of gratings, the transmission of the generated T-LPG can be expressed as [100]:

$$T(\lambda) = 1 - \frac{\kappa^2}{\kappa^2 + \delta^2} \sin^2 (L\sqrt{\kappa^2 + \delta^2}) \tag{3-17}$$

where κ is the acoustic wave coupling coefficient determined by the acoustic amplitude. It describes the overlap between the index perturbation and the optical mode field over the fiber cross section. L is the grating length. δ is the phase mismatch coefficient that is zero on the resonance wavelength. It is given by [97]:

$$\delta(\lambda) = \pi\left(\frac{1}{L_b(\lambda)} - \frac{1}{\lambda_a}\right) \tag{3-18}$$

where λ_a is the acoustic wavelength determined by the acoustic frequency as given in Equation (3-12), and L_b is the beatlength of the two optical modes involved in the optical coupling, given by Equation (3-9). Therefore, by substituting these two equations into Equation (3-18) we can have the phase mismatch coefficient as:

$$\delta(\lambda) = \frac{\pi \Delta n_{eff}}{\lambda} - \sqrt{\frac{\pi f_a}{R v_a}} \tag{3-19}$$

where Δn_{eff} is the effective refractive index difference between the core mode and the cladding mode; f_a is the acoustic frequency applied on the PZT; R is the fiber radius; and v_a is the acoustic velocity in silica.

3.4.2 Effective refractive index calculation

To calculate Δn_{eff}, we need to analyze the field distribution of the core and cladding modes. The following discussion of this is based on the class notes of ‘Photonic Devices and Systems, ECE6154’ instructed by Dr. Ahmad Safaai-Jazi in Bradley Department of Electrical and Computer Engineering at Virginia Tech.

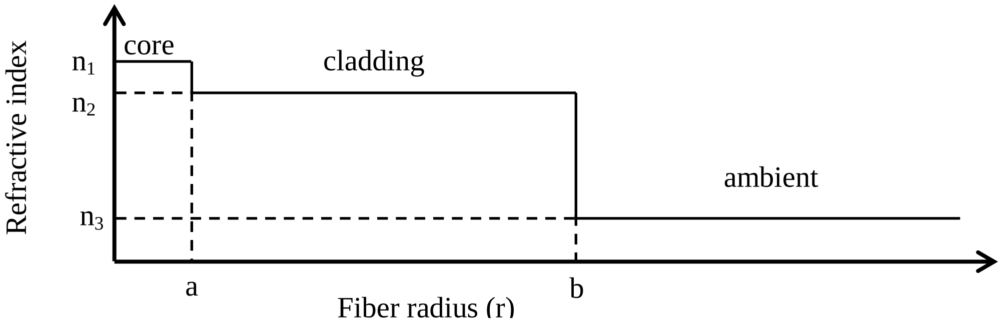

Figure 3.11. Schematic of refractive index profile of single mode fiber.

The refractive index profile of a step-index single-mode fiber is illustrated in Figure 3.11, and for illustrative purpose, the size of the fiber core relative to the fiber cladding is greatly exaggerated in the figure.

n_1 and n_2 are the refractive indices of the fiber core and cladding respectively; n_3 is the refractive index of the layer outside the cladding, and r is the radius of the fiber. Regular single-mode fiber (SMF-28, Corning) has germanium-doped silica and pure silica as the core and cladding material, respectively. So n_1 and n_2 are dependent on the dopant as well as the wavelength. In the simulation, n_1 and n_2 are calculated from the Sellmeier's equation given as[101]:

$$n_i = \sqrt{1 + \sum_{j=1}^{3} \frac{A_{ij}\lambda^2}{\lambda^2 - \lambda_{ij}^2}}, i = 1,2 \tag{3-20}$$

where A_{ij} and λ_{ij} are material constants. For regular single-mode fiber, the core material (n_2) is germanium-doped glass and the cladding material (n_2) is pure fused silica. In the simulation, we choose 3.5 mol % GeO_2-doped silica as the core material and pure silica as the cladding material Their Sellmeier constants are given as [102]:

Table 3.1. Sellmeier constants

	A_{i1}	A_{i2}	A_{i3}	λ_{i1}(μm)	λ_{i2}(μm)	λ_{i3}(μm)
n_1	0.7042038	0.4160032	0.9074049	0.0514415	0.1291600	9.896156
n_2	0.696750	0.408218	0.890815	0.069066	0.115662	9.900559

Figure 3.12 shows the calculated n_1 and n_2 using the Sellmeier's equation. The normalized refractive index difference is about 0.35%, which is similar to the value 0.36% provided by the datasheet of SMF-28 (Corning). In our simulation, the outer cladding layer is air, so $n_3 =1$.

Figure 3.13 schematically shows the cross-section of an optical fiber. As previously mentioned, scalar modes LP_{mn} are used to describe the modes in weakly guided single-mode fiber. The core mode is the fundamental mode, expressed as LP_{01} mode. In solving LP_{01} core mode, we assume the cladding region is infinitely extended. Because the guided core modes have exponentially decaying fields outside the core, and if the cladding radius is large enough which is the case in practice, the field of the guided modes at the outer boundary of the cladding can be ignored. So the mode field of the core mode is nearly isolated from the outer cladding layer ambient, the refractive index profile is simplified to a double-layer structure without consideration of the ambient layer in solving the effective index of the LP_{01} mode.

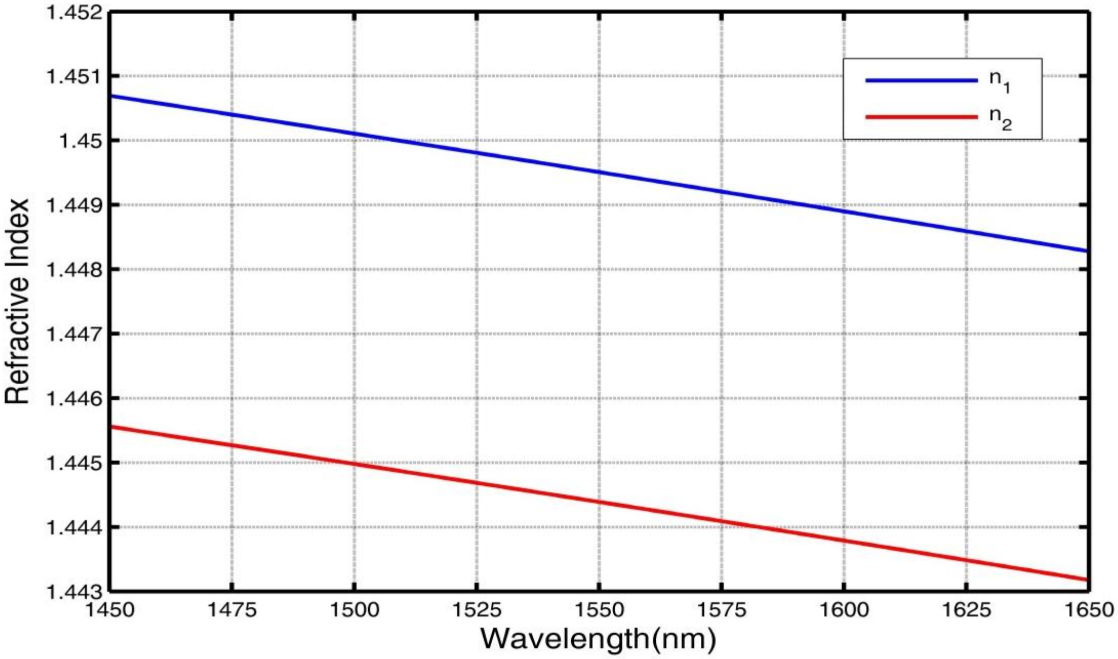

Figure 3.12. Calculated refractive index for core (n1) and cladding (n2).

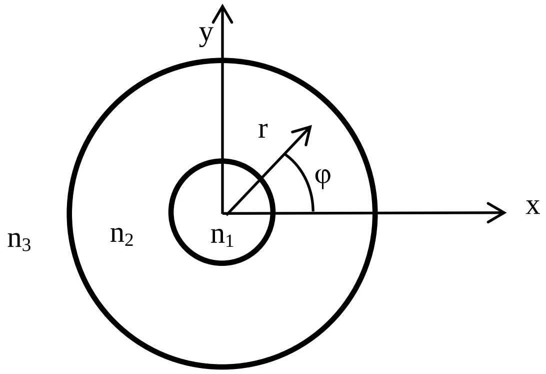

Figure 3.13. Schematic of cross-section of a round optical fiber.

The mode field of LP_{01} core mode can be written as [103]:

$$\Psi(r) = \begin{cases} A_1 J_0(q_1 r)\cos\phi, & r < a, 0 < \phi \le 2\pi \\ A_2 K_0(q_2 r)\cos\phi, & r > a, 0 < \phi \le 2\pi \end{cases} \tag{3-21}$$

where ψ represents either E_x or E_y; ϕ is the azimuthal angle as described in the model in Figure 3.13; J_0 is the first kind Bessel function and K_0 is the second kind modified Bessel function. A_1 and A_2 are constant coefficients to describe the field amplitude. q_1 and q_2 are given by:

$$\begin{cases} q_1 = k_0\sqrt{n_1^2 - n_{core}^2} \\ q_2 = k_0\sqrt{n_{core}^2 - n_2^2} \end{cases} \tag{3-22}$$

where $k_0 = 2\pi/\lambda$ is the free space wavenumber, and n_{core} is the effective refractive index of the core mode. The boundary condition of Equation (3-21) is that both $\psi(r)$ and $d\psi(r)/dr$ are continuous at $r = a$. $d\psi(r)/dr$ is given by:

$$\frac{d\Psi(r)}{dr} = \begin{cases} A_1 q_1 J_0^{'}(q_1 r)\cos\phi, & r < a \\ A_2 q_2 K_0^{'}(q_2 r)\cos\phi, & r > a \end{cases} \tag{3-23}$$

and for Bessel functions we have:

$$\begin{cases} J_l^{'}(x) = \frac{l}{x} J_l(x) - J_{l+1}(x) \\ K_l^{'}(x) = \frac{l}{x} K_l(x) - K_{l+1}(x) \end{cases} \tag{3-24}$$

so we can obtain the following equation after applying boundary conditions to Equation (3-21) and Equation (3-23):

$$\frac{J_0(q_1 a)}{q_1 J_1(q_1 a)} = \frac{K_0(q_2 a)}{q_2 K_1(q_2 a)} \tag{3-25}$$

This is the characteristic equation for LP_{01} core mode, which can be numerically solved for n_{core}. The following values are used in the calculation based on the data sheet of SMF-28: a = 4.1 µm, b = 62.5 µm. So the calculated effective refractive index of the LP_{01} core mode is plotted in Figure 3.14.

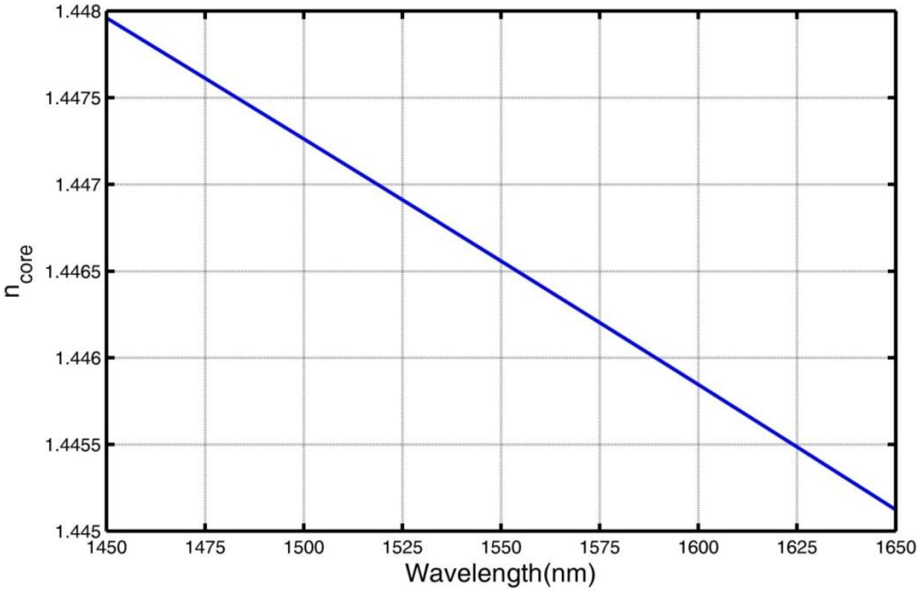

Figure 3.14. Calculated effective refractive index of LP_{01} core mode.

It is demonstrated that the acoustic-optic coefficient is only non-zero for modes differed by an integer in angular momentum, so there is no coupling between the LP_{mn} and $LP_{m'n'}$ modes unless m' = m+k' where k is an odd integer [99]. Therefore, the core LP_{01} mode will be coupled to second order cladding modes LP_{1n}. To solve the effective refractive index of the cladding modes, similarly we need to write down the mode field. But differently, we need to consider the outer cladding ambient layer. So the mode field of the second order cladding modes can be written as[103]:

$$\Psi(r) = \begin{cases} A_1 J_1(q_1 r)\begin{pmatrix}\sin\phi \\ \cos\phi\end{pmatrix}, & r < a, 0 < \phi \le 2\pi \\ \left[A_2 J_1(q_2 r) + A_3 Y_1(q_2 r)\right]\begin{pmatrix}\sin\phi \\ \cos\phi\end{pmatrix}, & a < r < b, 0 < \phi \le 2\pi \\ A_4 K_1(q_3 r)\begin{pmatrix}\sin\phi \\ \cos\phi\end{pmatrix}, & r > b, 0 < \phi \le 2\pi \end{cases} \tag{3-26}$$

where J_1 and Y_1 are the first and second kind Bessel functions, respectively; K_2 is the second kind modified Bessel function. A_1, A_2, A_3, A_4 are constant coefficients to describe the field amplitude. q_1, q_2 and q_3 are given by:

$$\begin{cases} q_1 = k_0\sqrt{n_1^2 - n_{clad}^2} \\ q_2 = k_0\sqrt{n_2^2 - n_{clad}^2} \\ q_3 = k_0\sqrt{n_{clad}^2 - n_3^2} \end{cases} \tag{3-27}$$

So $d\psi(r)/dr$ is expressed as:

$$\frac{d\Psi(r)}{dr} = \begin{cases} A_1 q_1 J_1^{'}(q_1 r)\begin{pmatrix}\sin\phi \\ \cos\phi\end{pmatrix}, r < a \\ A_2 q_2 J_1^{'}(q_2 r) + A_3 q_2 Y_1^{'}(q_2 r)\begin{pmatrix}\sin\phi \\ \cos\phi\end{pmatrix}, a < r < b \\ A_4 q_3 K_1^{'}(q_3 r)\begin{pmatrix}\sin\phi \\ \cos\phi\end{pmatrix}, r > b \end{cases} \tag{3-28}$$

The boundary condition is that both $\psi(r)$ and $d\psi(r)/dr$ are continuous at r = a, and r =b. Therefore, we can have the following equations:

$$A_1 J_1(q_1 a) = A_2 J_1(q_2 a) + A_3 Y_1(q_2 a) \tag{3-29}$$

$$A_1 q_1 J_1^{'}(q_1 a) = A_2 q_2 J_1^{'}(q_2 a) + A_3 q_2 Y_1^{'}(q_2 a) \tag{3-30}$$

$$A_4 K_1(q_3 b) = A_2 J_1(q_2 b) + A_3 Y_1(q_2 b) \tag{3-31}$$

$$A_4 q_3 K_1(q_3 b) = A_2 q_2 J_1^{'}(q_2 b) + A_3 q_2 Y^{'}{}_1(q_2 b) \tag{3-32}$$

From Equation (3-31) and (3-32) we can get the relationship between A_2 and A_3 as:

$$A_5 = \frac{A_2}{A_3} = \frac{q_3 K_1^{'}(q_3 b) Y_1(q_2 b) - q_2 K_1(q_3 b) Y_1^{'}(q_2 b)}{q_2 K_1(q_3 b) J_1^{'}(q_2 b) - q_3 K_1^{'}(q_3 b) J_1(q_2 b)} \tag{3-33}$$

Substituting Equation (3-33) into Equations (3-29) and (3-30), and based on Equation (3-24), we can have the characteristic equation for the LP_{1n} cladding modes as:

$$\frac{J_1(q_1a)}{q_1J_0(q_1a)-\frac{1}{a}J_1(q_1a)}=\frac{A_5J_1(q_2a)+Y_1(q_2a)}{A_5\left(q_2J_0(q_2a)-\frac{1}{a}J_1(q_2a)\right)+q_2Y_0(q_2a)-\frac{1}{a}Y_1(q_2a)} \tag{3-34}$$

There are many cladding modes in the fiber, but it is found in our acoustic frequency range from 2MHz to 4MHz, the acousto-optic coupling is mainly efficient to the first three LP_{1n} cladding modes: LP_{11}, LP_{12} and LP_{13}. So we only numerically solve the above equation for these three cladding modes. Figure 3.15 plots the calculation results of the effective refractive indices of these three modes.

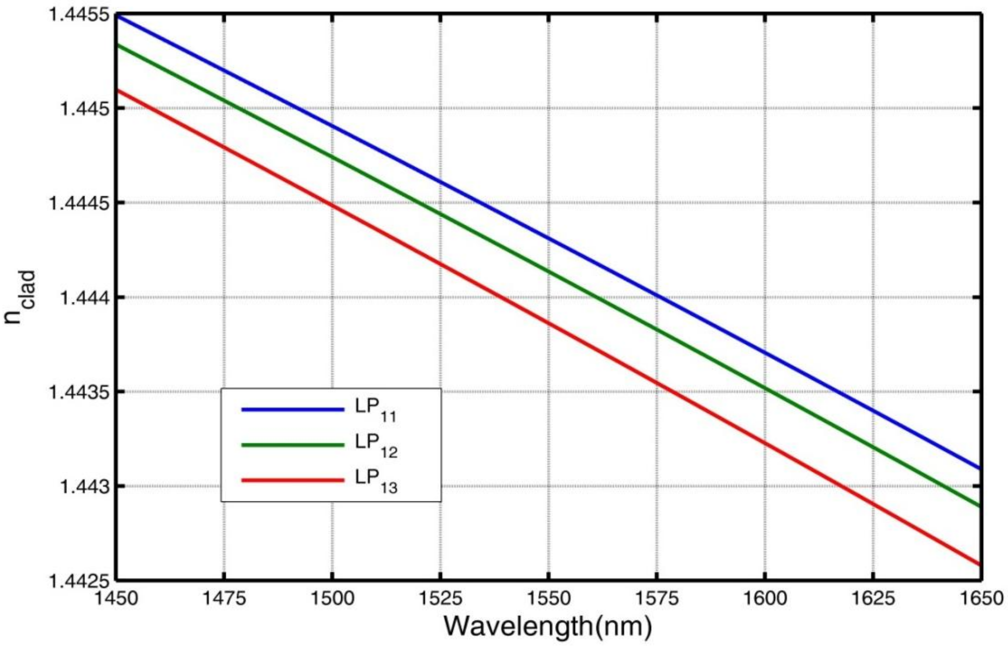

Figure 3.15. Calculated effective refractive index of cladding modes: LP_{11}, LP_{12}, LP_{13}.

Then based on Equation (3-9), we can calculate the beatlength $L_b(\lambda)$ of these three modes with the core mode LP_{01} as shown in Figure 3.16. Therefore, for a given acoustic frequency, we can simulate the transmission spectrum of the T-LPG generated by this acoustic frequency according to Equation (3-17). The acoustic wave coupling coefficient κ is different for different cladding modes, and also determined by the amplitude of the acoustic wave. For the same acoustic amplitude, among the three cladding modes of our interest, LP_{13} cladding mode has the largest value [99].

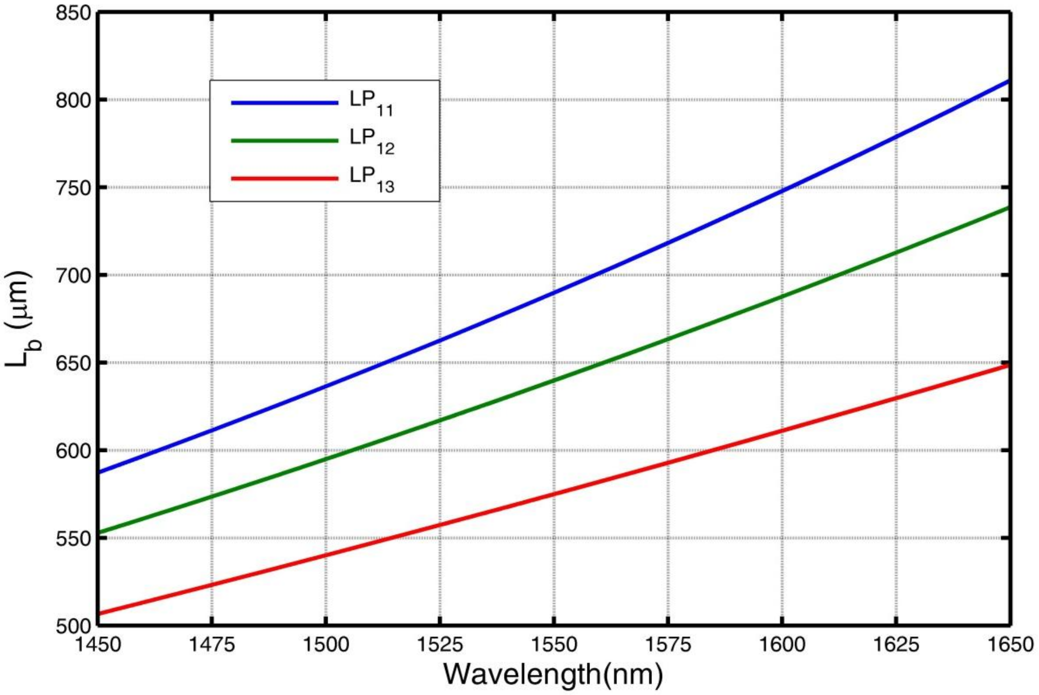

Figure 3.16. Simulated beatlength as a function of the wavelength for the LP_{01} core mode and cladding modes: LP_{11}, LP_{12}, LP_{13}.

If we set its coupling coefficient to 1, the other two coupling coefficients are relatively calculated as: 0.4 for the LP_{11} mode and 0.8 for the LP_{13} mode [104]. In the simulation, we assume: the T-LPG grating length L = 10cm and the acoustic frequency f_a = 2.395MHz. And the simulation results of the T-LPG transmission spectrum for the above cladding modes are plotted in Figure 3.17(a). From the simulation results we can see that only LP_{11} and LP_{12} cladding modes have transmission spectra within the wavelength range from 1450nm to 1700nm. In order to compare the simulation results with the measured results in Figure 3.7, we set the acoustic frequency f_a = 2.365MHz and 2.395MHz, respectively; and the grating length L = 1m.

From Figure 3.17(a) we can see that for these two acoustic frequencies, LP_{11} cladding mode is the mode that can generated T-LPG with resonance wavelength around 1550nm. So we plot the T-LPG transmission spectrum simulation for LP_{11} cladding mode in Figure 3.17(b). In the comparison with the measured results, the resonance wavelength is of our interest. For both these two acoustic frequencies, the simulated T-LPG resonance wavelength is about 2nm smaller than the measured results. A possible reason is strain applied on the fiber affected the acoustic wavelength, resulting in a slight shift of the LPG resonance wavelength. Because according to Equation (3-19), the acoustic wavelength λ_a becomes larger when an axial strain is applied on the fiber, and thus shifts the resonance to a longer wavelength.

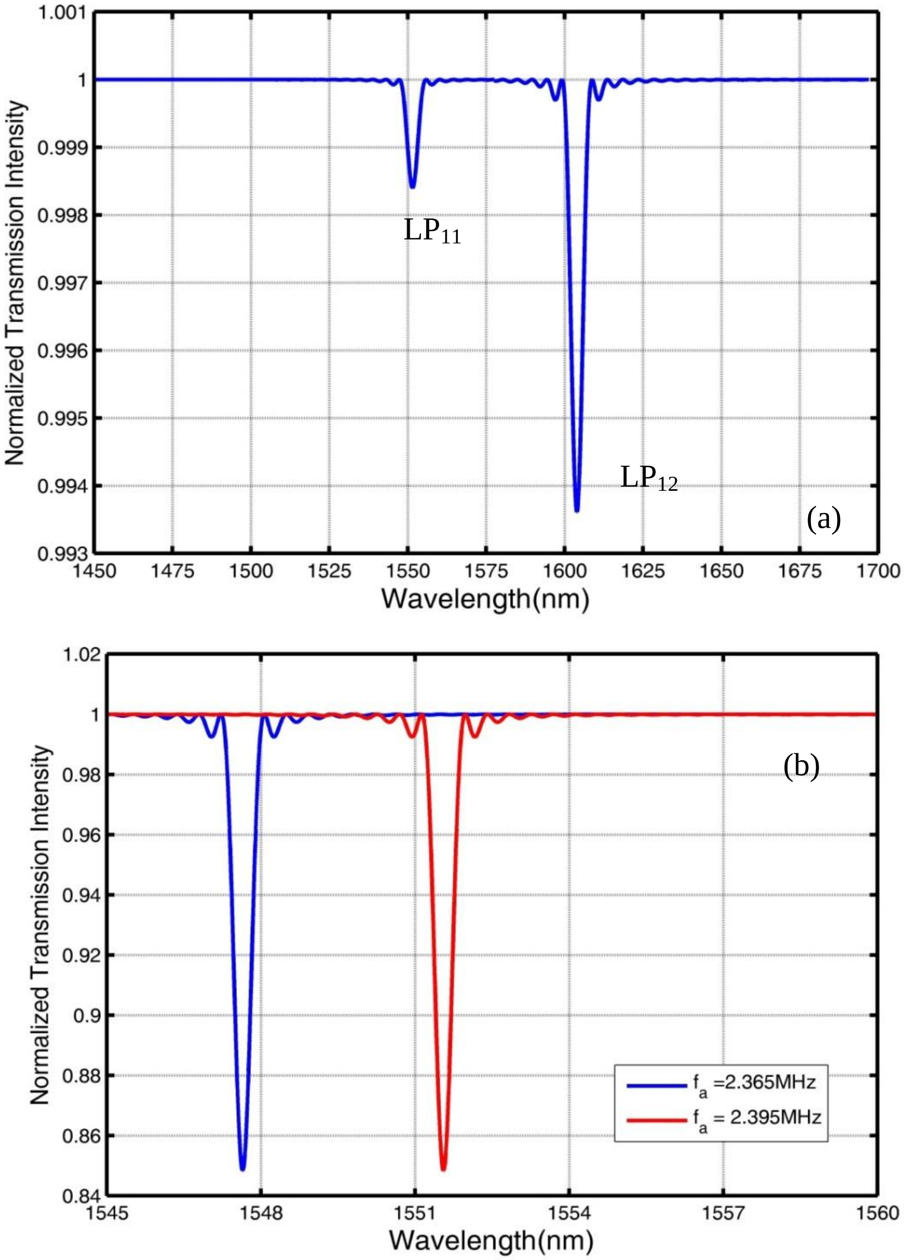

Figure 3.17. T-LPG transmission spectrum simulation for: (a) different cladding modes at the same acoustic frequency; and (b) different acoustic frequencies for the same cladding mode.

Figure 3.18 plots the simulation results of transmission spectra for different grating lengths, corresponding to different CNs in each burst. The acoustic frequency was 2.365MHz, and the cladding mode was chosen to LP_{11} to match the T-LPG resonance wavelength in the range of the measured results, as previously shown in Figure 3.8. From the comparison with the measured results, we can see that the simulation results well agree with the measured results in the change of the grating strength.

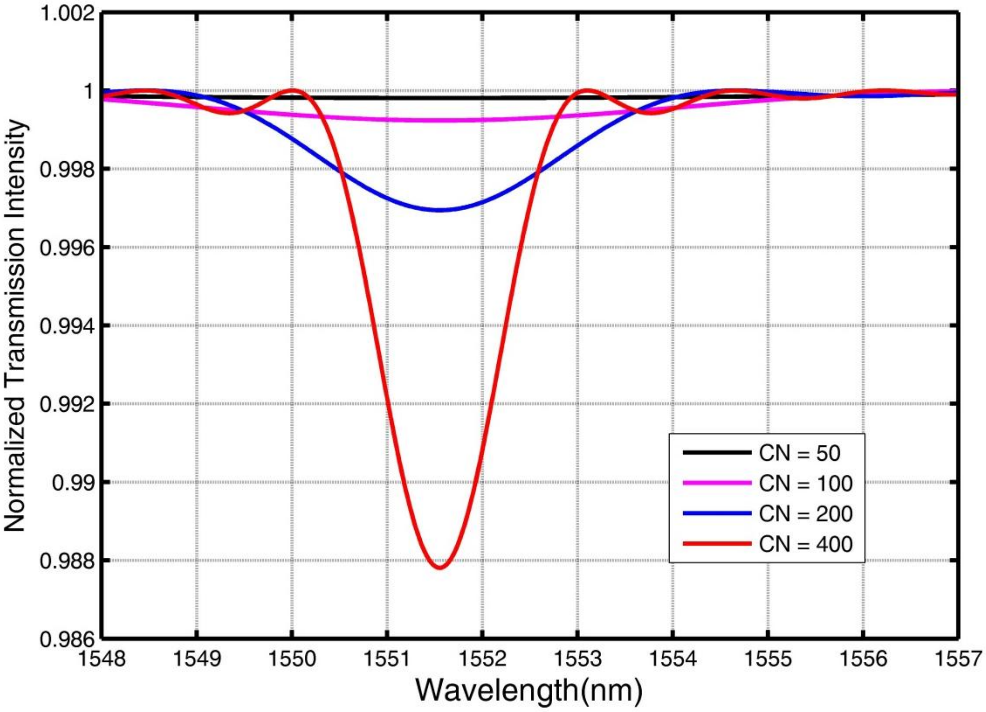

Figure 3.18. Simulated transmission spectra of T-LPG of different lengths.

3.5 Sensing Principle

LPG has been demonstrated sensitive to a number of physical, chemical and biological parameters [18, 58, 105]. Because the field of cladding modes can extend beyond the physical boundary of the fiber or into the fiber surface coating, it is sensitive to changes in the fiber surrounding medium or in the surface coating, which can affect the phase matching condition resulting in a shift in the LPG resonance wavelength.

According to Equation (3-15), the T-LPG resonance wavelength is determined by:

$$\lambda_{res} = \lambda_a \cdot \Delta n_{eff} \qquad (3\text{-}15)$$

where λ_a is the acoustic wavelength, and in the previous discussion, we ignore the axial strain applied on the fiber and get the approximation expression in Equation (3-15). But since in the following discussion strain is a potential measurand, we will not ignore it in the acoustic wavelength calculation. According to Equation (3-19), the acoustic wavelength with consideration of axial strain ε is given by:

$$\lambda_a = \frac{v_a}{\sqrt{2} f_a} \sqrt{\varepsilon + \sqrt{\varepsilon^2 + \frac{4\pi^2 R^2 f_a{}^2}{v_a{}^2}}} \tag{3-35}$$

So we can rewrite the T-LPG resonance wavelength equation which is also the T-LPG phase matching condition as:

$$\lambda_{res} = \frac{v_a}{\sqrt{2} f_a} \sqrt{\varepsilon + \sqrt{\varepsilon^2 + \frac{4\pi^2 R^2 f_a{}^2}{v_a{}^2}}} \cdot (n_{core} - n_{clad}^i) \tag{3-36}$$

where R is the fiber radius, and f_a is the acoustic frequency applied on the PZT. These two parameters are not affected by the change in the fiber surrounding medium. The strain effect on λ_{res} is straightforward, and it has been used to tune the LPG resonance wavelength [106]. v_a is the acoustic velocity in the fiber, which is about 5760m/s in silica. It is determined by the fiber material as well as the temperature. The thermo-acoustic coefficient is defined as:

$$C_{TA} = \frac{1}{v_a} \cdot \frac{d(v_a)}{dT} \tag{3-37}$$

For pure silica, $C_{TA} = 9.6 \times 10^{-5} (1/^{\circ}\mathrm{C})$ [107]. This value varies with different dopants in silica. However, since the acoustic wave has much more field in the fiber cladding region than in the core region, using the thermo-coefficient for pure silica is a good approximation in our case.

n_{core} and n^i_{cl} are the effective indices of the core mode and the ith cladding mode. Both n_{core} and n^i_{cl} are temperature dependent, and their change with temperature is determined by the thermo-optic coefficient defined as:

$$C_{TO} = \frac{1}{n} \cdot \frac{dn}{dT} \tag{3-38}$$

For silica, $C_{TO} = 0.5\times10^{-6}(1/^{o}C)$ [108], which is much smaller than C_{TA}. So it means when temperature changes, the major effect on the LPG resonance wavelength shift is induced by the thermo-acoustic effect rather than the thermo-optic effect.

From the previous simulation, it is clear that n^{i}_{cl} is dependent on the refractive index of the fiber surrounding medium which is n_3 as illustrated in Figure 3.11. So any parameter that can affect n_3 will change n^{i}_{cl}, resulting in the change of λ_{res}. This is the sensing principle when there are chemical or biological stimuli in the fiber surrounding medium.

Chapter 4 Experimental Results

4.1 Physical Sensing

Generally speaking, temperature, strain and pressure are the most common parameters that physical fiber sensors measure. As mentioned in the sensing principle, T-LPG can measure temperature or strain by detecting the grating resonance wavelength shift. In our experiment, we chose temperature measurement to demonstrate the distributed sensing capability of T-LPG.

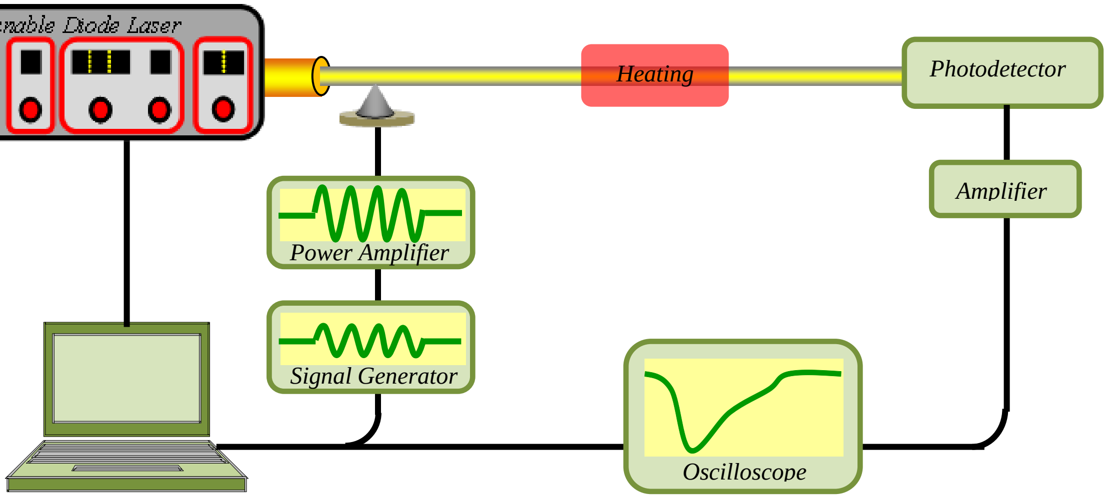

Figure 4.1. Schematic of T-LPG distributed temperature measurement setup.

The experimental setup is schematically shown in Figure 4.1. The acoustic frequency was set as 2.461MHz, and the generated LPG had 678 μm period which led to the resonance wavelength of ~1540nm. The signal generator was operated in burst mode with 200-cycle sinusoidal waves in each burst, corresponding to about 14cm LPG length. The total length of the sensing fiber was 2.5m, so the burst rate was set as 500Hz to make sure that at any time there was only one LPG at most propagating in the fiber. The voltage applied on the acoustic horn was about $40V_{p\text{-}p}$. A tunable laser (New Focus 6328) was used as the optical source, whose wavelength was scanned from 1530nm to 1560nm at a step size of 0.1nm. At each wavelength, the change of the light intensity output from the fiber end was received by a photodetector (HP 11982A), and recorded as a function of the acoustic wave travel time by an oscilloscope (LeCroy LT322). The acoustic wave travel time was mapped to the fiber location by perturbing the fiber at specific locations and observing the signal variations from the oscilloscope. After scanning the laser wavelength, the LPG transmission spectrum at a specific location of the fiber was constructed from the intensities recorded by the oscilloscope that corresponded to the location at all wavelengths. A ~20cm fiber section was heated by a hotplate to different temperatures ranging from the ambient temperature (22°C) to 111°C at a step of about 10°C. The temperature was monitored by a thermocouple.

Figure 4.2 shows how the LPG transmission spectrum changed as the LPG traveled along the fiber when the fiber was at ambient temperature 22°C (a) and heated to 111°C (b), respectively. The black curves in Figure 4.2(b) plot the T-LPG transmission spectrum at the heated section. It is evident the spectrum is shifted for the heated area while the spectra remain unchanged for the other locations. The distance between two neighboring curves is 8cm, so the heated fiber section covers two curves in the figure. Figure 4.2(c) shows a more detailed gradual shift of the heated fiber section, in which the distance between two neighboring curves is 1cm. Therefore, it is clear that the spatial resolution is smaller than 14cm which is the length of T-LPG.

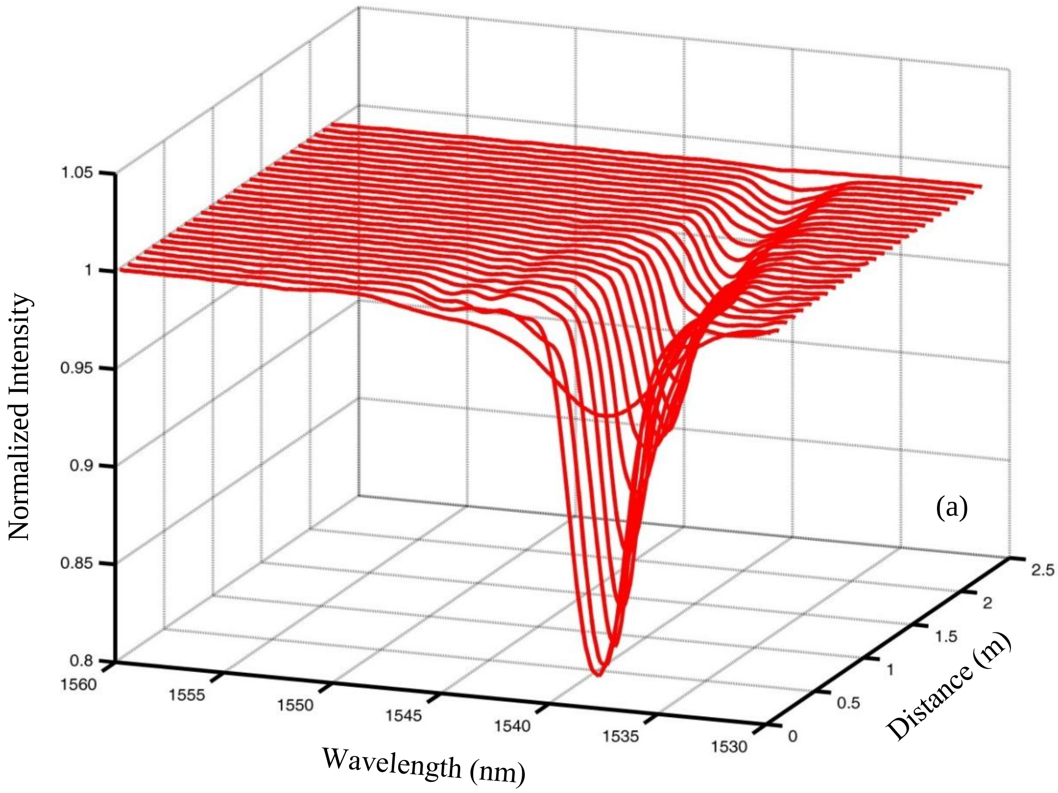

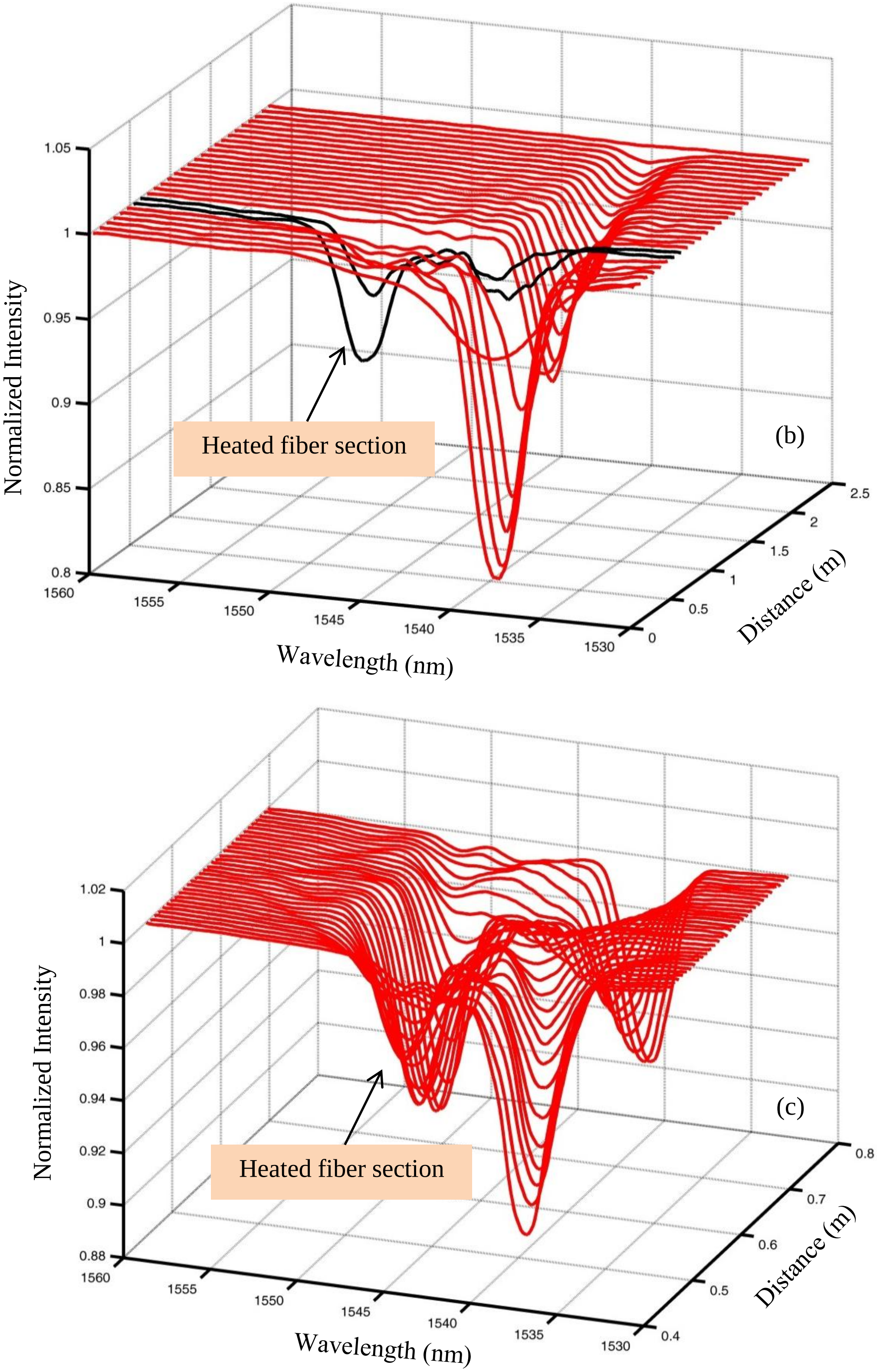

Figure 4.2. Experimental results of the T-LPG spectral evolution as the LPG was traveling along the fiber under different temperatures: (a) 22^{0}C, (b) and (c) 110^{0}C.

The T-LPG resonance wavelength shift amount as a function of the fiber distance at different temperatures is plotted in Figure 4.3(a). The T-LPG resonance wavelength was shifted toward longer wavelength at the heated area while remaining largely unchanged at the other parts of the fiber. It also clearly shows that temperature can be continuously monitored along the fiber by monitoring the resonance wavelength. The temperature sensitivity is about 0.097nm/^{0}C, as shown in Figure 4.3(b), which plots the LPG resonance wavelength against the temperature change at the heated fiber area. The blue dots are the experimental results, and they can be well fitted by a straight line. The experiment results demonstrate that T-LPG can be used for distributed temperature measurement by spatially monitoring the T-LPG resonance wavelength along the fiber.

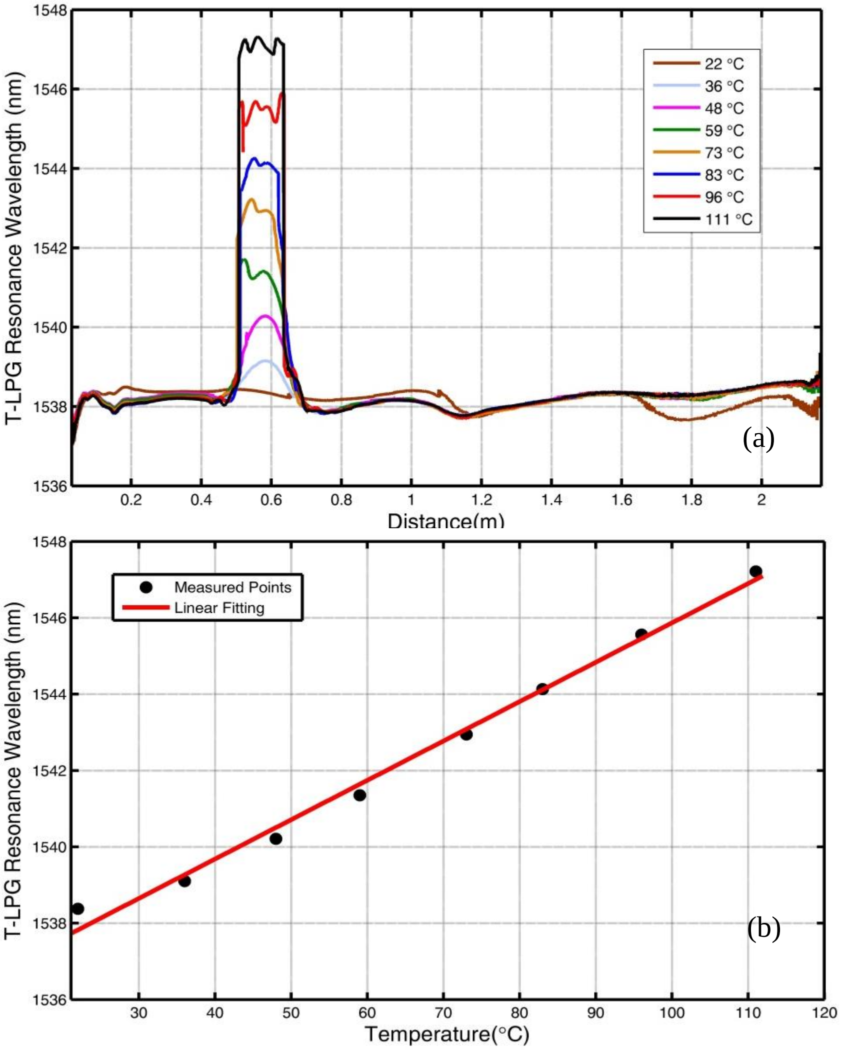

Figure 4.3. Experimental results of the T-LPG resonance wavelength as a function of: (a) distance and (b) temperature.

4.2 Biological Sensing

The principle of using an LPG for biological sensing is usually based on specific binding between the functionalized fiber surface and the intended biochemical species, which causes a change in the effective thickness of the fiber and consequently shifts the LPG resonance wavelength[13, 20]. There are many kinds of biosensors according to different classifications of biological species. In our experiment, we chose immunosensors, an important and intensively investigated group among biosensors. Immunosensing is based on specific molecular recognitions by antigen-antibody reactions, which can form a stable complex that causes changes of both size and reactive index in the sensing medium. Specifically in the experiment, we measured the interaction between immobilized immunoglobulin G (IgG) and its corresponding antigen, a mature biological sensing technology. The sensing principle is conceptually illustrated in Figure 4. 4.

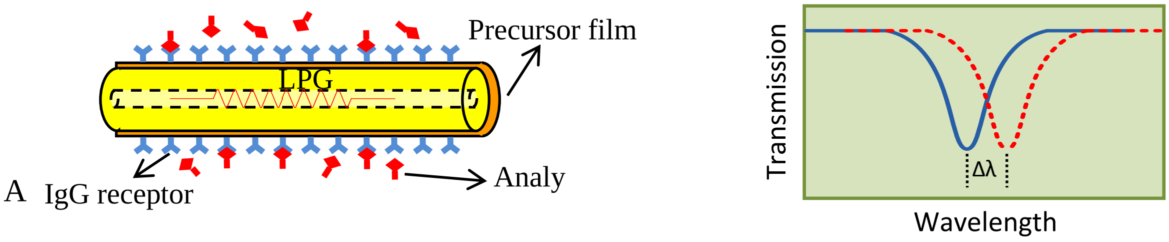

Figure 4.4. Schematic of immunosensing principle.

distributed sensor for detection of anti-pig IgG was demonstrated by functionalizing the sensing fiber surface with pig IgG. The system setup is similar to the one shown in Figure 4.1, the difference is instead of a heating furnace a glass U-groove with solutions in it was used to functionalize a desired fiber section, as shown in Figure 4.5.

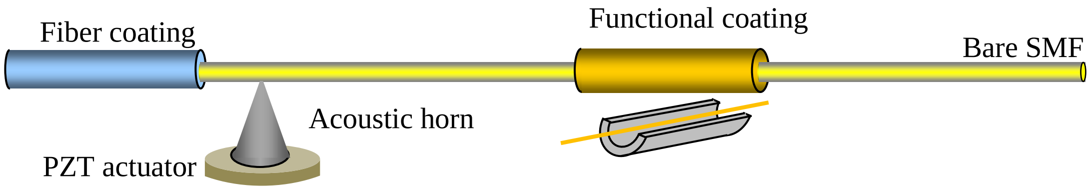

Figure 4.5. Schematic of part of the immunosensing experiment setup.

Biological molecules are highly efficient at recognizing specific analytes or catalyzing reactions; however, only in specific aqueous media [109]. A preferred medium is needed to avoid denaturation or loss of reactivity in many cases where biomolecules are directly bound to solid surfaces through adsorption. So in biological sensing, people usually use immobilization techniques to stabilize and preserve the reactivity of biomolecules [109]. Organic thin films are very popular for supporting or embedding the biomolecules, and it has been demonstrated that polymer self-assembly is an effective method for immobilization of biological molecules [110]. So in our experiment, we use the layer-by-layer electrostatic self-assembly (LbL/ESA) method to functionalize the fiber section.

LbL/ESA has been extensively investigated for biological sensing and is considered a highly feasible nanofabrication technique capable of depositing a variety of thin films of nanometer thickness for biological species and agents [111, 112]. LbL/ESA can provide precise control of the thickness of a thin film in the range from a few angstroms up to a micron. It also well controls the thin film structure in the vertical dimension. Its basic concept is driven by charge neutralization and resaturation upon adsorption of charged materials on oppositely charged surfaces. The basic process involves the immersion of a charged substrate into oppositely charged aqueous poly-electrolytic solutions of polyanions and polycations in alternating sequence at room temperature and ambient conditions [113]. These processes result in an alternating change in the surface charge and lead to a continuous assembly between positively and negatively charged materials (polycations and polyanions, respectively). The properties of the thin film are determined by the properties of individual molecules and the dipping sequence.

Figure 4.6 schematically shows the LbL/ESA process. A clean charged substrate (negatively charged as shown in the figure) is dipped into the polycation solution, and a monolayer of polycation molecules is deposited on the substrated because of the Coulombic attraction between the oppositely charged substrate and the polycation. Further polycation adsorption is limited once the deposition of one monolayer of polycation tends to be saturated. Then the polycation-coated substrate is rinsed with deionized water to remove excess polycation molecules that are not ionically bonded. After that, the substrated is immersed into the polyanion solution. Another monolayer of polyanion molecules is absorbed onto the substrate also due to the Coulombic attraction. The combination of one monolayer of polycation and polyanion is called a bilayer. By repeating these two steps, a multilayer thin film with an $(AB)_n$ structure is formed. The growth process for LbL/ESA is quick with a few minutes per layer.

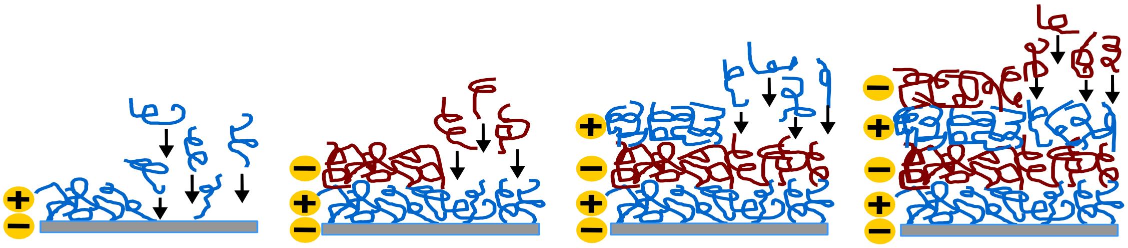

Charged substrate and assembly of first polyelectrolyte monolayer

Assembly of second polyelectrolyte monolayer to form a bilayer

Assembly of third polyelectrolyte monolayer on top of the bilayer

Assembly of fourth polyelectrolyte monolayer to form the second bilayer

Figure 4.6. LbL/ESA process for the formation of multilayer thin films.

In our experiment, a 10cm fiber section was used as the substrate for LbL/ESA. It was first cleaned in piranha solution (H_2O_2: H_2SO_4 = 30/70 v/v) at room temperature for 30minutes. After that, the fiber was ultrasonically rinsed in ultrapure water and dried in ambient condition. The ultrapure water was obtained by reverse osmosis (Barnstead Diamond RO) followed by ion exchange and filtration (Barnstead Nanopure Diamond UV/UF). Then the fiber was immersed into the polycation solution for 5 minutes, followed by rinsing in ultrapure water and drying. Then the fiber was dipped into the polyanion solution for 5 minutes, also followed by rinsing in ultrapure water and drying. The polycation and polyanion solutions in the experiment were poly {1-(4-(3-carboxy-4-hydroxy-phenylazo) benzenesulfonamido)-1, 2-ethanediyl, sodium salt (PCBS) and Polyallylamine hydrochloride (PAH), respectively. Their solutions are of 10mM concentration with 7.5 pH value. Under this condition, the thickness of one bilayer PAH/PCBS is about 2.3nm, and refractive index is about 1.695 [113]. Using LbL/ESA, a thin film of ten bilayers of (PCBS/PAH) was deposited onto the fiber substrate. This 10cm section was tested by the T-LPG in a 2.5m fiber. The acoustic frequency was 3.745MHz, corresponding to T-LPG with 550 µm grating period and resonance wavelength at 1548nm. The length of the T-LPG was controlled as 11cm by setting 200 cycles in each acoustic burst. The experiment results are shown in Figure 4.7. The T-LPG transmission spectra at different locations were plotted in Figure 4.7(a), with black curves showing the thin film deposition position. Figure 4.7(b) plots the T-LPG resonance wavelength at different thin film thicknesses, The 5 and 10 PAH/PCBS bilayer thin film coatings shifted the T-LPG resonant wavelengths toward shorter wavelengths by approximately 0.5 nm and 1 nm, respectively.

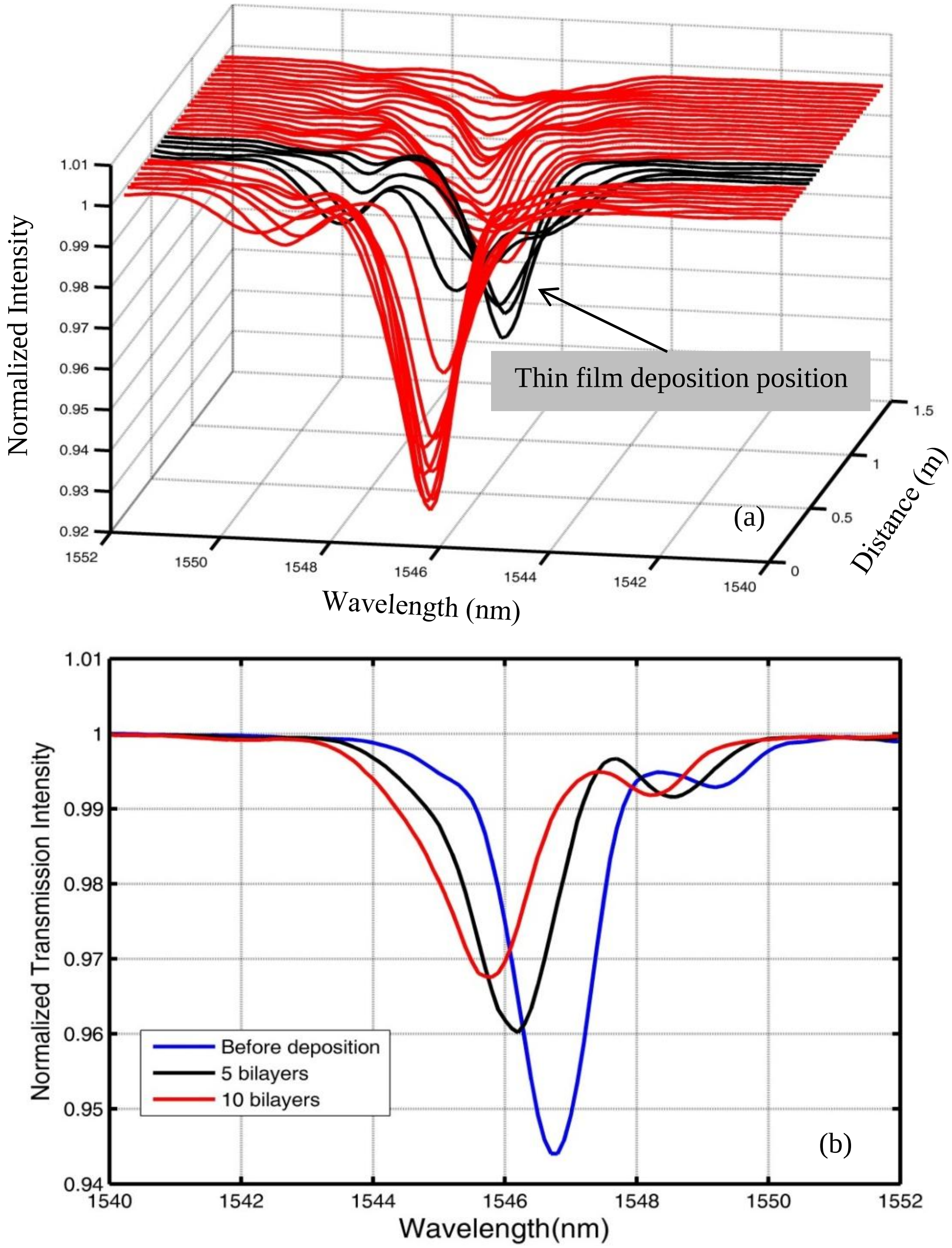

Figure 4.7. Thin film deposition experimental results for T-LPG transmission spectra at: (a) different locations along the fiber; (b) different deposition thicknesses.

The fabricated PAH/PCBS thin film works as a precursor layer in biological sensing for Igg and anti-IgG detection. It is used to support IgG molecules because IgG molecules can be absorbed onto the polymeric surface by hydrophobic and electrostatic interactions [109].

After the precursor layer deposition, the pre-coated fiber was subsequently immersed into a pig IgG solution of 0.05mg/mL concentration for one hour and then a standard binding block solution (2% bovine serum albumin (BSA)) for another hour. Each of these two steps introduced an additional -0.1nm shift on the LPG resonance wavelength, and the fiber was washed by ultrapure water after each step in order to remove the only partially adsorbed material. The blocking is a standard procedure in immunosensing to avoid non-specific binding by using BSA or other proteins to cover the portion of the fiber surface which is not covered with pig IgG. This step completed the sensor fabrication process.

Figure 4.8(a) presents the LPG transmission spectrum at it is propagating along this pretreated fiber. The spectrum in red line shows the position of the functional coating which has a wavelength shift towards shorter wavelength. Then the sensor was tested with a cross-reactivity experiment. The effectiveness of the binding block layer, which is designed to minimize non-specific binding, was tested via exposure to an anti-rabbit IgG, unrelated antigen.

Figure 4.8(b) shows the fabrication and testing of the traveling LPG immunosensor. For each rectangular box in the figure, the central red line is the median, and the blue edges of the box are the upper and lower quartile. The error bars were computed with 20 samples for each testing step, and the standard deviation is 0.02nm. Therefore, from the results, we can conclude that fully-distributed immunosensing can be realized by having the entire length of an optical fiber pretreated by the method described above. Furthermore, by changing the deposited molecules according to different specific binding pairs, many other biological agents can also be detected.

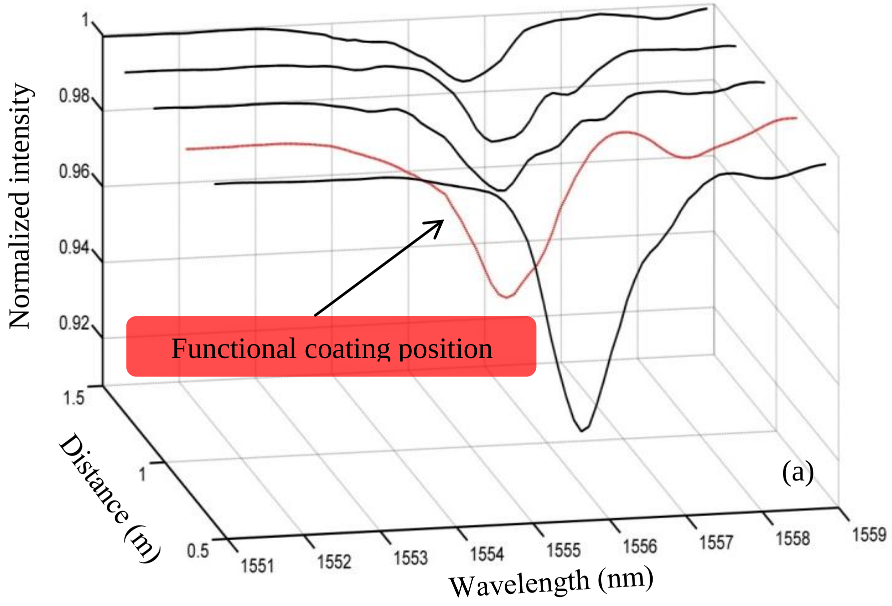

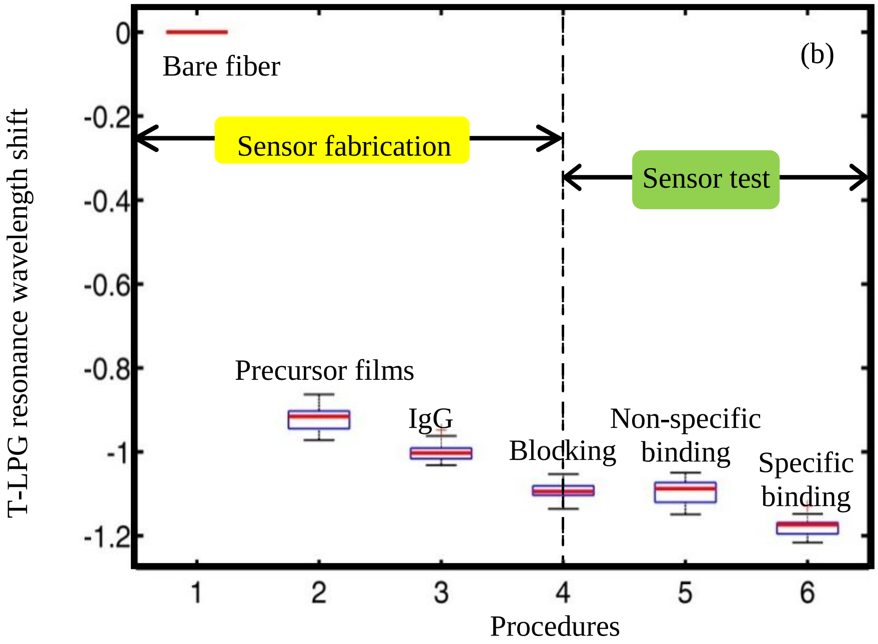

Figure 4.8. Distributed immunosensing results. (a) Evolution of T-LPG transmission spectrum along a pretreated fiber. (b) T-LPG resonance wavelength shift during film synthesis and sensor test.

4.3 Chemical Sensing

In the chemical sensing experiment, we demonstrated hydrogen sensing, which is of great interest among many topics of chemical sensing because of its participation in a wide range of chemical processes and its emerging importance as a promising clean source of energy. Hydrogen is very reactive, and well-known for its high risk of explosion. It is has a low explosive limit as 4.0% and a wide explosive range up to 74.2%, with a flame velocity almost ten times higher than that of natural gas [114, 115]. Therefore, in order to address the safety concern due to potential leaks, hydrogen leakage detection and monitoring is often essential. Moreover, distributed monitoring of hydrogen is becoming more and more desirable in today's complex industrial facilities, gas delivery systems and civil infrastructure sites. Fiber-optic sensors are superior to electrical sensors for hydrogen detection because of no detonation risk from electric arcing. Sumida et al. reported a distributed hydrogen sensing technique using specially designed fibers with hydrogen sensitive materials as the fiber cladding [116], and a few meter spatial resolution was reported. Using the traveling LPG method, we realized fully-distributed hydrogen detection by coating a regular SMF with platinum (Pt) and a spatial resolution of 10cm is obtained. The sensing principle is when the fiber is exposed to hydrogen; the presence of Pt will convert H_2 and O_2 to H_2O and gives off heat. The resulted temperature increase causes a shift in the LPG resonance wavelength. Therefore, by measuring the LPG resonance wavelength at different locations along the fiber, distributed hydrogen detection can be realized.

In the experiment, a Pt thin layer was deposited onto a 20cm fiber section using physical vapor deposition (PVD), and the thickness of the Pt layer is about 200nm estimated from the deposition rate. This Pt coated fiber section was placed in an open-end gas tube which was connected to a gas chamber with premixed hydrogen of certain concentrations, as illustrated in Figure 4.9. The diameter of the gas tube is 1cm, and the length is 20cm. The pressure of the out coming gas from the gas chamber was precisely controlled by a gas regulator, which together with the open-end structure can minimize the influence of the gas pressure on the acoustic LPG spectrum change.

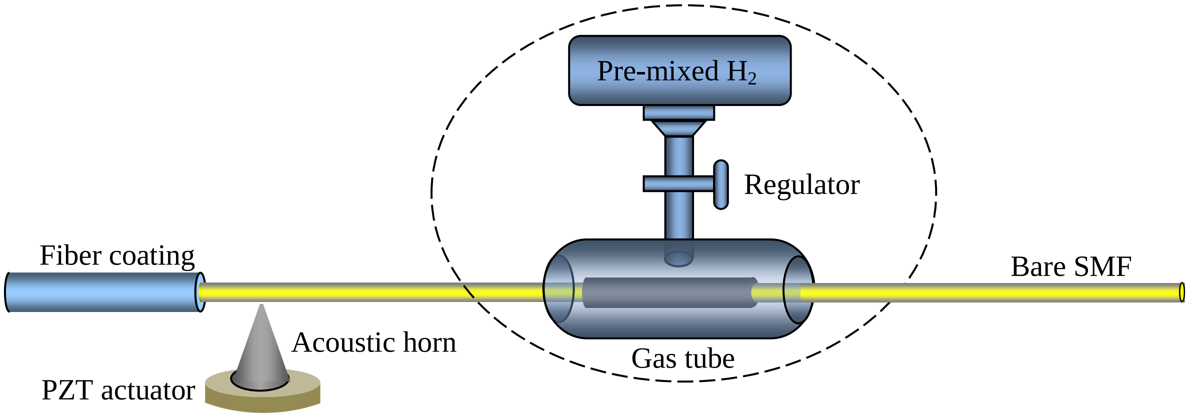

Figure 4.9. Schematic of part of the hydrogen sensing experiment setup.

The LPG transmission spectra at different locations of the fiber are shown in Figure 4.10(a). The spectrum in red is at the pt-coated position, while the others are at non-coated region. The Pt layer introduces a wavelength shift (blue shift) and also weakens the spectrum intensity, which could limit the maximum sensing length of the system. To test the influence of the gas flow perturbation on the acoustic LPG, we also measured the acoustic LPG spectrum change for pure nitrogen.

Figure 4.10 (b) presents the LPG spectra at the functional fiber section under different situations, and (c) is the error bar analysis computed with 20 samples for each testing step (rectangular box in the figure). Concluded from the results, gas flow could shift the acoustic LPG spectrum, which, however, is much smaller than the wavelength shift introduced by the hydrogen. Therefore, the gas flow perturbation can be viewed as the system noise, which could possibly be further reduced by improvements in the application of hydrogen to the sensor.

Figure 4.10 (d) shows the sensor response to hydrogen. The wavelength shift rate is about 0.04nm for one percent of hydrogen, and the standard deviation in the resonance wavelength measurement is 0.0099nm. The linear fitting line has a non-zero value when the hydrogen concentration is zero. This is because of the gas flow perturbation as mentioned before.

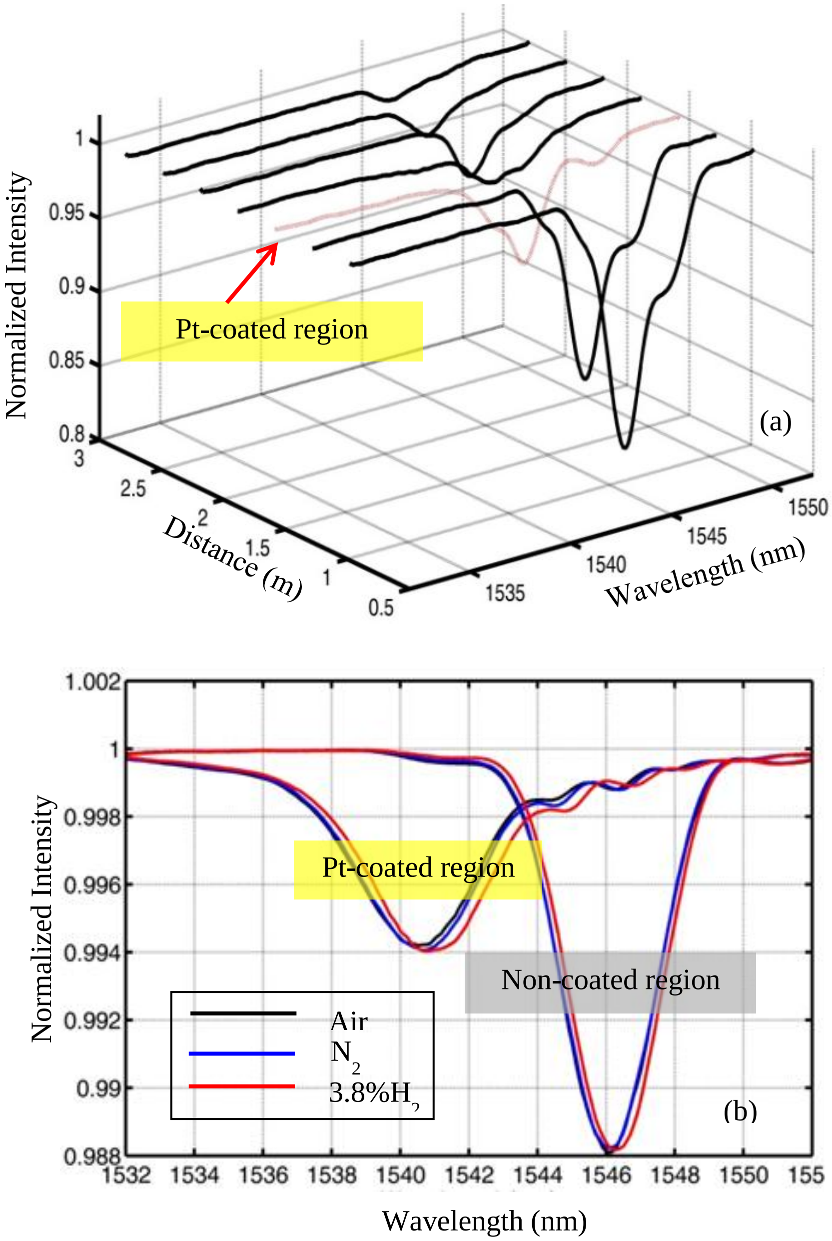

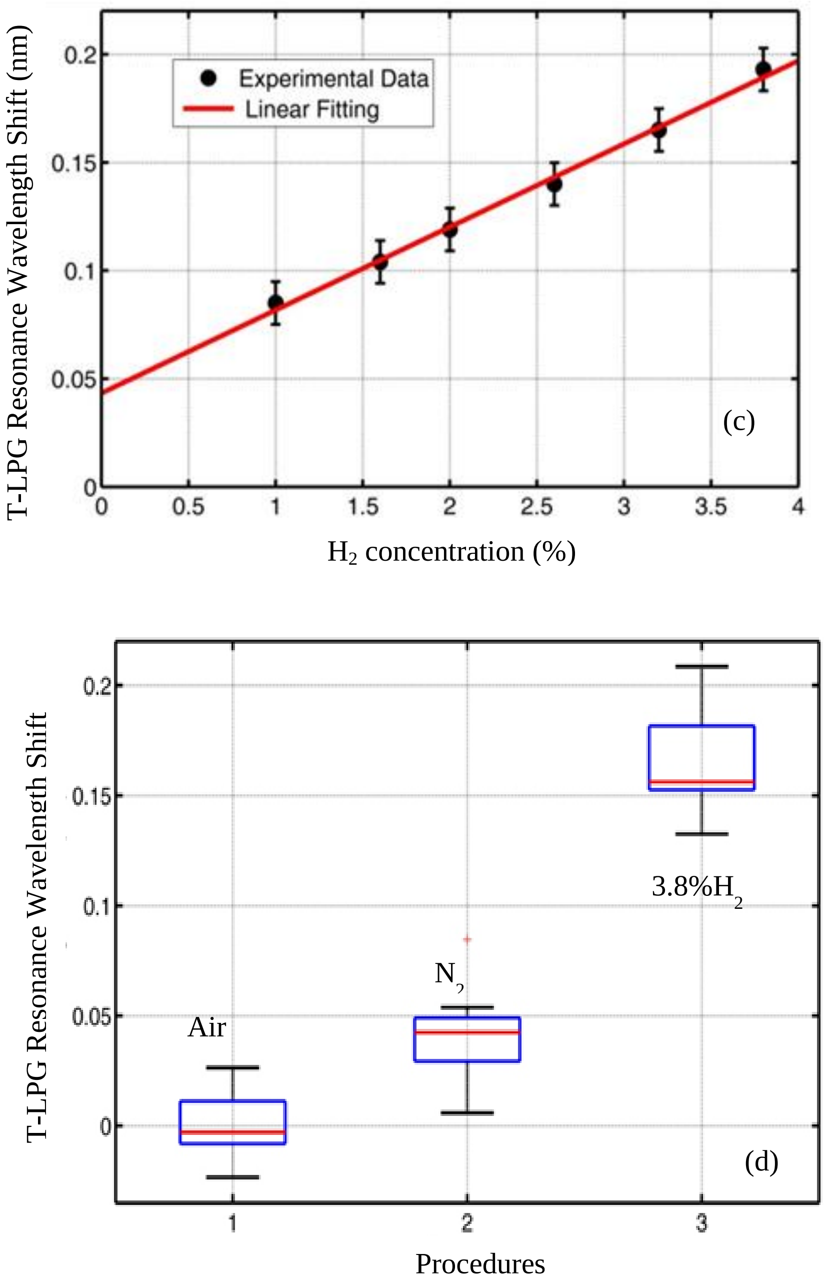

Figure 4.10 Distributed hydrogen sensing results: (a) Spectra of T- LPG at different locations along the fiber. (b) T-LPG spectra and (c) T-LPG resonance wavelength shift at the Pt coated fiber section under different situations; (d) T-LPG resonance wavelength shift.

The response and recovery times for the H_2 - O_2 reaction are approximately 3 and 10 minutes, respectively [117]. The actual system response and recovery times were not measured in our experiment because the system response and recovery time is much more determined by the data acquisition time which is about 5 minutes or even longer depending on the average times.

4.4 Temperature Compensation

All optical biological and chemical sensors are susceptible to thermally-induced fluctuations. Temperature variations inevitably cause changes in refractive index and material volume via the thermo-optic effect and thermal expansion of the optical material. T- LPG enables a unique way to compensate for the temperature induced detection errors. It measures the temperature along the fiber, and uses this information to compensate the thermal resonance wavelength shift through signal processing. The principle is schematically shown in Figure 4.11 (a).

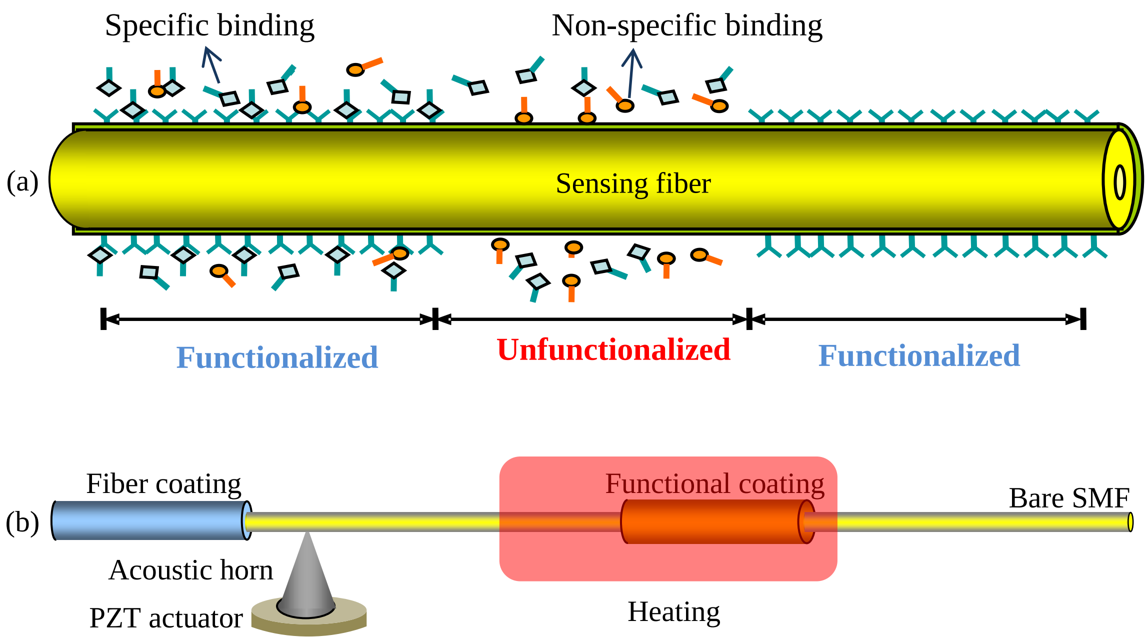

Figure 4.11. Schematic of temperature compensation: (a) principle and (b) experiment setup.

When the T-LPG is used for biological or chemical sensing, some sections of the fiber are intentionally left unfunctionalized. In most cases, the temperature variations of the neighboring functionalized and unfuntionalized areas can be considered identical and cause identical shifts of the T-LPG resonance wavelengths; while the specific binding of biochemical specifies can only cause T-LPG resonance wavelength shift in the functionalized area. Therefore, temperature cross-sensitivity can be compensated for when the difference of the T-LPG resonance wavelengths in the two areas is used as the detection signal. Compared with active temperature control, in which usually a thermal electric cooler is used to stable the temperature, temperature compensation is passive and does not require separate electrical cabling, retaining the electromagnetic immunity and eliminating the electric sparking possibility, traits that are essential for applications in explosive environments.

To test this temperature compensation capability, a 2.5m fiber with 10cm functional coating was heated to simulate the temperature variation environment, as illustrated in Figure 4.11 (b). The test results are plotted in Figure 4.12, which shows the T-LPG transmission spectra of functionalized and unfunctionilized positions measured at two different environmental temperatures (23 and 28 ℃). It shows that although the environmental temperature variation caused the LPG resonant shift at both points, their resonant wavelength differential remained unchanged.

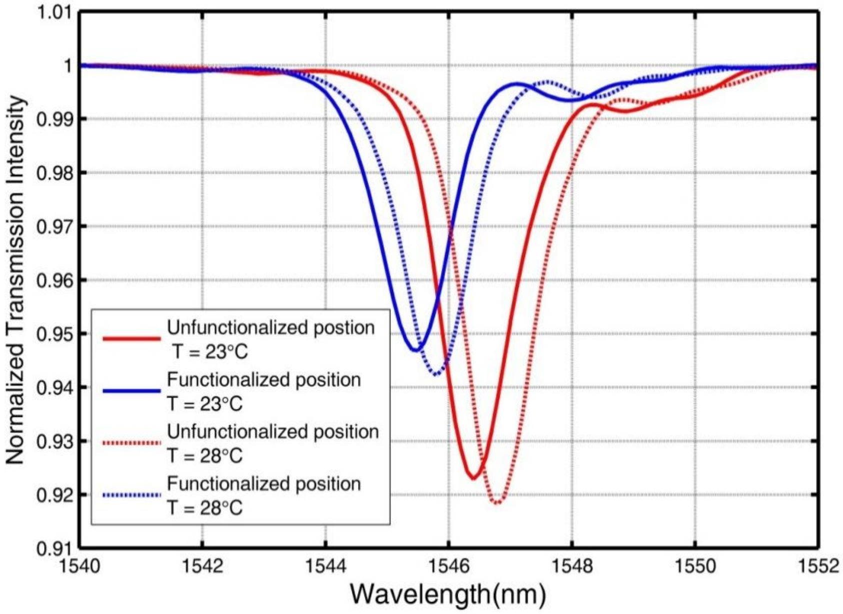

Figure 4.12. T-LPG spectra at different locations under different temperatures.

4.5 Traveling Rocking Grating

Previous T-LPG experiments are based on flexural acoustic waves. Besides flexural waves, torsional and longitudinal acoustic modes can also exist in the cylindrical silica waveguide structure [118]. However, compared with acoustic torsional wave, acoustic flexural wave attenuates more quickly in optical fiber, and is more vulnerable to fiber bending and other unwanted physical contacts [119]. In this section, T-LPG generated by a torsional acoustic mode is investigated for temperature sensing.

The traveling rocking grating is enabled by pulsed acoustic torsional waves propagating in an single-mode polarization maintaining fiber (PMF), and the sensing mechanism is based on the changes in the acoustic properties of acoustic torsional wave with the surrounding medium. In our previous work, we demonstrated fully-distributed sensing using an acoustically generated long period grating, formed by acoustic flexural waves [78, 120]. Using acoustic torsional waves to generate a rocking grating has been studied in the past [121, 122], but the acoustic waves used in their works were continuous waves. Their applications have been limited to tunable filters for optical communications. Moreover, traditional rocking gratings are usually inscribed permanently into optical fibers by a complicated fabrication technique, usually achieved by mechanically twisting the fiber in the fiber drawing process [123, 124] or in the grating writing process [125]. Therefore, the acoustically-induced traveling and transient rocking grating provides an effective means of high sensitivity and low cost to the fully-distributed temperature sensing; and it may also serve other fully-distributed sensing applications, e.g. pressure and transverse stress.

An optical rocking grating is a type of long-period grating in a PMF that rotates the polarization state of the light between the two orthogonal degenerated modes of the core mode by periodically twisting the principal axes of the fiber at a rocking angle. When the input light is launched into a PMF at one of the principal axes, it is coupled to the other principal axis at a certain wavelength where the phase matching condition is satisfied. So if we monitor the power intensity of the output light at the input polarization state, there is a dip in the received transmission spectrum at that wavelength, which is the resonance wavelength. When the periodic twisting is induced by a torsional mode acoustic wave, the generated rocking grating becomes transient, and the grating pitch length is equal to the acoustic wavelength. This is the phase matching condition of the rocking grating, which is the same to that of the LPG generated by acoustic flexural wave, given by Equation (3-14). The difference is in the case of acoustic flexural wave, the two modes are the core mode and one cladding mode; while for the acoustic torsional wave case, the two modes are the two degenerated modes of the core mode. So the phase matching condition can be written as:

$$\lambda_r = B_f \cdot V_{at} / f_{at} \tag{4-1}$$

where λ_r is the resonance wavelength; B_f is the fiber birefringence; V_{at} and f_{at} are the acoustic torsional mode velocity in the fiber and the acoustic frequency, respectively. When there is a temperature (T) change to the fiber, the resonance wavelength of the rocking grating will be shifted. The temperature sensing principle is given by:

$$\frac{d\lambda_r}{\lambda_r \cdot dT} = \frac{dB_f}{B_f \cdot dT} + \frac{dV_{at}}{V_{at} \cdot dT} \tag{4-2}$$

Unlike traditional permanent rocking gratings, the acoustically induced rocking grating is affected by not only the fiber birefringence, but also the acFiber oustic velocity in the fiber. And both of them are temperature dependent, resulting in a shift in the grating resonance wavelength with the temperature change.

Figure 4.13 illustrates the operation principle of acoustic torsional wave generation and coupling to a PMF. A flexural wave is generated by a piezoelectric transducer (PZT) disk vibrating in thickness mode and excited into a 4mm-long side fiber by a horn amplifier. At the end of the side fiber where it is glued onto the sensing fiber (main fiber) using a UV epoxy, the flexural wave gives rise to an acoustic torsional wave in the sensing fiber. Both of the sensing fiber and the side fiber are bare fibers of 125 μm diameter without polymer coating to reduce acoustic loss.

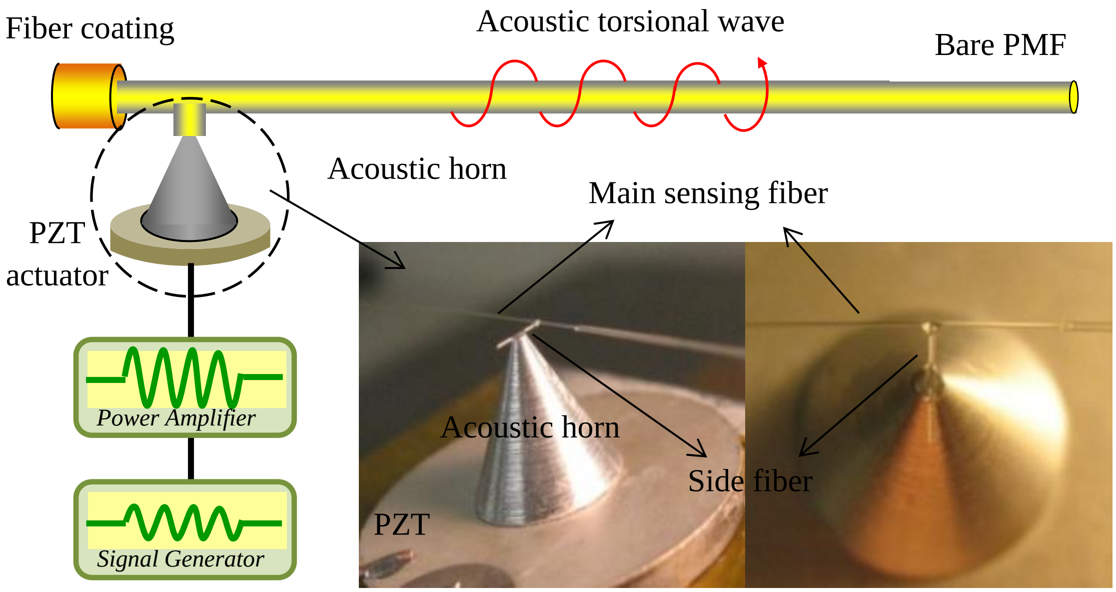

Figure 4.13. Operation principle of acoustically generated rocking grating.

Figure 4.14 is the schematic of experimental setup used for the demonstration of the proposed distributed temperature measurement in a 3m sensing fiber. To have acoustic pulses to generate a transient and traveling rocking grating, the signal generator driving the PZT was operated in burst mode. Each burst, corresponding to one grating, consisted of 200 cycles (number of grating periods) of a sinusoidal wave whose frequency was chosen to 860 KHz in order to match the beat length of the sensing fiber at 1550nm, which is about 4mm. So the generated grating length is about 80cm. The burst repetition rate was 500Hz to make sure there was only one grating traveling in the whole fiber span at a time. A tunable laser was used as the optical source, whose wavelength was scanned from 1500 to 1580nm at a step size of 0.1nm.

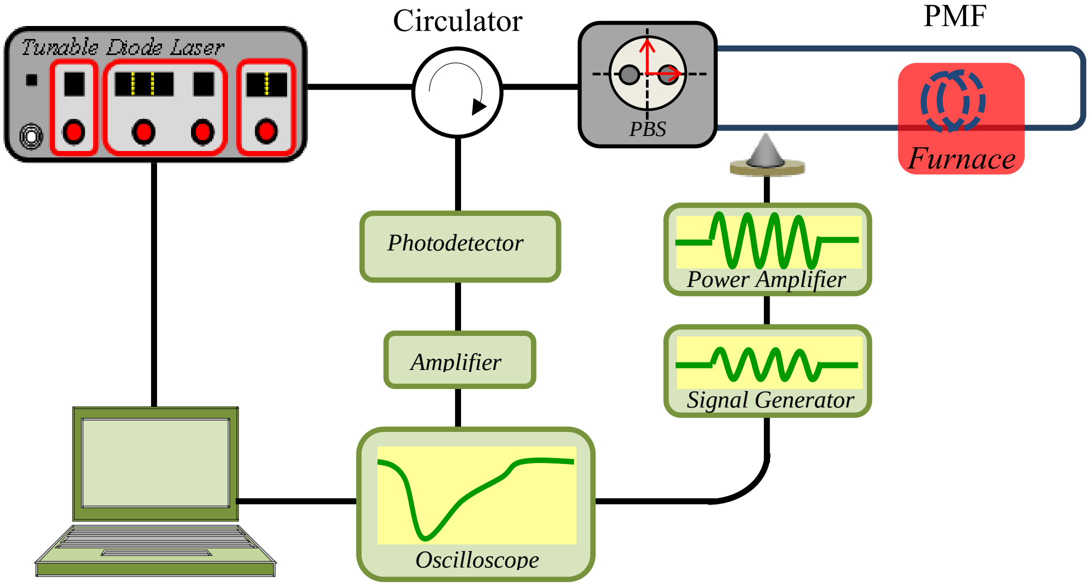

Figure 4.14. Schematic of acoustic torsional wave based T-LPG distributed temperature measurement setup.

At each wavelength, the change of the light intensity output from the fiber end as a function of the acoustic wave traveling time was recorded by an oscilloscope. After scanning the wavelengths, the grating transmission spectrum at any location of the fiber was reconstructed. The timing of the acoustic pulse relative to the optical measurement provides the information about the spatial location of the grating. At the polarization beam splitter (PBS), the incident light is divided into two output paths according to the power ratio of the two orthogonal polarizations in the input light. Both of the PBS output light beams are aligned on the slow axis of the output PMFs, so their polarization states are the same in the two output ports although they are orthogonal in the original input light. Then both of the two output light beams from PBS propagate in the grating section in opposite directions, and at the grating resonance wavelength (λ_r) each of them is converted to the other by the rocking grating. So after their round-trip in the fiber loop containing the rocking grating, both of the two light paths have opposite polarization directions as compared to their original one, which cannot be coupled back through the PBS to the input port. Therefore, only the light at the resonance wavelength is removed at the PBS, and the light at non-resonance wavelength is collected back at the detector, resulting in a spectrum dip at the resonance wavelength. A furnace was used to uniformly heat a fiber section of 1m to different temperatures, which was monitored by a thermal couple.

The measured transmission spectra at different temperatures are shown in Figure 4.15(a), and the non-heated region in the figure is the fiber section before it entered the furnace whose spectrum remained almost unchanged at different temperatures while the spectrum at the heated region was significantly shifted to smaller wavelengths when the temperature was increased. The measured temperature range in the experiment was about 20^0C, limited by the wavelength range of the optical source. Figure 4.15(b) shows how the grating transmission spectrum changed as it was traveling along the fiber when the heated fiber section was at 40^0C. It is evident that the grating transmission spectrum was gradually shifted when passing through the heated region, and then shifted towards the original wavelength at the non-heated regions afterwards. It clearly demonstrates that the temperature can be continuously monitored along the fiber by monitoring the grating resonance wavelengths. It is also seen that the rocking grating attenuates rapidly as the acoustic torsional wave propagates in the fiber, which could limit the measurement distance. The measured attenuation of the acoustic torsional wave in the fiber is about 2dB/m, but the maximum sensing length can be easily increased by coupling a stronger acoustic torsional wave into the fiber using an improved acoustic excitation and coupling setup.

Figure 4.15 (c) plots the temperature sensitivity of the resonance wavelength shift, which is about -1.6nm/^{0}C. So we can have $d\lambda_r/(\lambda_r \cdot dT)$ = 1000ppm/^{0}C, which is the left hand side in Equation (4-2). We also measured the fiber birefringence versus temperature change for the PMF used in the experiment using a Sagnac loop interferometer [126], and the result is shown in Figure 4.15 (d). The measured $dB/(B \cdot dT)$ is 844ppm/^{0}C, which is the first term on the right hand side of Equation (4-2). So we can get the second term $dV_a/(V_a \cdot dT)$ to be about 150ppm/^{0}C, and the calculated velocity of torsional acoustic mode in the given PMF is 3.7674×10^3m/s. Therefore, both the fiber birefringence and the acoustic velocity in the fiber contribute to the rocking grating resonance wavelength change with temperature, and the first one is dominant.

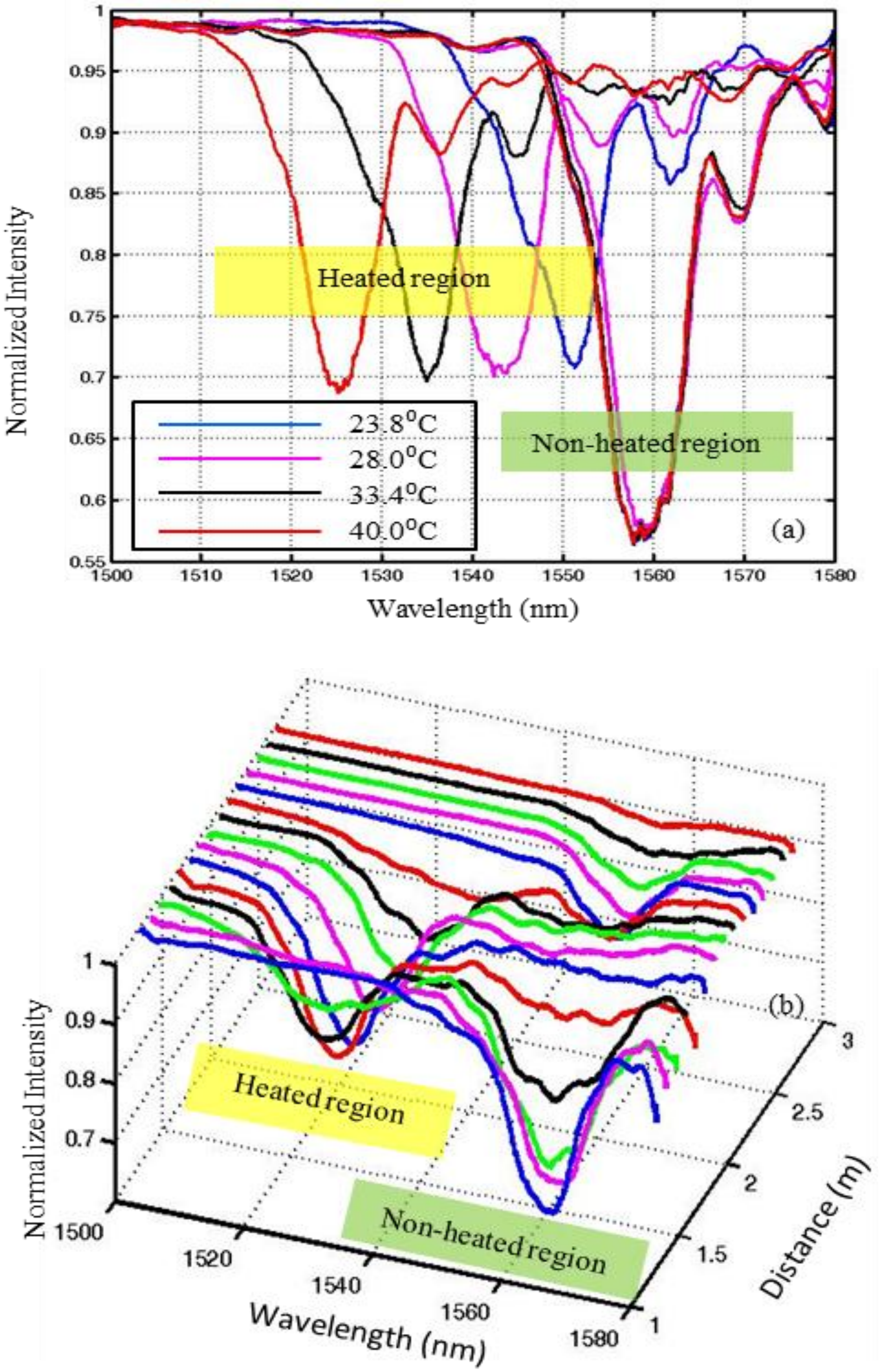

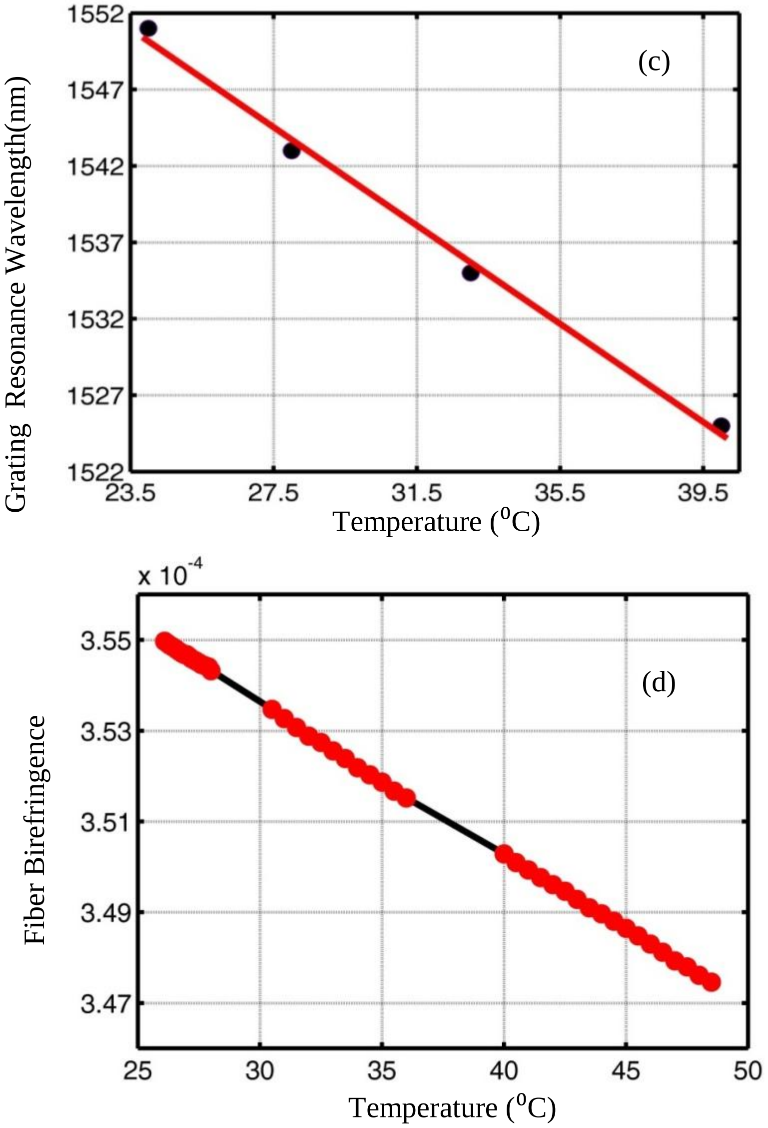

Figure 4.15. Distributed temperature measurement results: (a) spectra of rocking grating at different temperatures; (b) rocking grating spectral evolution as the grating travels along the fiber when the heated area was at 40^0C; temperature sensitivity of (c) rocking grating and (d) fiber birefringence .

Chapter 5 Conclusions and Future Work

5.1 Conclusions

In this work, a fully-distributed fiber-optic sensing technique based on a transient and traveling LPG in a SMF has been demonstrated. The T-LPG is generated by a pulsed acoustic wave with a finite overall length, and is made to propagate down the fiber along with a broadband optical pulse which serves as a sensing signal. Through control of the time delay between the T-LPG and the optical pulse, measurements can be made at any point along the fiber. Schematically varying this time delay generates a sampling of the measurement quantity along the length of the sensing fiber.

Based on this technique, we demonstrated fully-distributed temperature sensing, biological and chemical sensing by coating the fiber with functional coatings. In the temperature sensing experiment, a fiber was locally heated from room temperature (22°C) to ~110°C, and transmission spectrum of the T-LPG was monitored continuously along the fiber. The experiment results demonstrated the distributed measurement capability of this technique by showing T-LPG resonance wavelength shift only at the heated fiber position, and the resonance wavelength shift amount was proportional to the temperature change. In the biological sensing experiment, immunoglobulin G (IgG) was immobilized onto the fiber surface via ionic self-assembly, and we show that only specific antigen-antibody binding can introduce a measurable shift in the transmission optical spectrum of the traveling LPG when it passes through the pretreated fiber segment. It is also shown that non-specific binding to other unintended IgG can be avoided by the application of a standard binding block in the sensor fabrication. In the hydrogen sensing experiment, the fiber was coated with a platinum (Pt) catalyst layer, which is heated by the thermal energy released from Pt-assisted combustion of H_2 and O_2, and the resulted temperature change gives rise to a measurable LPG wavelength shift when the traveling LPG passes through. Hydrogen concentration from 1% to 3.8% was detected in the experiment.

This sensing technology is flexible in that it can be used to detect almost any stimulus that alters the properties of the acoustic wave (acoustic velocity) or the optical fiber (refractive index) or the surrounding area of the fiber (thickness, refractive index). Physical quantities such as temperature and strain can be measured directly by launching the T-LPG into a standard optical fiber. Various biological and chemical species can be detected using a sensing fiber with a functionalized coating. Through the use of specific functional coatings, deposited through established physical or chemical processes such as LbL/ESA, the sensing fiber can be made sensitive to a variety of biological and chemical species. By selecting uncoated and coated fiber regions with various functionalities, multiple physical, biological and chemical stimuli can be measured in a single distributed sensing link, resulting in a multi-functional sensing platform. Because the sensing element itself is comprised of low-cost commercially-available fiber, the T-LPG concept can provide the basis for wide-area sensor networks needed to monitor large-scale industrial process and environmental phenomena. The periodicity of the T-LPG is established by the excitation wavelength, so it is inherently highly uniform and can be very long. Additionally, cross-sensitivity to physical stimuli can be eliminated in the sensing fiber by changing the coated and un-coated sections through local measurement and compensation.

5.2 Recommendations of Future Work

The experiment results have demonstrated that the proposed T-LPG technique shows great promise in achieving fully-distributed physical, biological and chemical measurement. Using acoustic waves to generate LPGs also provides a large degree of freedom in the sensor design. By adjusting the acoustic wave frequencies, amplitude, and number of periods, we can readily control the LPG strength, resonance wavelength, resonance bandwidth, and cladding mode number. All these flexibilities, however, haven't been fully exploited to enhance the sensor performances. Moreover, there are a number of challenges that need to be addressed for this proposed sensing platform to be more practical. A major task among them is the acoustic excitation and confinement

In our experiment, we used standard optical fibers, whose coating is acrylates polymers with high acoustic attenuation, so we stripped off the polymer coatings and used bared fiber to guide the acoustic waves. There are several problems related to the bare fiber acoustic waveguding: 1. Bare fiber is fragile and not suitable for practical applications; 2. Despite the extremely small acoustic attenuation of fused silica (4.7dB/km at 2MHz[127]), the acoustic transmission length in a bare fiber exposed in air is severely limited by the extremely high acoustic attenuation of air

(6.4×10^5 dB/km at 2MHz [128]); 3. When the bare fiber is immersed into liquids or in contact with solid surfaces, acoustic waves can quickly dissipate into the environment, reducing the application flexibility and increasing the packaging difficulties. Therefore, methods that can better confine the acoustic within the sensing fiber for enhanced sensing range (hundreds of meters) are highly demanded.

One possible solution is to excite the acoustic wave with higher efficiency or to excite acoustic modes with lower attenuation in single-mode fiber. Generally, there are three types of acoustic modes transmitted in optical fibers: transverse, longitudinal, and torsional. The acoustic wave excited in the preliminary experiment is transverse mode, particularly the lowest-order flexural mode. Compared with the other two modes, transvers mode acoustic wave is the easiest to excite and coupled into optical fibers, however, it also has the largest attenuation [129]. And it has been reported that torsional acoustic wave is insensitive to fiber bending and physical contact. Therefore, we believe that by using acoustic modes with better transmission properties in optical fibers, the sensing span and the application flexibility could be greatly improved.

Another solution for this problem is using special fibers to form an acoustic waveguide, which consists of a core surrounded by a cladding with an acoustic wave velocity higher than of the core. The proposed acoustic waveguide structure is a direct analogy to optical fiber waveguide. And in the following analysis, we focus on acoustic wave in transverse and longitudinal modes. Assume for these two modes, similar to optical refractive indices, we have the acoustic refractive indices as:

$$\begin{aligned} n_{a,t} &= v_{t\_silica} / v_t \\ n_{a\_l} &= v_{l\_silica} / v_l \end{aligned} \tag{5-1}$$

where v_t and v_l are the transverse and longitudinal wave velocities of doped fused silica and v_{t_silica} and v_{l_silica} are the transverse and longitudinal wave velocities of pure fused silica. Fortunately, the commonly used dopants for modifying the optical refractive indices of silica in optical fiber also affect the acoustic refractive indices [130], as shown in Table 5. 1.

This makes it possible that a double-cladding fiber structure shown in Figure 5.1(a), which can confine both light and acoustic waves within the fiber. For instance, in the double-cladding structure, we can use B_2O_3 as the dopant in layer 2, and Al_2O_3 as the dopant in layer 3. The resulting acoustic index and optical index profiles are shown in Figure 5.1(b) and (c) respectively. It is clear that layers 1 and 2 can confine light while layers 2 and 3 can confine acoustic waves. There are other possible dopant selections that can achieve simultaneous optical and acoustic confinement. And we still need to further investigate the acoustic waveguide theories to validate the proposed double-cladding fiber design for both optical and acoustic confinement.

Table 5.1. Optical (Δnop%) and acoustic indices (Δna,t% and Δna,l%) vs. dopant concentration (W%)

Dopant	Δn_{op}%/W%	$\Delta n_{a,t}$%/W%	$\Delta n_{a,l}$%/W%
GeO_2	+0.056	+0.54	+0.52
P_2O_5	+0.020	+0.45	+0.34
F	-0.31	+3.4	+3.70
TiO_2	+0.23	+0.5	+0.65
Al_2O_3	+0.063	-0.23	-0.46
B_2O_3	-0.033	+1.30	+1.35

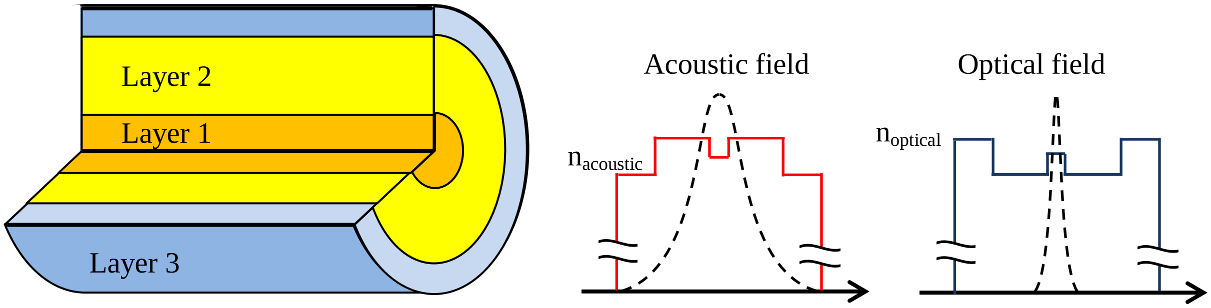

(a) (b) (c)

Figure 5.1. (a) Schematic of the proposed double-cladding fiber structure and its corresponding (b)acoustic index profile and (c) optical refractive profile.

References

1. Krohn, D.A., *Fiber Optical Sensors, Fundamentals and Applications*. 3rd Edition ed2000: Research Triangle Park, NC, Instrument Society of America.

2. Lopez-Higuera, J.M., *Handbook of optical fibre sensing technology*2002: John Wiley & Sons Inc.

3. Dakin, J. and B. Culshaw, *Optical Fiber Sensors: systems and applications*. Vol. 2. 1989: Artech House on Demand.

4. Dakin, J., et al., *Distributed optical fibre Raman temperature sensor using a semiconductor light source and detector.* Electronics letters, 1985. **21**(13): p. 569-570.

5. Horiguchi, T., T. Kurashima, and M. Tateda, *A technique to measure distributed strain in optical fibers.* Photonics Technology Letters, IEEE, 1990. **2**(5): p. 352-354.

6. Kurashima, T., T. Horiguchi, and M. Tateda, *Distributed-temperature sensing using stimulated Brillouin scattering in optical silica fibers.* Optics letters, 1990. **15**(18): p. 1038-1040.

7. Bao, X., D.J. Webb, and D.A. Jackson. *Recent progress in experiments on a Brillouin loss based distributed sensor*. 1994. Spie-Int Soc Optical Engineering.

8. Rogers, A., *Distributed optical-fibre sensors.* Journal of Physics D: Applied Physics, 1986. **19**: p. 2237.

9. Rogers, A., *Distributed optical-fibre sensing.* Measurement Science and Technology, 1999. **10**: p. R75.

10. Barnoski, M. and S. Jensen, *Fiber waveguides: a novel technique for investigating attenuation characteristics.* Applied optics, 1976. **15**(9): p. 2112-2115.

11. Jackson, D., *Recent progress in monomode fibre-optic sensors.* Measurement Science and Technology, 1994. **5**: p. 621.

12. Mallalieu, K.I., R. Youngquist, and D.E.N. Davies, *FMCW of optical source envelope modulation for passive multiplexing of frequency-based fibre-optic sensors.* Electronics letters, 1986. **22**(15): p. 809-810.

13. Cusano, A., et al., *High-sensitivity optical chemosensor based on coated long-period gratings for sub-ppm chemical detection in water.* Applied Physics Letters, 2005. **87**(23): p. 234105-234105-3.

14. Falate, R., et al., *Alternative technique for biodiesel quality control using an optical fiber long-period grating sensor.* Química Nova, 2007. **30**(7): p. 1677.

15. Rao, Y. and T. Zhu. *A highly sensitive fiber-optic refractive index sensor based on an edge-written long-period fiber grating*. in *Nonlinear Photonics*. 2007. Optical Society of America.

16. Gu, Z., Y. Xu, and K. Gao, *Optical fiber long-period grating with solgel coating for gas sensor.* Optics letters, 2006. **31**(16): p. 2405-2407.

17. Wang, L., et al., *A relative humidity sensor using a hydrogel-coated long period grating.* Measurement Science and Technology, 2007. **18**(10): p. 3131.

18. Kim, D., et al., *Fibre-optic interferometric immuno-sensor using long period grating.* Electronics letters, 2006. **42**(6): p. 324-325.

19. Swart, P.L., *Long-period grating Michelson refractometric sensor.* Measurement Science and Technology, 2004. **15**(8): p. 1576.

20. Delisa, M.P., et al., *Evanescent wave long-period fiber bragg grating as an immobilized antibody biosensor.* Analytical chemistry, 2000. **72**(13): p. 2895-2900.

21. Rogers, A., *Polarization-optical time domain reflectometry: A technique for the measurement of field distributions.* Applied optics, 1981. **20**(6): p. 1060-1074.

22. Han, M., Y. Wang, and A. Wang, *Grating-assisted polarization optical time-domain reflectometry for distributed fiber-optic sensing.* Optics letters, 2007. **32**(14): p. 2028-2030.

23. Healey, P., *Fading in heterodyne OTDR.* Electronics letters, 1984. **20**(1): p. 30-32.

24. Zhang, Z. and X. Bao, *Distributed optical fiber vibration sensor based on spectrum analysis of Polarization-OTDR system.* Optics Express, 2008. **16**(14): p. 10240-10247.

25. Eickhoff, W. and R. Ulrich, *Optical frequency domain reflectometry in single-mode fiber.* Applied Physics Letters, 1981. **39**(9): p. 693-695.

26. Koshikiya, Y., X. Fan, and F. Ito. *Highly Sensitive Coherent Optical Frequency-domain Reflectometry Employing SSB-modulator with cm-level Spatial Resolution over 5 km*. in *Optical Communication (ECOC), 2007 33rd European Conference and Ehxibition of*. 2007. VDE.

27. Passy, R., N. Gisin, and J. Von der Weid, *High-sensitivity-coherent optical frequency-domain reflectometry for characterization of fiber-optic network components.* Photonics Technology Letters, IEEE, 1995. **7**(6): p. 667-669.

28. Oberson, P., et al., *Optical frequency domain reflectometry with a narrow linewidth fiber laser.* Photonics Technology Letters, IEEE, 2000. **12**(7): p. 867-869.

29. Hartog, A., A. Leach, and M. Gold, *Distributed temperature sensing in solid-core fibres.* Electronics letters, 1985. **21**(23): p. 1061-1062.

30. Brown, G. and A. Hartog, *Optical fiber sensors in upstream oil & gas.* Journal of petroleum technology, 2002. **54**(11): p. 63-65.

31. Belal, M., et al., *A temperature-compensated high spatial resolution distributed strain sensor.* Measurement Science and Technology, 2009. **21**(1): p. 015204.

32. Horiguchi, T., et al., *Development of a distributed sensing technique using Brillouin scattering.* Lightwave Technology, Journal of, 1995. **13**(7): p. 1296-1302.

33. Fernandez, A.F., et al., *Radiation-tolerant Raman distributed temperature monitoring system for large nuclear infrastructures.* Nuclear Science, IEEE Transactions on, 2005. **52**(6): p. 2689-2694.

34. Bibby, G.W., *Temperature measurement*, 1989, EP Patent 0,190,001.

35. Suh, K. and C. Lee, *Auto-correction method for differential attenuation in a fiber-optic distributed-temperature sensor.* Optics letters, 2008. **33**(16): p. 1845-1847.

36. Hartog, A.H., M.P. Gold, and A.P. Leach, *Optical time-domain reflectometry*, 1989, Google Patents.

37. Bolognini, G., et al., *Analysis of distributed temperature sensing based on Raman scattering using OTDR coding and discrete Raman amplification.* Measurement Science and Technology, 2007. **18**(10): p. 3211.

38. Rogers, A., *Distributed optical-fibre sensing.* Measurement Science and Technology, 1999. **10**(8): p. R75-R99.

39. Höbel, M., et al., *High-resolution distributed temperature sensing with the multiphoton-timing technique.* Applied optics, 1995. **34**(16): p. 2955-2967.

40. Tanner, M.G., et al., *High-resolution single-mode fiber-optic distributed Raman sensor for absolute temperature measurement using superconducting nanowire single-photon detectors.* Applied Physics Letters, 2011. **99**(20): p. 201110-201110-3.

41. Dolfi, D.W., M. Nazarathy, and S.A. Newton, *5-mm-resolution optical-frequency-domain reflectometry using a coded phase-reversal modulator.* Optics letters, 1988. **13**(8): p. 678-680.

42. Nakayama, J. and J. Nielsen, *Optical fiber fault locator by the step frequency method.* Applied optics, 1987. **26**(3): p. 440-443.

43. Garcus, D., et al., *Brillouin optical-fiber frequency-domain analysis for distributed temperature and strain measurements.* Lightwave Technology, Journal of, 1997. **15**(4): p. 654-662.

44. Horiguchi, T., T. Kurashima, and M. Tateda, *Tensile strain dependence of Brillouin frequency shift in silica optical fibers.* Photonics Technology Letters, IEEE, 1989. **1**(5): p. 107-108.

45. Smith, J., et al., *Simultaneous distributed strain and temperature measurement.* Applied optics, 1999. **38**(25): p. 5372-5377.

46. Farahani, M.A. and T. Gogolla, *Spontaneous Raman scattering in optical fibers with modulated probe light for distributed temperature Raman remote sensing.* Journal of Lightwave Technology, 1999. **17**(8): p. 1379.

47. Bao, X. and L. Chen, *Recent progress in Brillouin scattering based fiber sensors.* Sensors, 2011. **11**(4): p. 4152-4187.

48. Bao, X., et al., *Characterization of the Brillouin-loss spectrum of single-mode fibers by use of very short (< 10-ns) pulses.* Optics letters, 1999. **24**(8): p. 510-512.

49. Garus, D., et al., *Distributed sensing technique based on Brillouin optical-fiber frequency-domain analysis.* Optics letters, 1996. **21**(17): p. 1402-1404.

50. Hotate, K. and T. Hasegawa, *Measurement of Brillouin Gain Spectrum Distribution along an Optical Fiber Using a Correlation-Based Technique--Proposal, Experiment and Simulation.* IEICE transactions on electronics, 2000. **83**(3): p. 405-412.

51. DeMerchant, M.D., et al. *Automated system for distributed sensing*. in *5th Annual International Symposium on Smart Structures and Materials*. 1998. International Society for Optics and Photonics.

52. Brown, A.W., B.G. Colpitts, and K. Brown, *Distributed sensor based on dark-pulse Brillouin scattering*. Photonics Technology Letters, IEEE, 2005. **17**(7): p. 1501-1503.

53. Bernini, R., A. Minardo, and L. Zeni, *Distributed Sensing at Centimeter-Scale Spatial Resolution by BOFDA: Measurements and Signal Processing.* Photonics Journal, IEEE, 2012. **4**(1): p. 48-56.

54. Hotate, K. and M. Tanaka, *Distributed fiber Brillouin strain sensing with 1-cm spatial resolution by correlation-based continuous-wave technique.* Photonics Technology Letters, IEEE, 2002. **14**(2): p. 179-181.

55. Bao, X., D.J. Webb, and D.A. Jackson, *22-km distributed temperature sensor using Brillouin gain in an optical fiber.* Optics letters, 1993. **18**(7): p. 552-554.

56. Bao, X., D.J. Webb, and D.A. Jackson, *32-km distributed temperature sensor based on Brillouin loss in an optical fiber.* Optics letters, 1993. **18**(18): p. 1561-1563.

57. Wang, S. *Optical fiber gas sensing system based on FBG filtering*. 2008.

58. Wang, K., D. Klimov, and Z. Kolber. *Long period grating-based fiber-optic PH sensor for ocean monitoring*. 2007.

59. Buerck, J. and E. Sensfelder. *Optical fiber sensors for the distributed measurement of hydrocarbons*. 1999.

60. Zeng, L., et al., *A Novel Fiber-Optic Biosensor for On-Line Monitoring of Cell Cultivation.* Sens. Mater, 2005. **17**(4): p. 211-217.

61. Kim, G.Y., et al., *Detection of Listeria monocytogenes using an automated fiber-optic biosensor: RAPTOR.* Key Engineering Materials, 2006. **321**: p. 1168-1171.

62. Thévenot, D.R., et al., *Electrochemical biosensors: recommended definitions and classification.* Biosensors and Bioelectronics, 2001. **16**(1): p. 121-131.

63. Höök, F., et al., *A comparative study of protein adsorption on titanium oxide surfaces using in situ ellipsometry, optical waveguide lightmode spectroscopy, and quartz crystal microbalance/dissipation.* Colloids and Surfaces B: Biointerfaces, 2002. **24**(2): p. 155-170.

64. Anderson, G.P. and N.L. Nerurkar, *Improved fluoroimmunoassays using the dye Alexa Fluor 647 with the RAPTOR, a fiber optic biosensor.* Journal of immunological methods, 2002. **271**(1): p. 17-24.

65. Skládal, P., A. Deng, and V. Kolár, *Resonant mirror-based optical immunosensor: application for the measurement of atrazine in soil.* Analytica chimica acta, 1999. **399**(1-2): p. 29-36.

66. Oh, B.K., et al., *Surface plasmon resonance immunosensor for the detection of< i> Salmonella typhimurium</i>.* Biosensors and Bioelectronics, 2004. **19**(11): p. 1497-1504.

67. Zhang, Y., et al., *Miniature fiber-optic multicavity Fabry-Perot interferometric biosensor.* Optics letters, 2005. **30**(9): p. 1021-1023.

68. Bakaltcheva, I.B., et al., *Multi-analyte explosive detection using a fiber optic biosensor.* Analytica chimica acta, 1999. **399**(1-2): p. 13-20.

69. Toppozada, A.R., et al., *Evaluation of a fiber optic immunosensor for quantitating cocaine in coca leaf extracts.* Biosensors and Bioelectronics, 1997. **12**(2): p. 113-124.

70. Nath, N., et al., *A rapid reusable fiber optic biosensor for detecting cocaine metabolites in urine.* Journal of analytical toxicology, 1999. **23**(6): p. 460-467.

71. Mouvet, C., et al., *Determination of simazine in water samples by waveguide surface plasmon resonance.* Analytica chimica acta, 1997. **338**(1-2): p. 109-117.

72. Brecht, A., et al., *Optical immunoprobe development for multiresidue monitoring in water.* Analytica chimica acta, 1998. **362**(1): p. 69-79.

73. Kwon, H.J., H.I. Balcer, and K.A. Kang, *Sensing performance of protein C immuno-biosensor for biological samples and sensor minimization.* Comparative Biochemistry and Physiology-Part A: Molecular & Integrative Physiology, 2002. **132**(1): p. 231-238.

74. King, K.D., et al., *Detecting staphylococcal enterotoxin B using an automated fiber optic biosensor.* Biosensors and Bioelectronics, 1999. **14**(2): p. 163-170.

75. Zhou, C., et al., *A compact fiber-optic immunosensor for Salmonella based on evanescent wave excitation.* Sensors and Actuators B: Chemical, 1997. **42**(3): p. 169-175.

76. Lu, B., C. Lu, and Y. Wei, *A planar quartz waveguide immunosensor based on TIRF principle.* Analytical letters, 1992. **25**(1): p. 1-10.

77. Wijesuriya, D., et al., *Regeneration of immobilized antibodies on fiber optic probes.* Biosensors and Bioelectronics, 1994. **9**(8): p. 585-592.

78. Han, M., Y. Wang, and A. Wang, *Fiber-optic physical and biochemical sensing based on transient and traveling long-period gratings.* Optics letters, 2009. **34**(1): p. 100-102.

79. Hill, K., et al., *Efficient mode conversion in telecommunication fibre using externally written gratings.* Electronics letters, 1990. **26**(16): p. 1270-1272.

80. Hill, K., et al., *Photosensitivity in optical fiber waveguides: Application to reflection filter fabrication.* Applied Physics Letters, 1978. **32**(10): p. 647-649.

81. Snyder, A.W. and W.R. Young, *Modes of optical waveguides.* JOSA, 1978. **68**(3): p. 297-309.

82. Snyder, A.W. and J. Love, *Optical waveguide theory*. Vol. 190. 1983: Springer.

83. Gloge, D., *Weakly guiding fibers.* Applied optics, 1971. **10**(10): p. 2252-2258.

84. Erdogan, T., *Cladding-mode resonances in short-and long-period fiber grating filters.* JOSA A, 1997. **14**(8): p. 1760-1773.

85. Anemogiannis, E., E. Glytsis, and T. Gaylord, *Transmission characteristics of long-period fiber gratings having arbitrary azimuthal/radial refractive index variations.* Journal of Lightwave Technology, 2003. **21**(1): p. 218.

86. Rao, Y.J., et al., *Novel fiber-optic sensors based on long-period fiber gratings written by high-frequency CO< sub> 2</sub> laser pulses.* Lightwave Technology, Journal of, 2003. **21**(5): p. 1320-1327.

87. Kondo, Y., et al., *Fabrication of long-period fiber gratings by focused irradiation of infrared femtosecond laser pulses.* Optics letters, 1999. **24**(10): p. 646-648.

88. Nam, S., et al., *Bend-insensitive ultra short long-period gratings by the electric arc method and their applications to harsh environment sensing and communication.* Optics Express, 2005. **13**(3): p. 731-737.

89. Kosinski, S.G. and A.M. Vengsarkar. *Splicer-based long-period fiber gratings*. in *Optical Fiber Communication Conference and Exhibit, 1998. OFC'98., Technical Digest*. 1998. IEEE.

90. Fujimaki, M., et al., *Fabrication of long-period optical fiber gratings by use of ion implantation.* Optics letters, 2000. **25**(2): p. 88-89.

91. Jeong, Y., et al., *Electrically controllable long-period liquid crystal fiber gratings.* Photonics Technology Letters, IEEE, 2000. **12**(5): p. 519-521.

92. Savin, S., et al., *Tunable mechanically induced long-period fiber gratings.* Optics letters, 2000. **25**(10): p. 710-712.

93. Yokouchi, T., et al., *Thermal tuning of mechanically induced long-period fiber grating.* Applied optics, 2005. **44**(24): p. 5024-5028.

94. Rego, G., et al., *High-temperature stability of long-period fiber gratings produced using an electric arc.* Lightwave Technology, Journal of, 2001. **19**(10): p. 1574-1579.

95. Yariv, A. and P. Yeh, *Optical waves in crystals*. Vol. 5. 1984: Wiley New York.

96. Diez, A., et al., *High strain-induced wavelength tunability in tapered fibre acousto-optic filters.* Electronics letters, 2000. **36**(14): p. 1187-1188.

97. Birks, T.A., P.S.J. Russell, and D. Culverhouse, *The acousto-optic effect in single-mode fiber tapers and couplers.* Lightwave Technology, Journal of, 1996. **14**(11): p. 2519-2529.

98. Li, Q., et al., *Highly efficient acoustooptic tunable filter based on cladding etched single-mode fiber.* Photonics Technology Letters, IEEE, 2002. **14**(3): p. 337-339.

99. Engan, H.E., et al., *Propagation and optical interaction of guided acoustic waves in two-mode optical fibers.* Lightwave Technology, Journal of, 1988. **6**(3): p. 428-436.

100. Li, H., et al., *Design of tunable composite spectrums using all-fiber acoustooptical filters subject to strain control.* Journal of Lightwave Technology, 2006. **24**(4): p. 1855.

101. Ghosh, G., M. Endo, and T. Iwasaki, *Temperature-dependent Sellmeier coefficients and chromatic dispersions for some optical fiber glasses.* Lightwave Technology, Journal of, 1994. **12**(8): p. 1338-1342.

102. Brückner, V., *To the use of Sellmeier formula.*

103. Safaai-Jazi, D.A., *Lecture notes of 'Photonic Devices and Systems, ECE6154.*

104. Kim, H.S., et al., *All-fiber acousto-optic tunable notch filter with electronically controllable spectral profile.* Optics letters, 1997. **22**(19): p. 1476-1478.

105. Pennington, C., et al. *Fiber-optic-based biosensors utilizing long period grating (LPG) technology*. in *BiOS 2001 The International Symposium on Biomedical Optics*. 2001. International Society for Optics and Photonics.

106. Zhang, W., et al., *All-fiber acousto-optic tunable notch filter with a fiber winding driven by a cuneal acoustic transducer.* Optics letters, 2011. **36**(2): p. 271-273.

107. Law, P.C., et al., *Acoustic coefficients of P< sub> 2</sub> O< sub> 5</sub>-doped silica fiber: acoustic velocity, acoustic attenuation, and thermo-acoustic coefficient.* Optical Materials Express, 2011. **1**(4): p. 686-699.

108. Brown, D.C. and H.J. Hoffman, *Thermal, stress, and thermo-optic effects in high average power double-clad silica fiber lasers.* Quantum Electronics, IEEE Journal of, 2001. **37**(2): p. 207-217.

109. Zhang, Y., *Miniature fiber-optic multicavity Fabry-Perot interferometric biosensor*.

110. Caruso, F., et al., *2. Assembly of alternating polyelectrolyte and protein multilayer films for immunosensing.* Langmuir, 1997. **13**(13): p. 3427-3433.

111. Wang, X., et al., *Label-free DNA sequence detection using oligonucleotide functionalized optical fiber.* Applied Physics Letters, 2006. **89**: p. 163901.

112. Shibru, H., et al., *Optimization of layer-by-layer electrostatic self-assembly processing parameters for optical biosensing.* Optical Engineering, 2006. **45**: p. 024401.

113. Wang, Z., et al., *Analysis of optical response of long period fiber gratings to nm-thick thin-film coatings.* Opt. Express, 2005. **13**(8): p. 2808-2813.

114. Caucheteur, C., et al., *Hybrid fiber gratings coated with a catalytic sensitive layer for hydrogen sensing in air.* Optics Express, 2008. **16**(21): p. 16854-16859.

115. Sekimoto, S., et al., *A fiber-optic evanescent-wave hydrogen gas sensor using palladium-supported tungsten oxide.* Sensors and Actuators B: Chemical, 2000. **66**(1-3): p. 142-145.

116. Sumida, S., et al., *Distributed hydrogen determination with fiber-optic sensor.* Sensors and Actuators B: Chemical, 2005. **108**(1-2): p. 508-514.

117. Shin, W., et al., *Thermoelectric thick-film hydrogen gas sensor operating at room temperature.* Japanese Journal of Applied Physics, 2001. **40**: p. 1232.

118. Safaai-Jazi, A., C.K. Jen, and G. Farnell, *Analysis of weakly guiding fiber acoustic waveguide.* IEEE transactions on ultrasonics, ferroelectrics, and frequency control, 1986. **33**(1): p. 59-68.

119. Lee, K.J., et al., *Polarization-coupling all-fiber acousto-optic tunable filter insensitive to fiber bend and physical contact.* Optics Express, 2009. **17**(8): p. 6096-6100.

120. Wang, D.Y., et al., *Fully Distributed Fiber-Optic Biological Sensing.* Photonics Technology Letters, IEEE, 2010. **22**(21): p. 1553-1555.

121. Berwick, M., et al., *Demonstration of birefringent optical fibre frequency shifter employing torsional acoustic waves.* Electronics letters, 1991. **27**(9): p. 713-715.

122. Lee, K.J., H.C. Park, and B.Y. Kim, *Highly efficient all-fiber tunable polarization filter using torsional acoustic wave.* Opt. Express, 2007. **15**(19): p. 12362–12367.

123. Stolen, R.H., et al., *In-line fiber-polarization-rocking rotator and filter.* Optics letters, 1984. **9**(7): p. 300-302.

124. Statkiewicz-Barabach, G., et al., *Sensing characteristics of rocking filter fabricated in microstructured birefringent fiber using fusion arc splicer.* Optics Express, 2008. **16**(22): p. 17249-17257.

125. Kakarantzas, G., et al., *Structural rocking filters in highly birefringent photonic crystal fiber.* Optics letters, 2003. **28**(3): p. 158-160.

126. Kim, D.H. and J.U. Kang, *Sagnac loop interferometer based on polarization maintaining photonic crystal fiber with reduced temperature sensitivity.* Opt. Express, 2004. **12**(19): p. 4490–4495.

127. Cheeke, J.D.N., *Fundamentals and applications of ultrasonic waves*2002: CRC.

128. Available from: http://www.csgnetwork.com/atmossndabsorbcalc.html.

129. Jen, C.K., A. Safaai-Jazi, and G. Farnell, *Leaky modes in weakly guiding fiber acoustic waveguides.* IEEE transactions on ultrasonics, ferroelectrics, and frequency control, 1986. **33**(6): p. 634-643.

130. Jen, C.K., et al., *Acoustic characterization of silica glasses.* Journal of the American Ceramic Society, 1993. **76**(3): p. 712-716.